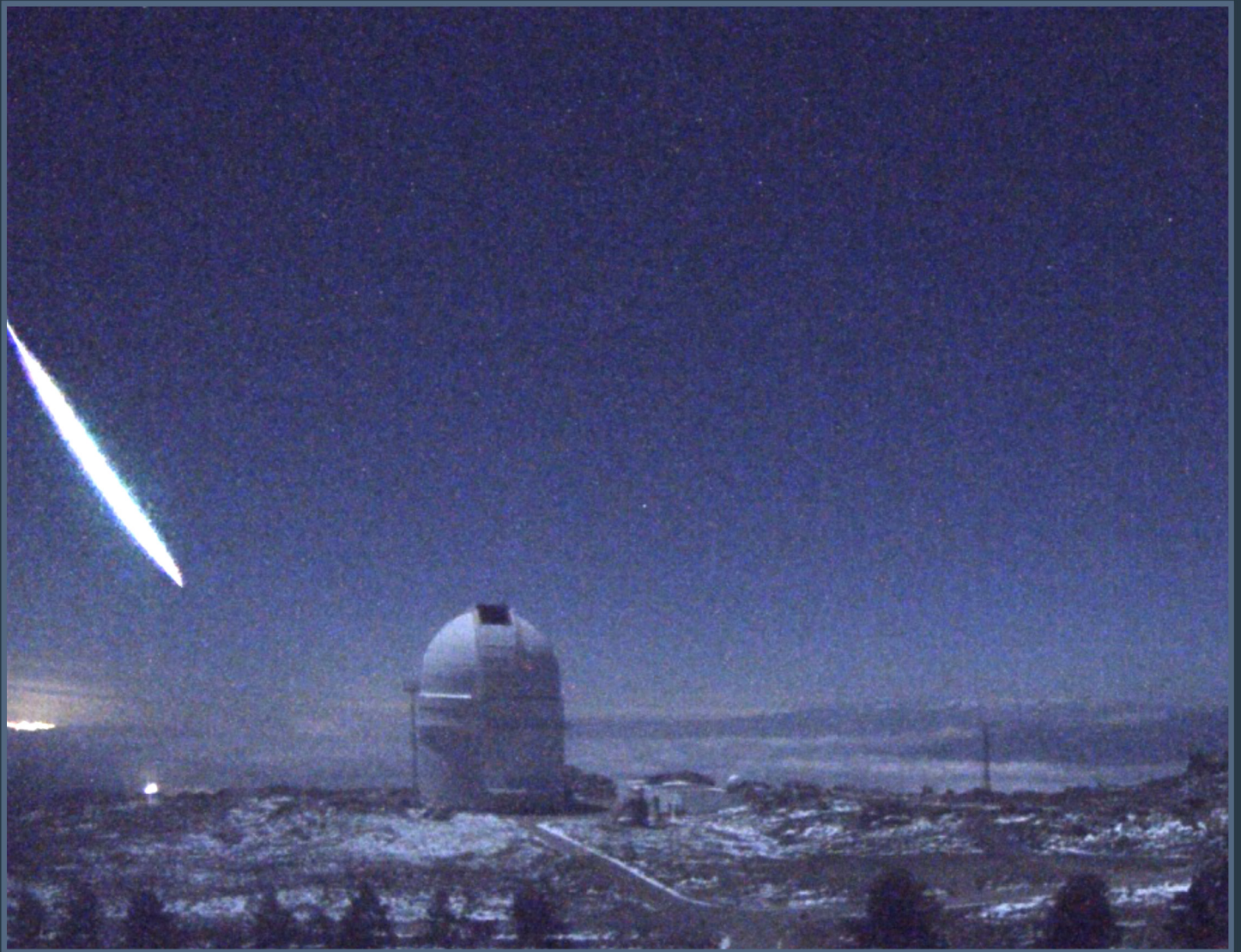


MeteorNews

ISSN 2570-4745

VOL 8 / ISSUE 3 / MAY 2023



Stacked image of the SWEMN20230201_200423 "Oulad Aneur" fireball as recorded from Calar Alto, Spain (Courtesy: Southwestern Europe Meteor Network)

- February Hydrids
- Activity of 68 Virginids
- GMN results
- CAMS reports
- Radio meteor work
- Fireballs

Contents

Properties of 14 major meteor showers: magnitude ratio derived from video observations <i>M. Koseki</i>	151
New meteor shower in Draco <i>D. Šegon, D. Vida, and P. Roggemans</i>	171
New meteor shower in Bootes <i>D. Šegon, D. Vida, and P. Roggemans</i>	177
February Hydrids (FHY#1032) in 2023 <i>P. Jenniskens</i>	181
Increased activity 68 Virginid (OAV#00651) in 2023 <i>Y. Harachka, I. Sergei, and R. Zavadich</i>	183
Using GUI RMS on Linux to support multiple cameras <i>E. Harman, P. Eschman, B. Massey, and W. Olivera</i>	185
February 2023 report CAMS-BeNeLux <i>C. Johannink</i>	197
March 2023 report CAMS-BeNeLux <i>C. Johannink</i>	199
First steps of the CARMELO network (Cheap Amateur Radio Meteors Echoes Logger) <i>L. Barbieri, G. Brando, P. Fontana, and S. Sarto</i>	201
Radio meteors February 2023 <i>F. Verbelen</i>	207
Radio meteors March 2023 <i>F. Verbelen</i>	214
The Southwestern Europe Meteor Network: remarkable meteors recorded between February and March 2023 <i>J.M. Madiedo, J.L. Ortiz, J. Izquierdo, P. Santos-Sanz, J. Aceituno, E. de Guindos, P. Yanguas, J. Palacián, A. San Segundo, D. Ávila, B. Tosar, A. Gómez-Hernández, J. Gómez-Martínez, A. García, and A.I. Aimee</i>	222

Properties of 14 major meteor showers: magnitude ratio derived from video observations

Masahiro Koseki

The Nippon Meteor Society, 4-3-5 Annaka Annaka-shi, Gunma-ken, 379-0116 Japan

geh04301@nifty.ne.jp

We challenge to investigate the magnitude ratio (r) of 14 major meteor showers using SonotaCo net video data: Quadrantids (QUA#010), Lyrids (LYR#006), eta Aquariids (ETA#031), Southern delta Aquariids (SDA#005), Capricornids (CAP#001), Perseids (PER#007), Orionids (ORI#008), STA_SE (Steady Expression of Southern Arietids, STA#002), STA_SF (Sharply Fluctuating component of ‘Southern Taurids’, STA#002), Northern Taurids (NTA#017), Leonids (LEO#013), sigma Hydriids (HYD#016), Geminids (GEM#004), and Comae Berenicids (COM#020). We compensate for the observation bias by using the sporadic meteor distribution and the results are in good agreement with past results. The magnitude ratio (r) and the beginning height of a meteor shower strongly relate, and these properties obtained by video observations give a useful clue to infer the origin of the meteoroids. We study the two most important major meteor showers in detail (Perseids and Geminids) and find a very interesting peculiarity in the Geminids; brighter meteors with absolute magnitude $M_A < -2$ decrease in number compared to sporadic meteors and other meteor showers of course, and the beginning height of Geminids is almost the same as for sporadic meteors.

1 Introduction

Video observations are now conducted on a large scale worldwide. Their results are usually used to detect unknown meteor showers, but other useful data are often disregarded: absolute magnitude and beginning height for example. The author tried to estimate the magnitude ratio from video data, however, photometry in video observations is unique for every observation system (Koseki, 2023). As Ceplecha showed the beginning height of a meteor path suggests the property of its meteoroid (Ceplecha, 1968), the author used this as an index of the meteor shower property in the case of the remnants from comet 73P/Schwassmann–Wachmann 3 (Koseki, 2022). A vast amount of video data has been accumulated but this has not been used to analyze major shower properties. We challenge here to show the importance of forgotten video data by representing the properties of major meteor showers using SonotaCo net video data (SonotaCo, 2009¹; SonotaCo et al., 2021).

2 Activity profile and mean magnitude

For each of the 14 major meteor showers, we will discuss in detail and show the activity profile and the mean absolute magnitude (M_A) change (see Section 5). You may be wondering why the Southern Taurids (STA#002) are split. The author stressed that the “Southern Taurids” have two quite different activity peaks: one around October 13 and another around November 5 (Koseki, 2020).

These graphs display the sliding mean of the number of shower meteors (solid blue line) and of the absolute magnitude (dotted orange line) with 1 solar longitude bin; the number is divided by the years of the observations, which is 15 for representing the yearly average activity

profile. These activity profiles are derived using the raw number and have not been compensated for the background sporadic meteor activity; observing conditions may have affected the profiles. This research aims to investigate the outline of the properties of meteor showers. If one intended to show more accurate activity profiles, this could be obtained by using the DR parameter (density ratio of shower meteors to sporadic meteors): see Koseki (2019).

We use the classification applied in SonotaCo net data except for the two STAs and NTA.

3 Magnitude ratio

3.1 Slope in the logarithm distribution

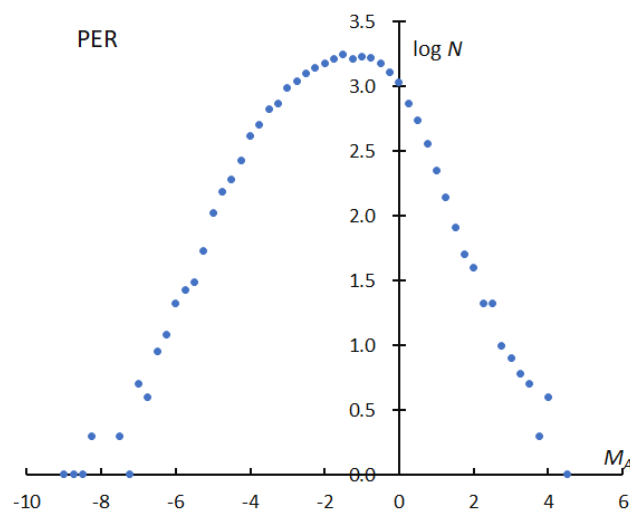


Figure 1 – The logarithm distribution of the number of meteors in function of the absolute magnitude for the Perseids. The classification of meteor showers is based on SonotaCo net.

¹ See also “SonotaCo Network Simultaneously Observed Meteor Data Sets”, <http://sonotaco.jp/doc/SNM/>.

The magnitude ratio is determined by the slope of the logarithm distribution of meteor numbers along the magnitude; *Figure 1* shows the distribution for the Perseids for example. But it is not so easy to determine the magnitude ratio, because the distribution cannot be expressed by a linear regression line (see *Table 1*).

Table 1 – The magnitude ratio estimated by several different magnitude’s ranges for *Figure 1*. Slopes represent the results of the regression analysis in given magnitude ranges and the magnitude ratios are values corresponding to the slopes.

Magnitude range	slope	Magnitude ratio
-7~-2	0.548	3.54
-7~-3	0.625	4.22
-7~-4	0.681	4.80
-6~-2	0.494	3.12
-6~-3	0.591	3.90
-6~-4	0.681	4.80

Such a distribution as shown in *Figure 1* reflects not only the real meteoroid distribution but also the observational selection. Video observations have problems with their photometric techniques as well as with the perception of the meteor magnitude. If we could estimate the perception coefficients for SonotaCo net system, the magnitude distribution might be represented by a smoother line.

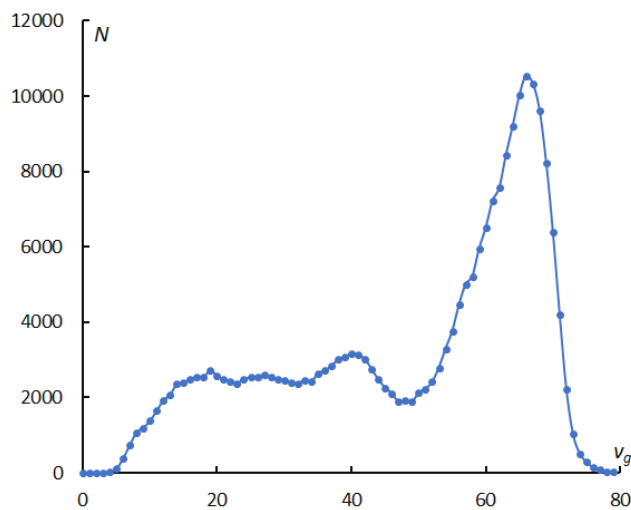


Figure 2 – The velocity distribution of sporadic meteors in video observations. It is important to note that different observation techniques give different results.

We know there are two meteor groups divided by a geocentric velocity v_g of 50 km/s (*Figures 2 and 3*). *Figure 2* represents the sporadic meteor number distribution against the geocentric velocity; it should be stressed that this graph is for SonotaCo net and the shapes of the graphs differ depending on observational techniques although the two groups are obvious in these graphs (Koseki, 2015).

Figure 3 displays the ratio of the number of meteors with v_g less than 50 km/s to the number with v_g faster than 50 km/s, standardized by each total number of meteors against the meteor magnitude. There are two striking characteristics; the slower meteors with $M_A = -3 \sim -4$, exceed the faster ones

by more than a factor of two and the change in M_A is very regular. We can suggest two reasons; both the perception coefficients and the magnitude ratio vary with the geocentric velocity.

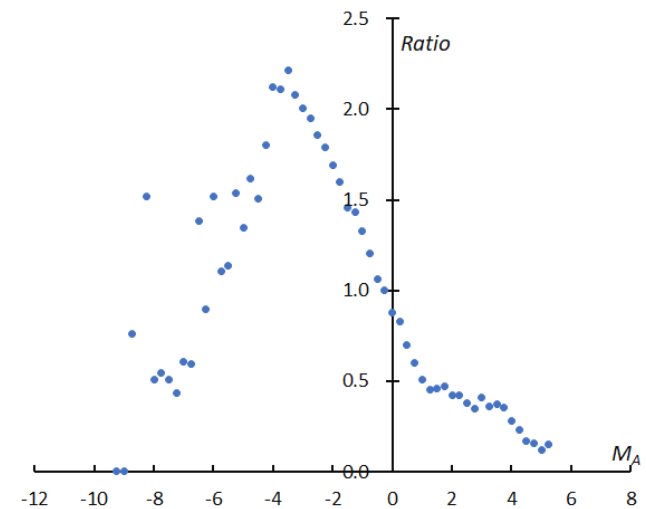


Figure 3 – The ratio of the number of meteors slower than 50 km/s to the number of faster meteors against the meteor magnitude. This graph is standardized by each total number of meteors and we can see that the faster meteors dominate in fainter meteors $M_A > 0$ and the brightest range $M_A < -5$.

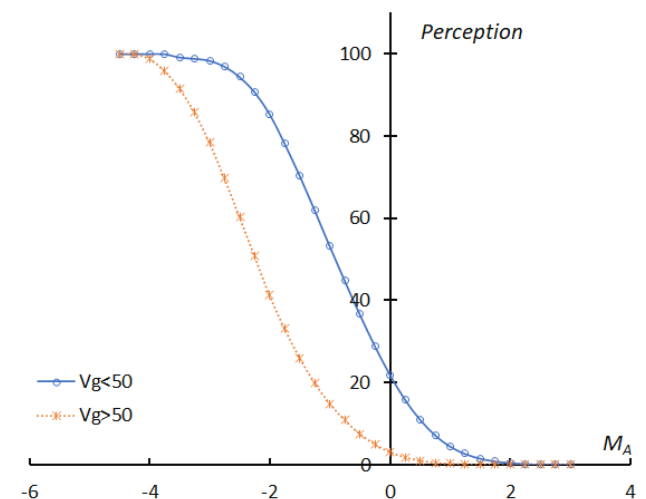


Figure 4 – Perception coefficients for meteors slower than 50 km/s and faster than 50 km/s with the assumption $r = 3.18$ for meteors slower than 50 km/s and $r = 4.24$ for faster meteors.

We estimate two perception coefficients, one for meteors slower than 50 km/s and one for faster meteors. *Figure 4* shows the smoothed lines of these coefficients. If we correct the number distribution of the Perseids using the perception coefficient for meteors faster than 50 km/s, a pretty good distribution can be plotted in *Figure 5* compared to *Figure 1*. We can get $r = 3.04$ from the slope between $M_A = -4$ and $M_A = 0$. The used coefficient is temporary because the values in *Figure 4* are estimated by the assumption of $r = 3.18$ for meteors slower than 50 km/s and $r = 4.24$ for faster meteors. The magnitude ratio and the perception coefficient might change with the geocentric velocity, and, therefore, $r = 3.04$ for the Perseids seems to be overestimated. SonotaCo net has piled up a great amount of data, but this data is still not enough to evaluate the

perception coefficient changes in function of the geocentric velocity.

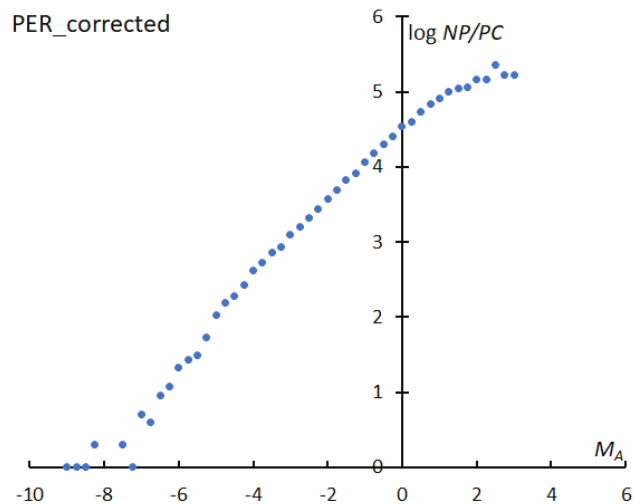


Figure 5 – The corrected logarithm distribution of meteor numbers against the magnitude for the Perseids using the perception coefficient curve for meteors faster than 50 km/s.

We try to search for another way to obtain the magnitude ratio; we study the ratio of shower meteors to sporadic meteors instead of the perception coefficient. If the perception coefficients of both shower meteors and sporadic ones are assumed to be equal, we could calculate the magnitude ratio using the ratio of shower meteors and sporadic ones; $r = 10^{(s_{sh} + s_{sp})}$, where s_{sh} is the slope of the shower meteors to the sporadic meteors and s_{sp} is the slope of the sporadic meteors. First of all, it is necessary to investigate how the magnitude ratio of sporadic meteors changes with the geocentric velocity.

3.2. Magnitude ratio dependence on a geocentric velocity

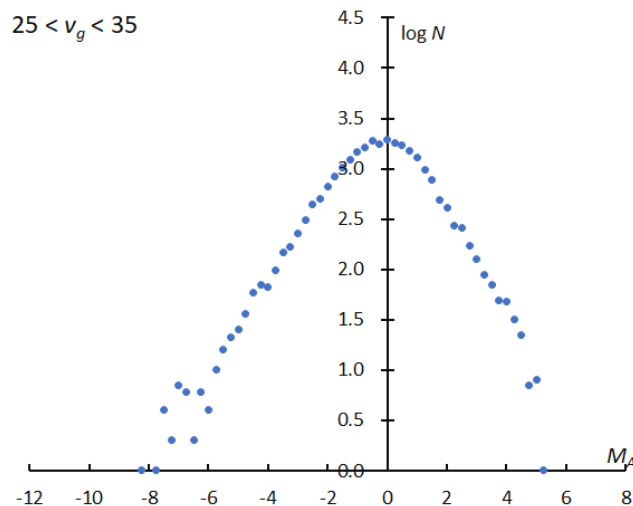


Figure 6a – The logarithm distribution of the number of sporadic meteor against absolute magnitude M_A , for 25 km/s < v_g < 35 km/s.

As suggested by Figure 3, the magnitude ratio of sporadic meteors varies with the geocentric velocity. We divided sporadic meteors into 14 groups with 10 km/s bins in geocentric velocity overlapping 5 km/s each, $v_g < 15$,

$10 < v_g < 20$, $15 < v_g < 25$, and so on. Figures 6a and 6b show the logarithm distribution for $25 < v_g < 35$ and $60 < v_g < 70$ as examples. The two graphs show that the slopes are different. The slope of the faster meteors is steeper (Figure 6b). But, the two graphs are not straight lines, and it is difficult to select the most suitable section (Table 2).

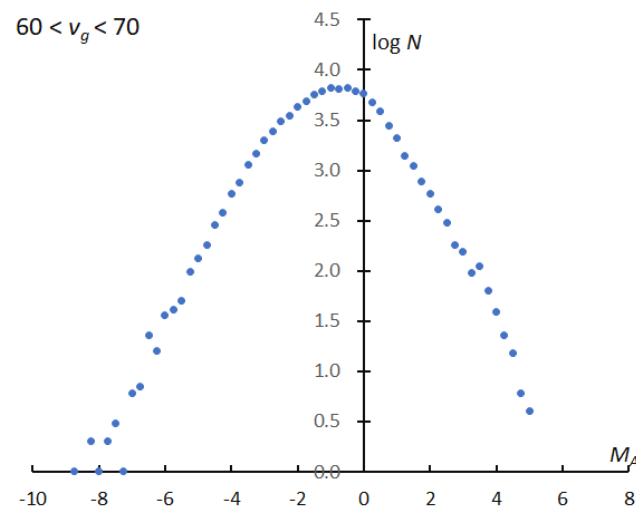


Figure 6b – The logarithm distribution of the number of sporadic meteor against absolute magnitude M_A , for 60 km/s < v_g < 70 km/s.

Table 2 – The slopes of the logarithm distribution and the derived magnitude ratios in the different magnitude ranges for Figures 6a and 6b.

		25 < v_g < 35				
Range		-6~-4	-5~-3	-4~-2	-6~-2	-6~-3
slope		0.586	0.455	0.489	0.5	0.521
r		3.85	2.85	3.09	3.16	3.32
		60 < v_g < 70				
Range		-6~-4	-5~-3	-4~-2	-6~-2	-6~-3
slope		0.634	0.593	0.437	0.556	0.612
r		4.31	3.92	2.73	3.6	4.1

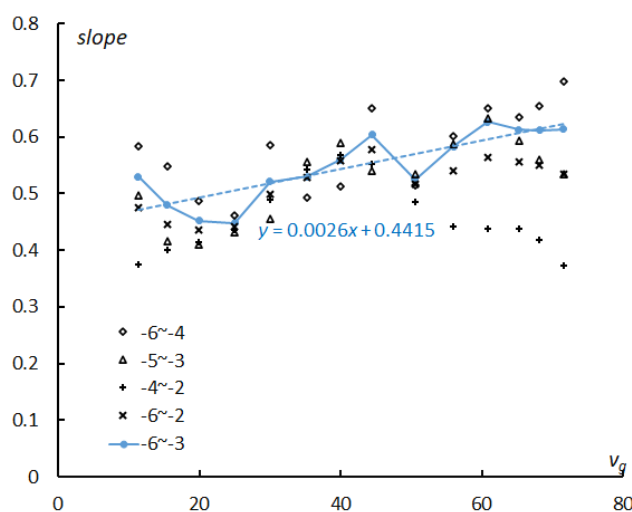


Figure 7 – Changes in the slopes shown in Table 2 along with the geocentric velocity. The values of the slopes for the most plausible range $-6 < M_A < -3$ are connected, and the result of the regression analysis is shown as inset.

We plot the slopes and the estimated magnitude ratios for all groups in *Figure 7*. The range $M_A = -4 \sim -2$ is clearly influenced by the perception coefficient which becomes lower for faster meteors, and the slope is dropping after $v_g > 50$ km/s. The range $M_A = -6 \sim -2$ seems to be influenced by the perception coefficient because meteors fainter than $M_A > -3$ may be overlooked. Therefore, we select the range $M_A = -6 \sim -3$, because the range is wider than the other two ranges and gives moderate magnitude ratios. We use the result of the linear regression analysis to estimate the magnitude distribution of sporadic meteors hereafter.

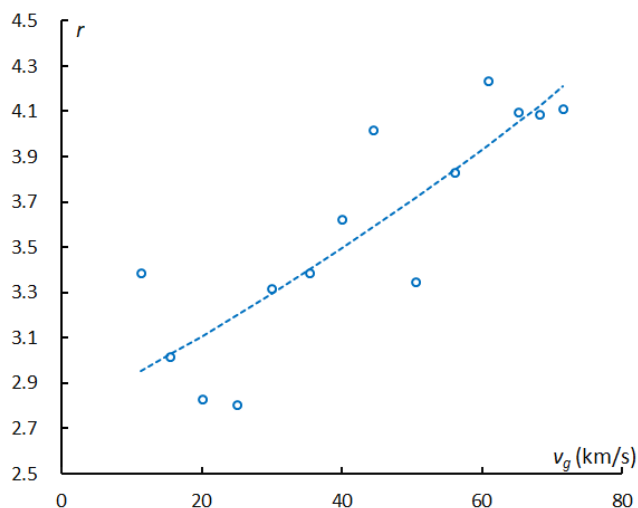


Figure 8 – Estimated magnitude ratio for sporadic meteors with geocentric velocity derived from the slopes of $-6 < M_A < -3$ in *Figure 7*. The dashed line is given by the result of the regression analysis in *Figure 7* and we use it hereafter for the estimation of the magnitude ratio of shower meteors.

Figure 8 shows the estimated magnitude ratio of sporadic meteors based on the slopes for the range $M_A = -6 \sim -3$, and the smoothed line represents the relationship of the slope of the magnitude distribution with the geocentric velocity as the result of the regression analysis.

3.3. Ratio of shower meteors to sporadic meteors

We know the dependence of the magnitude ratio of sporadic meteors on the geocentric velocity (*Figure 8*), and, therefore, we can estimate the magnitude ratio of the shower meteors by calculating the ratio of shower meteors to sporadic meteors against the absolute magnitude.

It is necessary to examine the magnitude distribution around the mean geocentric velocity of the shower meteors to calculate the ratio. *Figure 9* shows the magnitude distribution of sporadic meteors around $v_g = 58.7$ km/s, which is the mean geocentric velocity of the Perseids; we choose the velocity range as ± 5 km/s: $v_g = 53.7 \sim 63.7$ km/s. *Figure 10* gives the results for the comparison of *Figure 1* with *Figure 9*: the ratio of the number of Perseids to sporadic meteors in a logarithm distribution. It seems to be better to adopt a linear regression to the graph of *Figure 10* rather than to *Figure 5*. We exclude both the ranges brighter than $M_A < -4$ and fainter than $M_A > +2$, because the smaller numbers of data cause uncertainties. The magnitude ratio of the Perseids, then, can be calculated by estimating the

slope of the sporadic meteors for $v_g = 58.7$ km/s which is 0.5914 in *Figure 7* and the slope of the Perseids to sporadic meteors in *Figure 10* is -0.1956 : $r = 10^{(0.5914 - 0.1956)} = 2.49$.

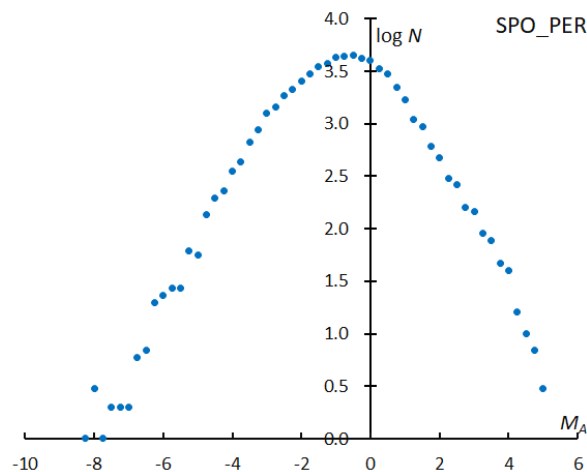


Figure 9 – The magnitude distribution of sporadic meteors $v_g = 58.7 \pm 5$ km/s, which is around the mean magnitude of the Perseids.

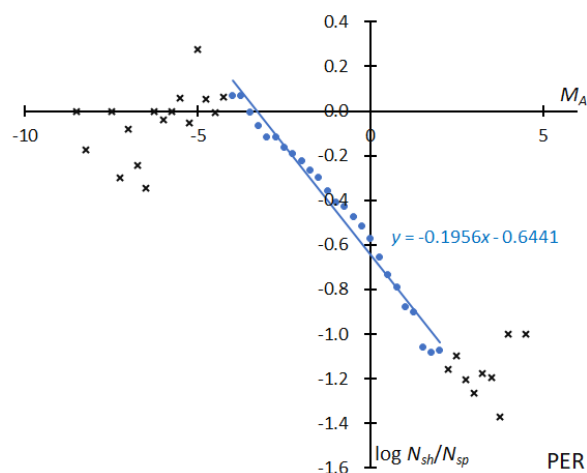


Figure 10 – The logarithm distribution of the ratio of the number of Perseids (*Figure 1*) to sporadic meteors (*Figure 9*).

We can confirm the workability of the ratio of shower meteors to sporadic meteors by applying this method to the major showers (see *Figures 12, 15, 18, 21, 24, 27, 31, 35, 39, 43, 46, 49, 52 and 55*). The full line is the result of the linear regression analysis between $M_A = -4 \sim +2$. Crosses on both sides are excluded from the analysis because of the scarcity of data. Because all abscissas in the above-mentioned figures are the same and the widths of the ordinates are the same, we can derive the difference in the magnitude distribution as seen in the slope of the figures. A steep slope means such a meteor shower is rich in bright meteors and a flatter one suggests it is rich in faint meteors. Both enhanced activities of the Orionids in 2007–09 and the STA_SF display were rich in bright meteors. We can see the explanation for the difference in the mean magnitude (see *Figures 11, 14, 17, 20, 23, 26, 29, 30, 34, 37, 38, 42, 45, 48, 51 and 54*) from another point of view. The slopes of the logarithm distribution of the ratio of shower meteors relative to sporadic meteors in function of the absolute magnitude shows that the magnitude ratios are different in each meteor showers.

Table 3 – Magnitude ratio of the major 14 meteor showers. v_g is the mean geocentric velocity of the shower. The slope is the slope of the magnitude distribution and r is the magnitude ratio. Each upper line is for sporadic meteors estimated by the relation shown in *Figure 7* and each lower line is for the meteor shower.

	QUA	LYR	ETA	SDA	CAP	PER	ORI1	ORI2	_SE	_SF1	_SF2	NTA	LEO	HYD	GEM	COM
v_g	40.2	46.6	65.6	39.7	22.3	58.7	65.9	65.9	28.5	27.9	27.9	27.3	69.9	59.4	33.8	62.9
slope	0.544	0.561	0.609	0.543	0.498	0.591	0.61	0.61	0.514	0.513	0.513	0.511	0.62	0.593	0.528	0.602
	-0.095	-0.161	-0.007	-0.076	-0.161	-0.196	-0.126	-0.036	0.076	-0.146	0.018	-0.063	-0.167	-0.06	-0.1	-0.083
r	3.5	3.64	4.06	3.49	3.15	3.9	4.07	4.07	3.27	3.26	3.26	3.25	4.17	3.92	3.37	4
	2.81	2.51	4	2.93	2.17	2.49	3.05	3.75	3.89	2.33	3.39	2.81	2.84	3.42	2.68	3.31

Table 4 – Survey outline for the beginning height. Shower codes are listed in the first line: ORI1 is for the enhanced activity of ORI and ORI2 for the regular years. _SE, _SF1, and _SF2 correspond to STA_SE, enhanced activity of STA_SF and regular years respectively. The two λ_θ give the activity interval, we used the QUA meteors between $\lambda_\theta = 282.6\sim 283.6^\circ$ for example. The two v_g lines give the upper and lower values of the geocentric velocity of sporadic meteors, we selected sporadic meteors between $v_g = 38.4\sim 42.0$ for QUA, that is, in the range of $\pm 1\sigma$ of the mean velocity of QUA.

	QUA	LYR	ETA	SDA	CAP	PER	ORI1	ORI2	_SE	_SF1	_SF2	NTA	LEO	HYD	GEM	COM
λ_θ	282.6	31.9	44	126	125	139.5	206	206	195	218	218	222	234	250	262.5	259
	283.6	32.9	49	130	133	140.5	210	212	205	224	224	234	239	260	263	279
v_g	38.4	44.7	63.6	37.8	20.5	56.5	63.9	63.4	26.3	26.5	25.2	24.7	67.7	56.7	31.8	60.6
	42	48.6	67.6	41.6	24	60.9	68.2	68.2	30.6	30.3	29.7	29.9	72.1	62	35.8	65.3

3.4. Estimate of the magnitude ratio of shower meteors

It may be enough to determine how rich in bright or faint meteors a meteor shower is, by showing the slope of the ratio of shower meteors to sporadic ones. But it is convenient for readers to calculate the magnitude ratio and it is very easy because we have gotten the slopes of major showers and the relation of the slope of sporadic meteors with a given geocentric velocity. We can calculate the magnitude ratio by the formula; $r = 10^{(s_{sh} + s_{sp})}$, where s_{sh} is the slope of the shower meteors to sporadic meteors and s_{sp} is the slope of the sporadic meteors estimated by the relation shown in *Figure 7*.

4 Beginning height

The beginning height of meteors is the clue to understanding the meteoroid properties (Cook, 1973). We investigated the beginning height of 14 major showers according to the conditions shown in *Table 4*.

The widths of the two axes are the same in for all showers, though the ranges of the beginning height (H_B) are different from each other. The result of the linear regression for sporadic meteors is shown as a dashed line (blue) and that of the shower meteors with a solid line (orange), both are shown with the linear expression. We can estimate meteoroid properties for shower meteors by comparing them with the corresponding sporadic ones. If the beginning height of shower meteors is higher than that for the sporadic ones, we can infer that such meteoroids might be more porous than sporadic ones. The results are discussed shower by shower in *Section 5*.

5 Properties discussed by shower

5.1 Quadrantids (QUA#010)

The maximum of Quadrantids is narrow, and meteors classified as Quadrantids in SonotaCo net beyond the 2 days maximum might be contaminated by sporadic meteors or by other minor shower activities such as DAD. The mean absolute magnitude (M_A) drops about 0.5 magnitude at the maximum, brighter meteors become more abundant at the maximum. The changes in the mean magnitude apart from the maximum are very uncertain because of the small number of shower meteors (*Figure 11*).

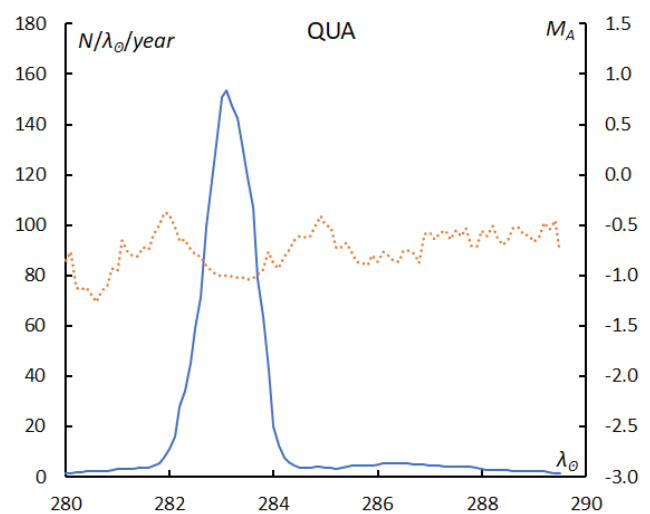


Figure 11 – The sliding mean of the number of Quadrantids (solid line, blue) and of the absolute magnitude (dotted line, orange) using with 1 solar longitude bin; the number is divided by the number of years of the observations.

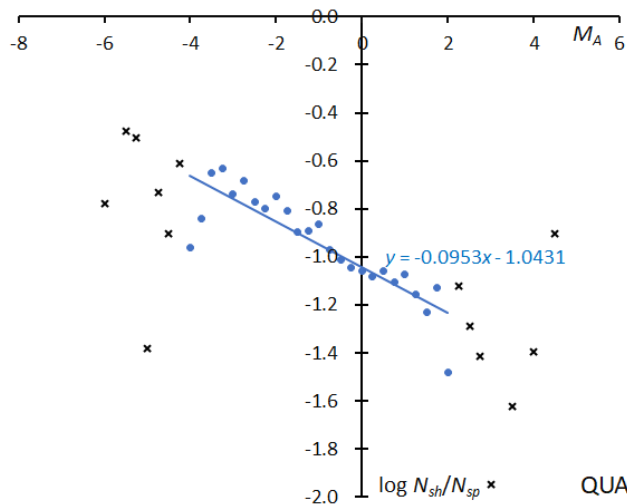


Figure 12 – The solid line indicates the result of the linear regression analysis for the Quadrantids between $M_A = -4 \sim +2$, crosses on both sides are excluded from the analysis because of the scarcity of the data.

The two filled circles on the left side and one in right are lower than the line because of the scarcity of data, but excluded data shown in crosses are consistent with the expected extension of the line. The slope suggests QUA belongs to the ecliptic meteor showers (Figure 12).

The beginning height of QUA is slightly above the sporadic ones (Figure 13). If QUA has common ancestors with SDA, the larger perihelion distance of QUA could be the cause of the difference.

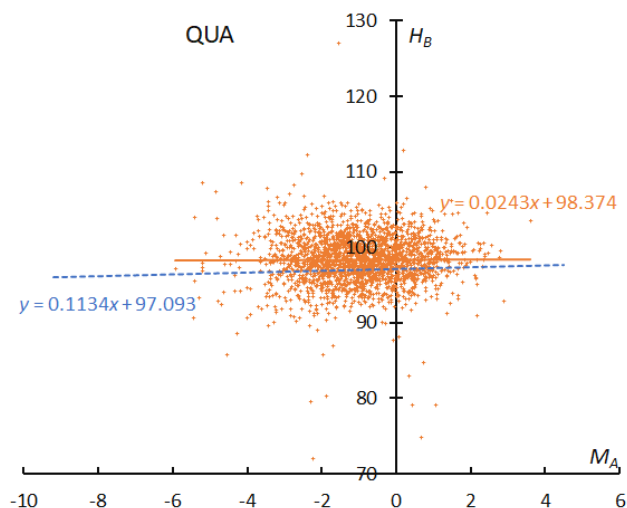


Figure 13 – The result of the linear regression for sporadic meteors is shown as a dashed line, that of the Quadrantids as a solid line.

5.2 Lyrids (LYR#006)

The activity period of Lyrids is also short, and the activity level is lower than for the Quadrantids. The mean magnitude change, therefore, is uncertain but seems to be lower than for the Quadrantids and richer in brighter meteors (Figure 14).

The slope is approximately comparable to CAP and suggests that LYR produces abundantly bright meteors (Figure 15). The beginning height of LYR is clearly higher

than for QUA. The meteoroids of LYR could have a cometary origin and might be more porous than those of QUA (Figure 16).

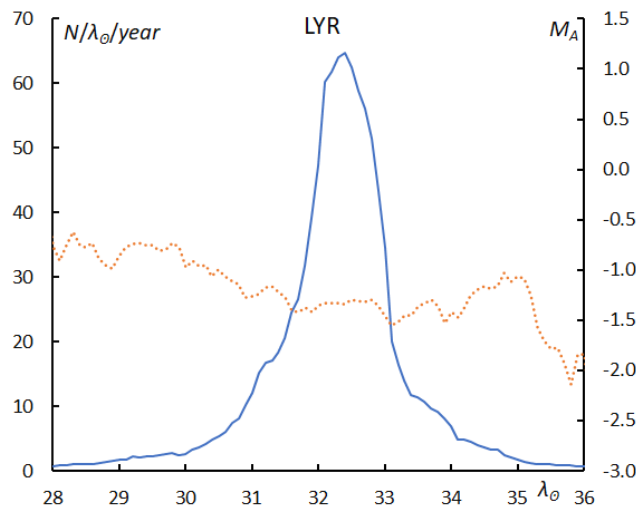


Figure 14 – The sliding mean of the number of Lyrids (solid line, blue) and of the absolute magnitude (dotted line, orange) using with 1 solar longitude bin; the number is divided by the number of years of the observations.

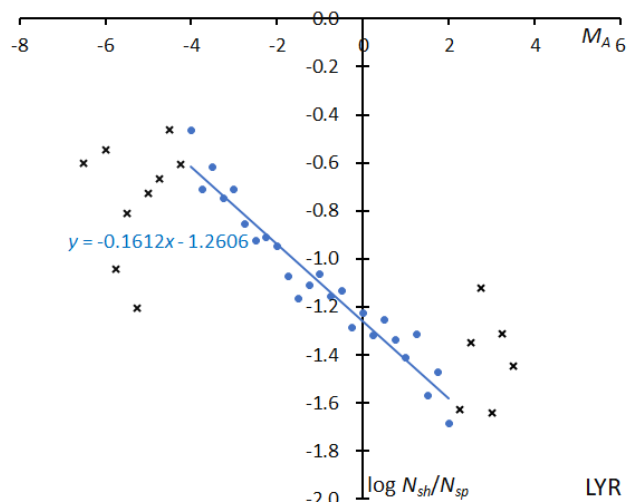


Figure 15 – The solid line indicates the result of the linear regression analysis for the Lyrids between $M_A = -4 \sim +2$, crosses on both sides are excluded from the analysis because of the scarcity of the data.

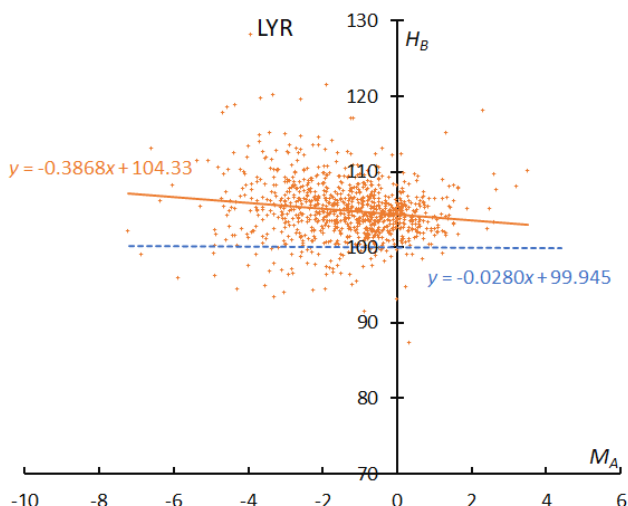


Figure 16 – The result of the linear regression for sporadic meteors is shown as a dashed line, that of the Lyrids as a solid line.

5.3 Eta Aquariids (ETA#031)

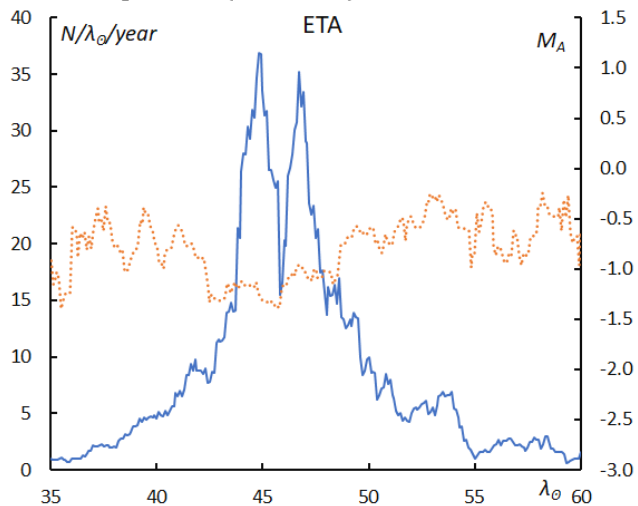


Figure 17 – The sliding mean of the number of eta Aquariids (solid line, blue) and of the absolute magnitude (dotted line, orange) using with 1 solar longitude bin; the number is divided by the number of years of the observations.

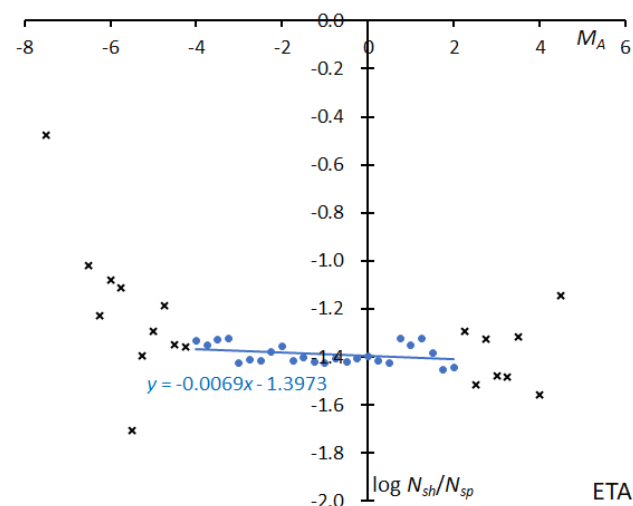


Figure 18 – The solid line indicates the result of the linear regression analysis for the eta Aquariids between $M_A = -4 \sim +2$, crosses on both sides are excluded from the analysis because of the scarcity of the data.

It is obvious that the double maximum is just apparent because of the short observation period in the morning twilight and the weather condition which often distorted the results of the observations. The mean magnitude is lower around the maximum like with the Quadrantids (Figure 17).

The slope is the smoothest among the major showers and is flatter than that of ORI in its regular years. This may be since ETA is farther away from the core of the meteoroid's distribution derived from 1P/Halley than ORI, although the distance between the orbit of ETA and the parent comet is smaller than that of ORI (Figure 18).

The beginning height of ETA is slightly higher than ORI (both enhanced and regular years). This difference may be related to the distance from the orbit of 1P/Halley; the distance between descending nodes of ETA and 1P/Halley is closer than that of the ascending nodes of ORI and the comet (Figure 19).

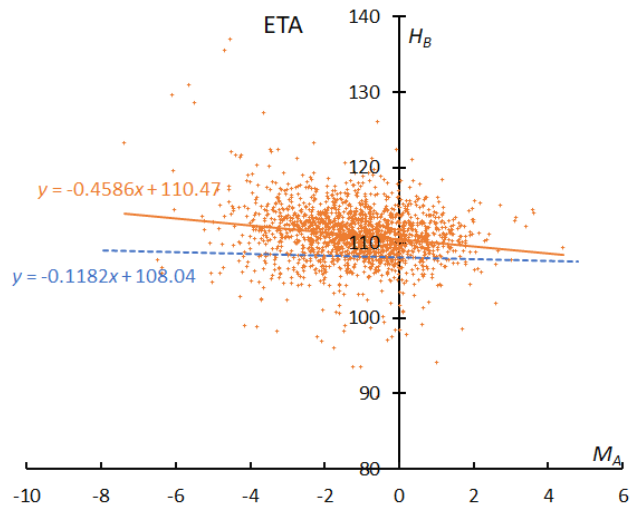


Figure 19 – The result of the linear regression for sporadic meteors is shown as a dashed line, that of the eta Aquariids as a solid line.

5.4 Southern delta Aquariids (SDA#005)

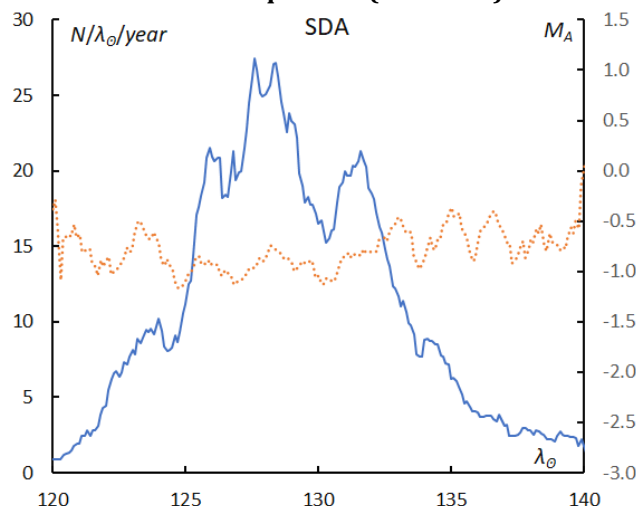


Figure 20 – The sliding mean of the number of Southern delta Aquariids (solid line, blue) and of the absolute magnitude (dotted line, orange) using with 1 solar longitude bin; the number is divided by the number of years of the observations.

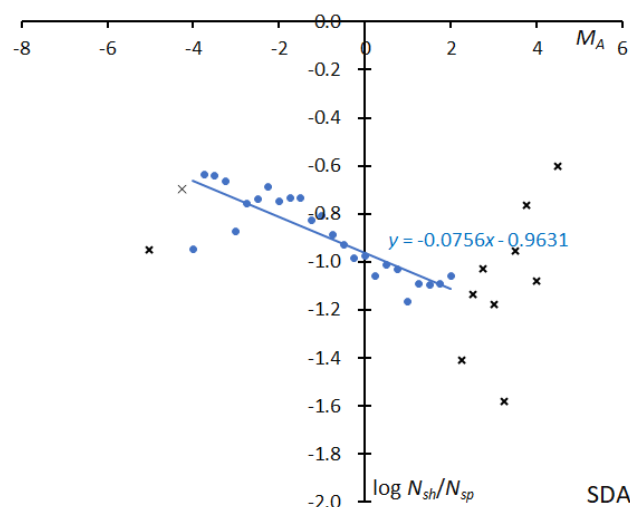


Figure 21 – The solid line indicates the result of the linear regression analysis for the Southern delta Aquariids between $M_A = -4 \sim +2$, crosses on both sides are excluded from the analysis because of the scarcity of the data.

The mean magnitude does not show any distinct brightening around the maximum and is higher, that is, fainter than CAP (Figure 20).

SDA is active in late July at the same time as CAP, but the slopes of the two meteor showers show very well their difference in appearance. SDA meteors appear to be more like QUAs (Figure 21).

SDA is the only meteor shower for which the beginning height is lower than this for the sporadic meteors. The perihelion distance of SDA is the closest to the Sun among all 14 major meteoroid streams, and this might make meteoroids more solid (Figure 22).

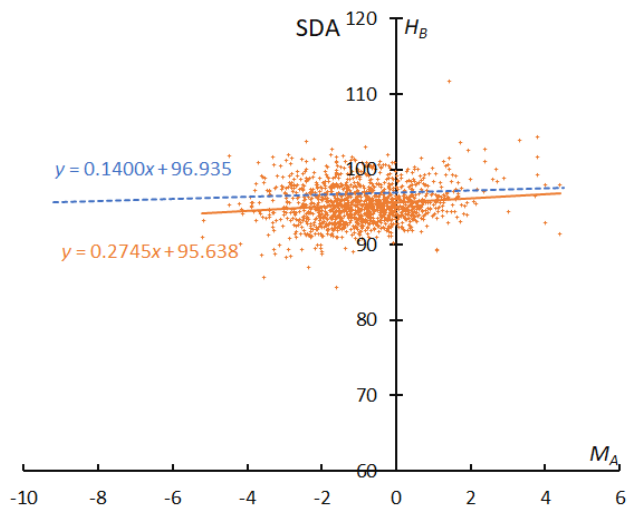


Figure 22 – The result of the linear regression for sporadic meteors is shown as a dashed line, that of the Southern delta Aquariids as a solid line.

5.5 Capricornids (CAP#001)

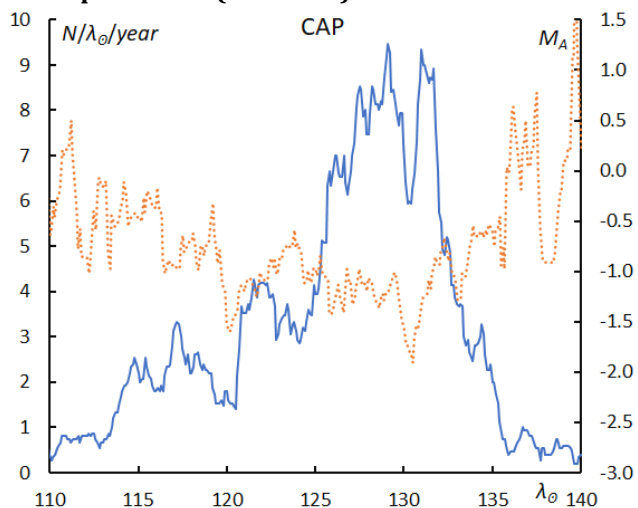


Figure 23 – The sliding mean of the number of Capricornids (solid line, blue) and of the absolute magnitude (dotted line, orange) using with 1 solar longitude bin; the number is divided by the number of years of the observations.

The first half of the activity profile is uncertain because of the bad weather condition in Japan and, therefore, the real maximum might be earlier. The mean magnitude deviates widely and clearly shows brightening around the maximum of the activity (Figure 23).

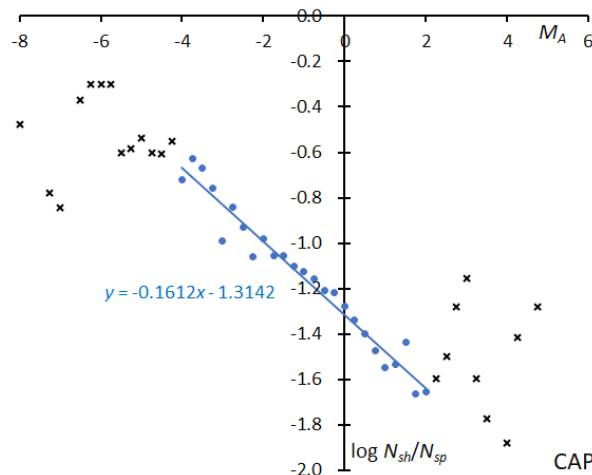


Figure 24 – The solid line indicates the result of the linear regression analysis for the Capricornids between $M_A = -4 \sim +2$, crosses on both sides are excluded from the analysis because of the scarcity of the data.

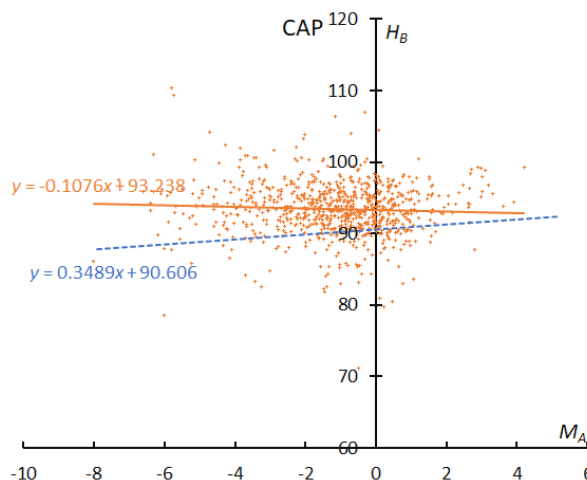


Figure 25 – The result of the linear regression for sporadic meteors is shown as a dashed line, that of the Capricornids as a solid line.

The slope is consistent with our experiences: we know CAP is one of the magnificent meteor showers producing conspicuous fireballs (Figure 24). This may suggest that CAP is of cometary origin, and we encounter the very core of its meteoroid stream such as the Perseids and Leonids.

The beginning height of sporadic meteors is an ascending slope, and this is a common feature in the low-velocity range of meteors (see Figure 25 and other graphs of ecliptic showers). The beginning height of CAP is quite different from SDA and meteoroids of CAP are more fragile than those of SDA.

5.6 Perseids (PER#007)

Perseids are active during more than a month, and the mean magnitude gets brighter around the maximum although it remains in the bright range during the entire activity period (Figure 26).

The magnitude slope is the steepest among all major showers and, therefore, we can enjoy their summer fireworks (Figure 27). The distribution seems to be bulging in the middle; we will study this problem in Section 6.

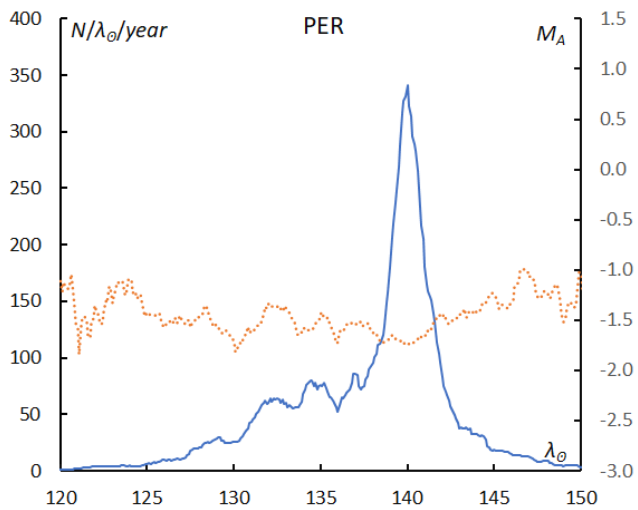


Figure 26 – The sliding mean of the number of Perseids (solid line, blue) and of the absolute magnitude (dotted line, orange) using with 1 solar longitude bin; the number is divided by the number of years of the observations.

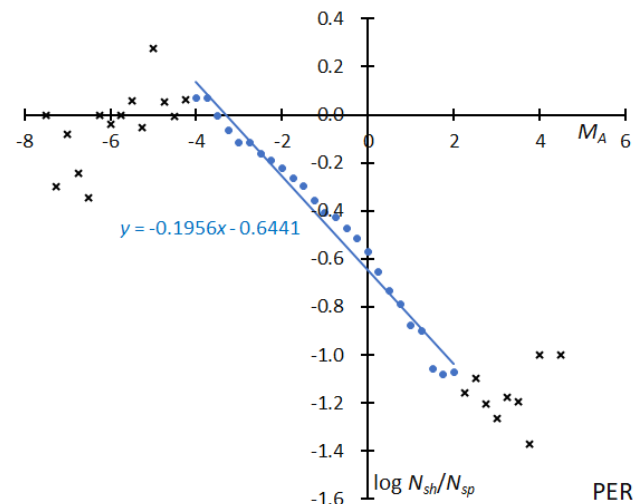


Figure 27 – The solid line indicates the result of the linear regression analysis for the Perseids between $M_A = -4 \sim +2$, crosses on both sides are excluded from the analysis because of the scarcity of the data.

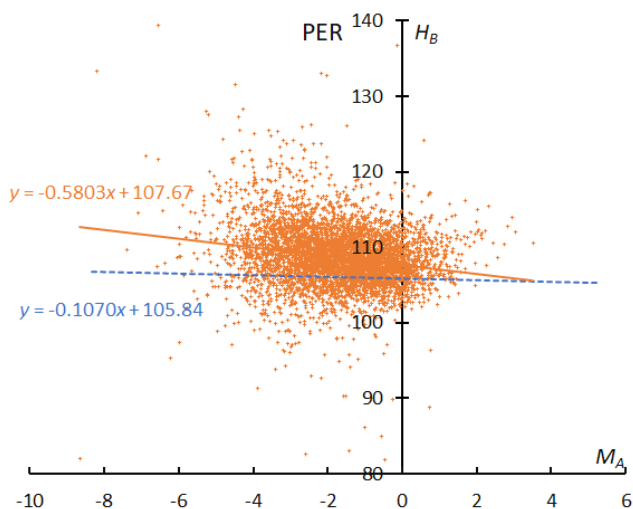


Figure 28 – The result of the linear regression for sporadic meteors is shown as a dashed line, that of the Perseids as a solid line.

The beginning height of the Perseids shows a descending

slope, and this seems to be common for those of cometary origin (see ORI and LEO). The line for the sporadic meteors is flat although we choose the same geocentric velocity range as for PER (Figure 28).

5.7 Orionids (ORI#008)

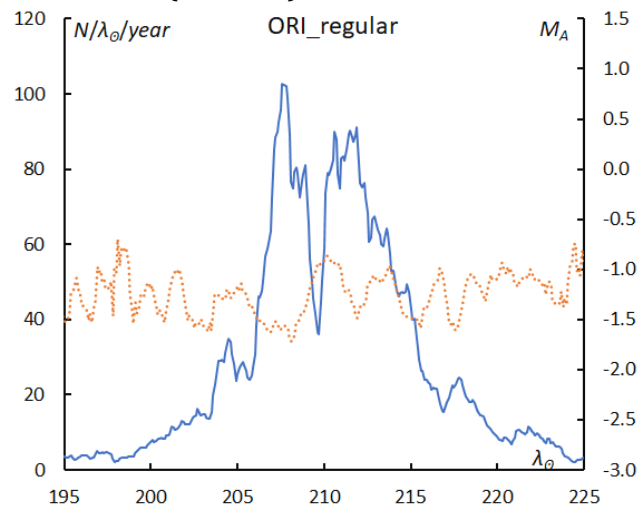


Figure 29 – The sliding mean of the number of Orionids regular activity (solid line, blue) and of the absolute magnitude (dotted line, orange) using with 1 solar longitude bin; the number is divided by the number of years of the observations.

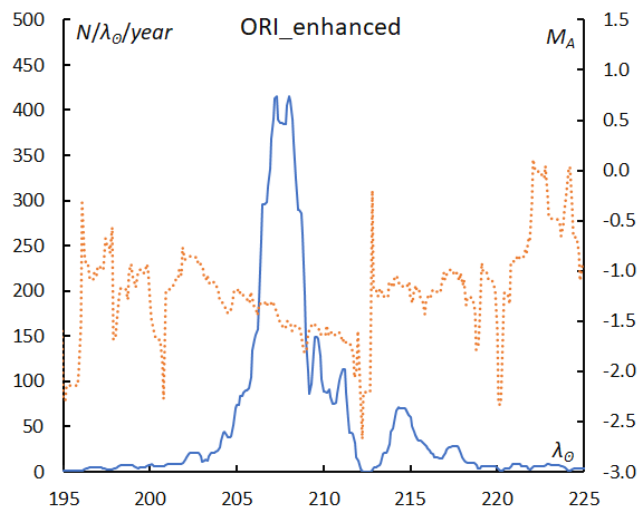


Figure 30 – The sliding mean of the number of Orionids during enhanced activity (solid line, blue) and of the absolute magnitude (dotted line, orange) using with 1 solar longitude bin; the number is divided by the number of years of the observations.

SonotaCo net caught the enhanced activity of Orionids in 2007–09, and, therefore, we divide Orionids data into two parts: the enhanced period (2007–09) and the regular period (2010–22). The Orionids during enhanced years were about five times more abundant in numbers of meteors than in the regular years and with brighter meteors than the latter $\Delta M_A = -0.5 \sim -1.0$. The left wing is different in both plots though the right wing is the same (Figures 29 and 30).

SonotaCo net captured the enhanced activities of ORI in 2007–09. The magnitude distribution in these years is clearly different from the regular years; we were closer to the core of the meteoroid concentration in the enhanced years than in the regular years (Figure 31).

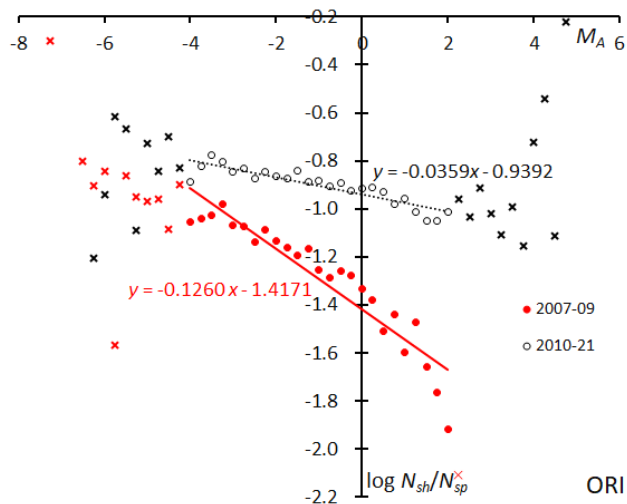


Figure 31 – The solid line indicates the result of the linear regression analysis for the Orionids during enhanced activity, the dotted line for the regular activity, between $M_A = -4 \sim +2$, crosses on both sides are excluded from the analysis because of the scarcity of the data.

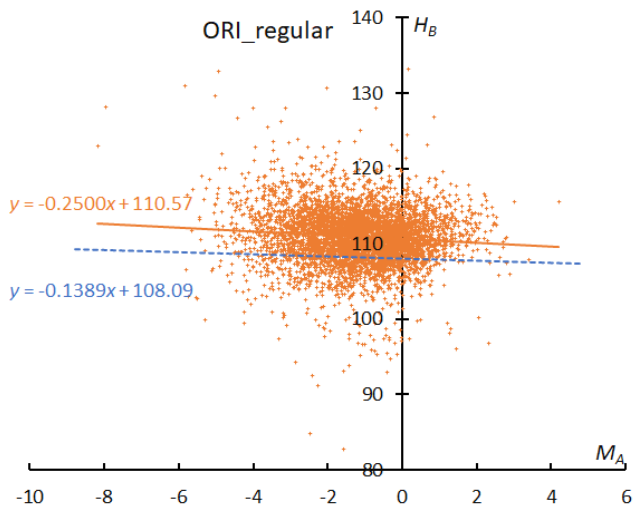


Figure 32 – The result of the linear regression for sporadic meteors is shown as a dashed line, that of the Orionids during regular activity as a solid line.

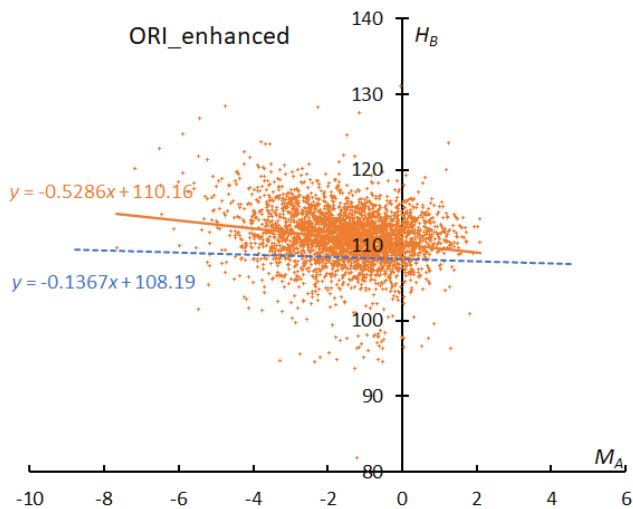


Figure 33 – The result of the linear regression for sporadic meteors is shown as a dashed line, that of the Orionids during enhanced activity as a solid line.

The beginning height of ORI in enhanced years (Figure 33)

clearly shows a descending slope and looks similar like ETA. The regression line for the regular years is even higher than the sporadic one (Figure 32).

5.8 STA_SE (Steady Expression, STA#002)

It is often said that Southern Taurids are active from September to December, but they are composites of ANT activities. We can recognize two distinct meteor showers: STA_SE and STA_SF. We use the code STA for this activity because of the IAU code, although STA_SE is located in Aries. This activity is the second in rank within the so-called STA-activities but the maximum is uncertain ($\lambda_\odot = 203^\circ$) and the mean magnitude is the faintest one among the 14 meteor major showers (Figure 34).

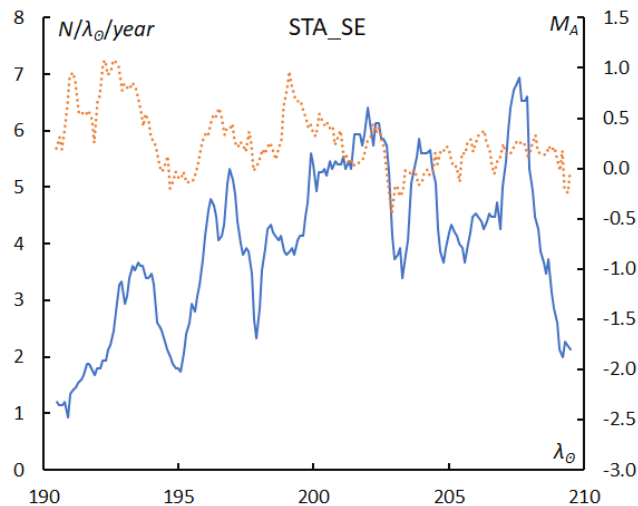


Figure 34 – The sliding mean of the number of Southern Taurids SE activity (solid line, blue) and of the absolute magnitude (dotted line, orange) using with 1 solar longitude bin; the number is divided by the number of years of the observations.

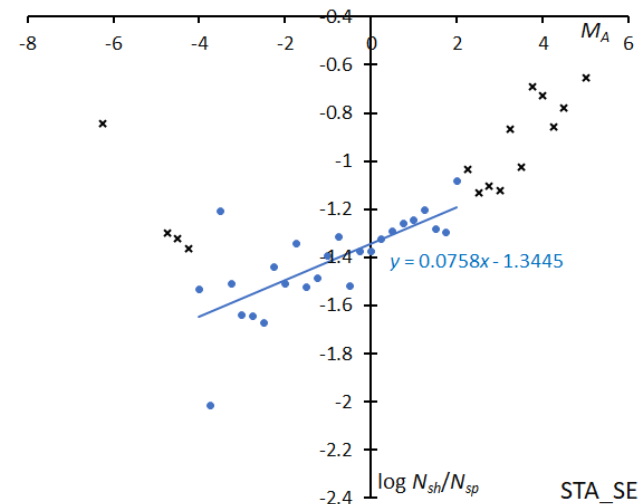


Figure 35 – The solid line indicates the result of the linear regression analysis for the Southern Taurids SE, between $M_A = -4 \sim +2$, crosses on both sides are excluded from the analysis because of the scarcity of the data.

STA_SE is so unique that its magnitude slope shows an ascending slope; this shower is richer in faint meteors than the sporadic activity (Figure 35). It should be stressed we have to distinguish two ‘STA’ components because of the magnitude distribution on top of the difference in the maximum date.

The beginning height of STA_SE is almost parallel to the sporadic one although higher and clearly different from STA_SF (Figure 36).

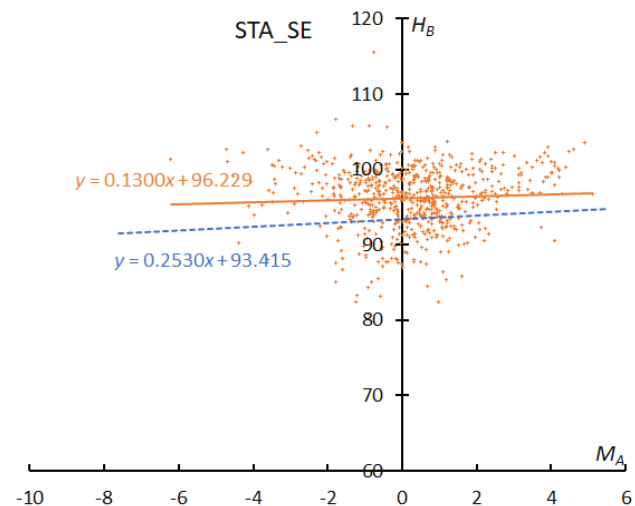


Figure 36 – The result of the linear regression for sporadic meteors is shown as a dashed line, that of the Southern Taurids SE as a solid line.

5.9 STA_SF (Sharply Fluctuating STA#002)

This activity fluctuates from year to year; the enhanced activities were observed in 2008, 2012, 2015, and 2022 although this search was done before the apparition in 2022. Although STA_SF is more active than STA_SE at the maximum ($\lambda_{\odot} = 222^{\circ}$) even during regular years (Figure 37), the meteor rates exceed several times the regular activity level during these enhanced years and the mean magnitude becomes about 1 magnitude brighter (Figure 38).

The magnitude slope during the enhanced years is clearly different from the regular years; this shower produces many fireballs in its enhanced years similar to CAP, though meteors are fainter than NTA and inconspicuous in the regular years (Figure 39).

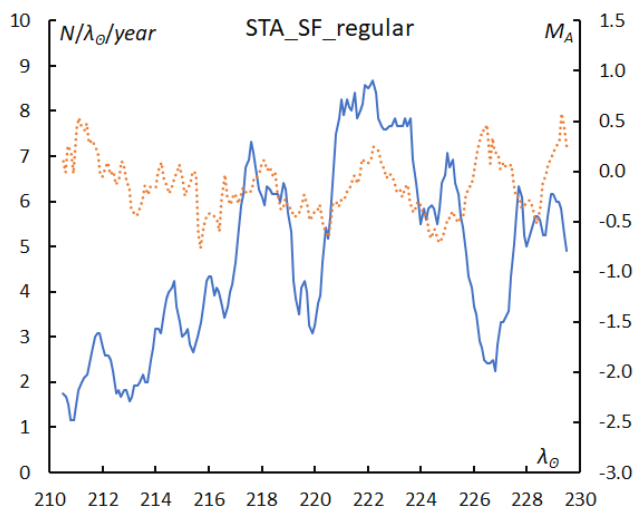


Figure 37 – The sliding mean of the number of Southern Taurids SF regular activity (solid line, blue) and of the absolute magnitude (dotted line, orange) using with 1 solar longitude bin; the number is divided by the number of years of the observations.

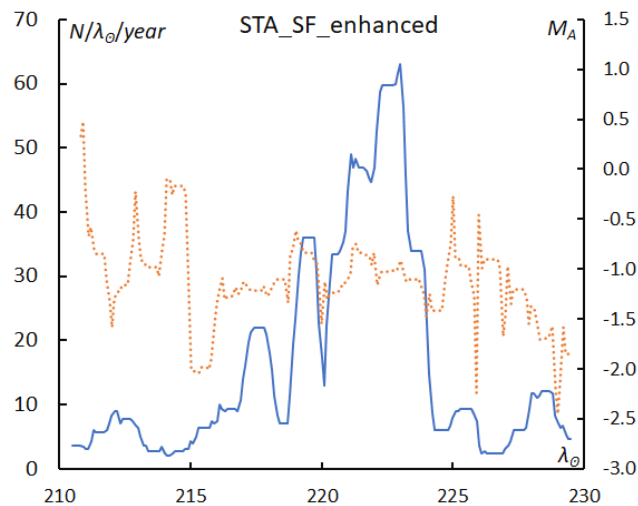


Figure 38 – The sliding mean of the number of Southern Taurids SF enhanced activity (solid line, blue) and of the absolute magnitude (dotted line, orange) using with 1 solar longitude bin; the number is divided by the number of years of the observations.

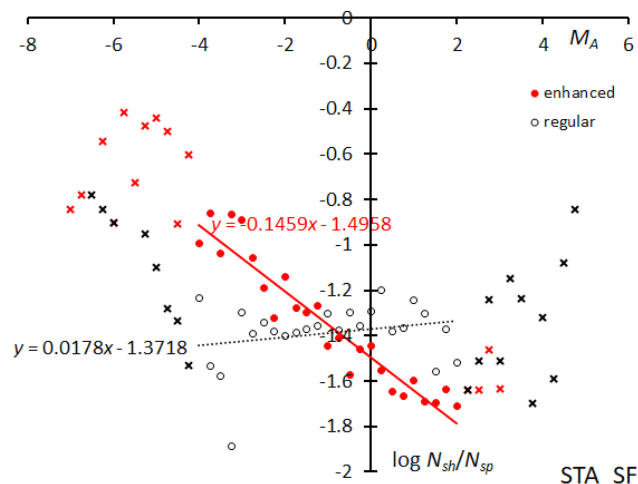


Figure 39 – The solid line indicates the result of the linear regression analysis for the Southern Taurids SF during enhanced activity, the dotted line for the regular activity, between $M_A = -4 \sim +2$, crosses on both sides are excluded from the analysis because of the scarcity of the data.

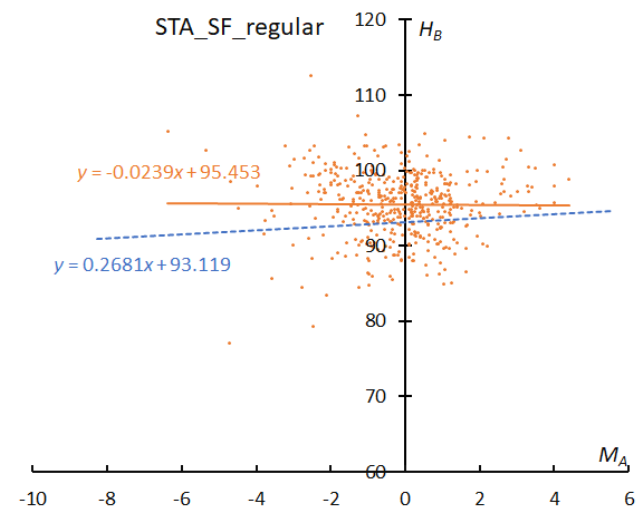


Figure 40 – The result of the linear regression for sporadic meteors is shown as a dashed line, that of the Southern Taurids SF during regular activity as a solid line.

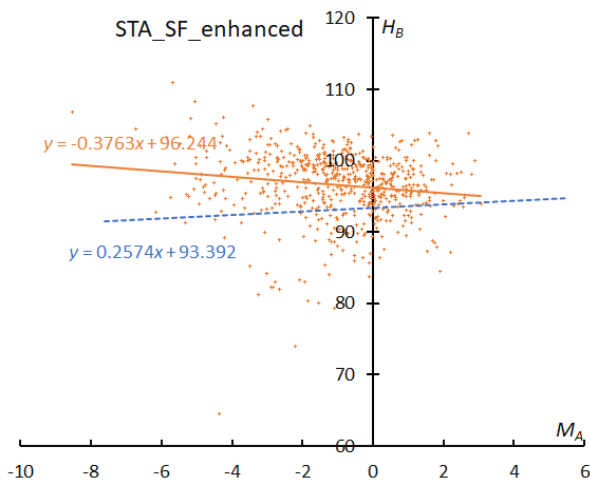


Figure 41 – The result of the linear regression for sporadic meteors is shown as a dashed line, that of the Southern Taurids SF during enhanced activity as a solid line.

The beginning height of enhanced years (Figure 41) clearly shows a descending slope and suggests this activity might be of cometary origin and be near the core of emitted dust. Even the line of regular years (Figure 40) is not an ascending slope like STA_SE shows (Figure 36).

5.10 Northern Taurids (NTA#017)

The activity of NTA continues over a month and shows an uncertain peak around $\lambda_{\odot} = 230^{\circ}$, the activity fluctuates randomly from year to year (Figure 42). The mean magnitude seems brighter than the regular year activity of STA_SF.

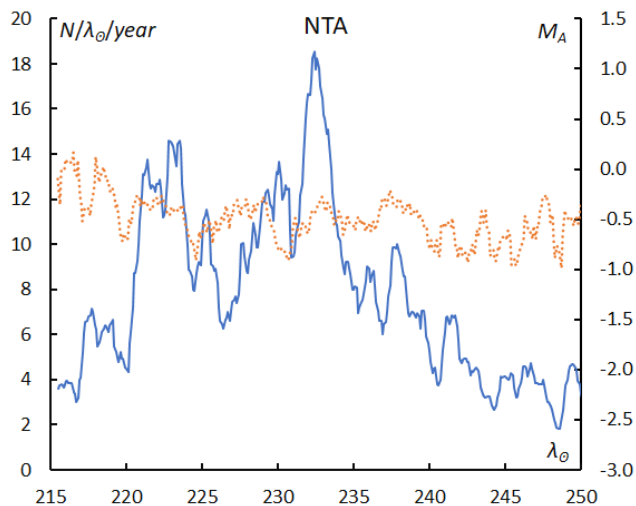


Figure 42 – The sliding mean of the number of Northern Taurids (solid line, blue) and of the absolute magnitude (dotted line, orange) using with 1 solar longitude bin; the number is divided by the number of years of the observations.

Though the magnitude slope suggests that NTA belongs to the ecliptic meteor showers, NTA becomes a central activity of the three Taurids, or, STA_SE, STA_SF, and NTA itself, because NTA has a rather steeper slope (Figure 43).

Figure 44 of the NTA shows an intermediate property between the enhanced and the regular years of STA_SF.

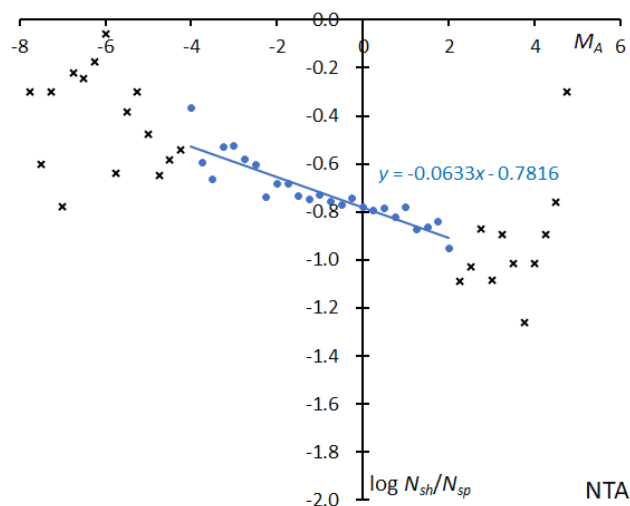


Figure 43 – The solid line indicates the result of the linear regression analysis for the Northern Taurids, between $M_A = -4 \sim +2$, crosses on both sides are excluded from the analysis because of the scarcity of the data.

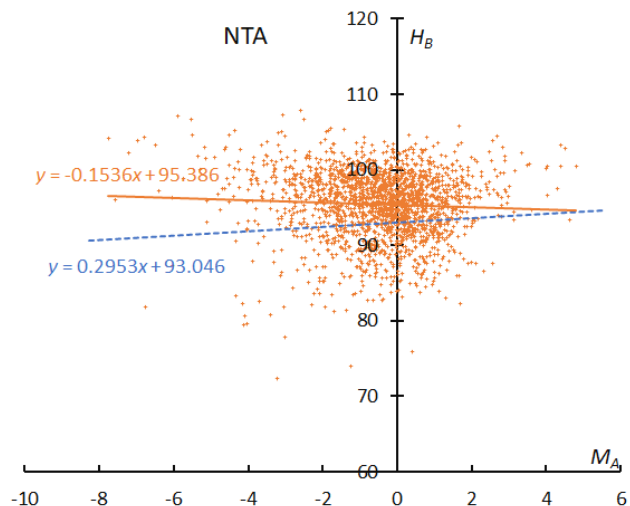


Figure 44 – The result of the linear regression for sporadic meteors is shown as a dashed line, that of the Northern Taurids as a solid line.

5.11 Leonids (LEO#013)

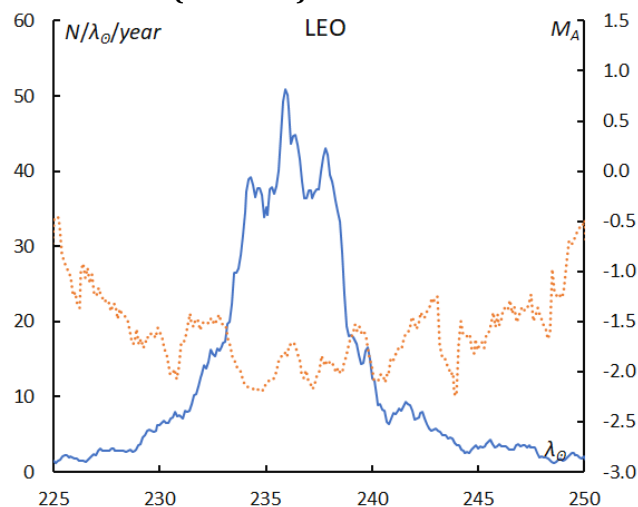


Figure 45 – The sliding mean of the number of Leonids (solid line, blue) and of the absolute magnitude (dotted line, orange) using with 1 solar longitude bin; the number is divided by the number of years of the observations.

Leonids are now in a low activity period, but the mean magnitude shows this is the brightest meteor shower, moreover, the mean magnitude shows distinct brightening around the maximum (Figure 45).

Leonid activity is rather low, but the slope is the second steepest (Figure 46) after the Perseids. We can enjoy several Leonid fireballs during the maximum activity of this shower. The regression line of the Leonids (Figure 47) clearly indicates a cometary origin, although the shower is in a calm period of activity.

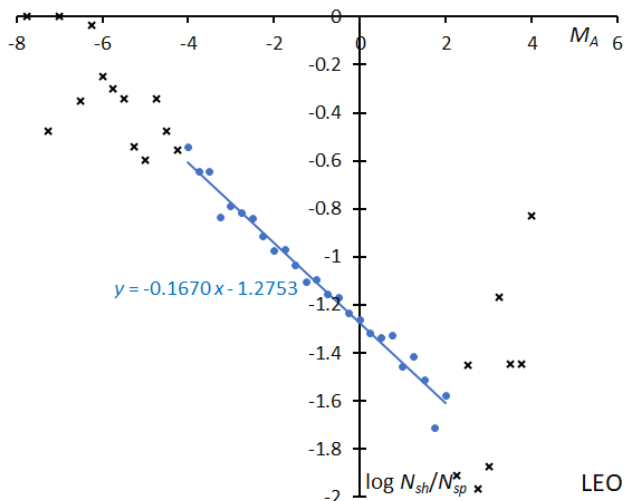


Figure 46 – The solid line indicates the result of the linear regression analysis for the Leonids, between $M_A = -4 \sim +2$, crosses on both sides are excluded from the analysis because of the scarcity of the data.

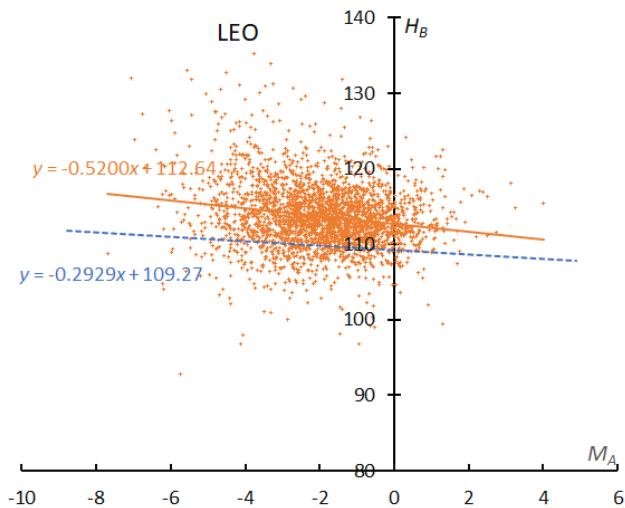


Figure 47 – The result of the linear regression for sporadic meteors is shown as a dashed line, that of Leonids as a solid line.

5.12 Sigma Hydrids (HYD#016)

The activity covers nearly a month. Meteor rates peak around $\lambda_{\odot} = 255^{\circ}$ but the mean magnitude does not show significant changes (Figure 48). The σ -Hydrids seem richer in bright meteors than GEM. The slope is more gentle than in the cases of GEM and COM, although HYD has a Halley-type orbit (Figure 49). The beginning height is slightly above the sporadic ones (Figure 50). The perihelion distance is closer to the Sun than for STA and NTA, and meteoroids of HYD might have lost their fragility.

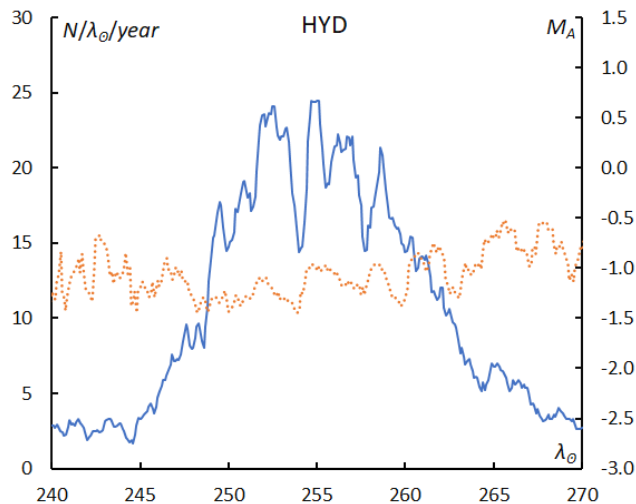


Figure 48 – The sliding mean of the number of sigma Hydrids (solid line, blue) and of the absolute magnitude (dotted line, orange) using with 1 solar longitude bin; the number is divided by the number of years of the observations.

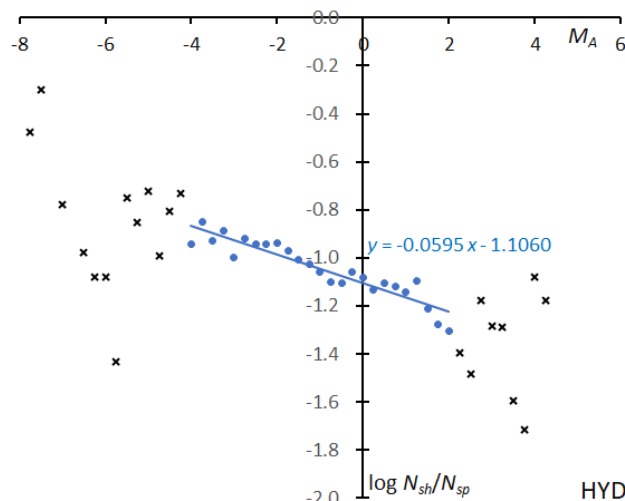


Figure 49 – The solid line indicates the result of the linear regression analysis for the sigma Hydrids, between $M_A = -4 \sim +2$, crosses on both sides are excluded from the analysis because of the scarcity of the data.

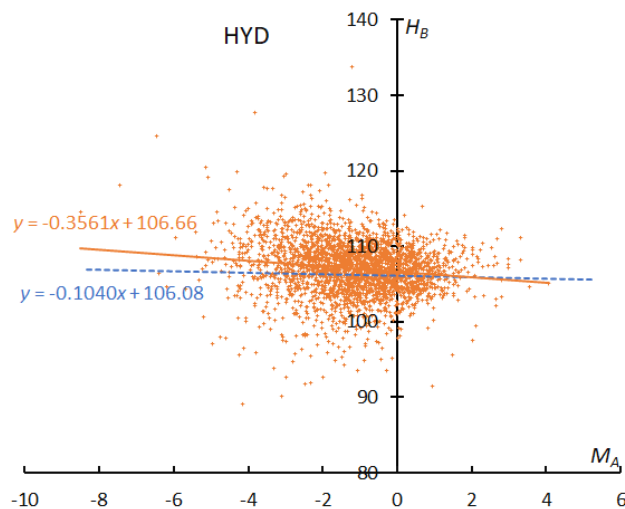


Figure 50 – The result of the linear regression for sporadic meteors is shown as a dashed line, that of the sigma Hydrids as a solid line.

5.13 Geminids (GEM#004)

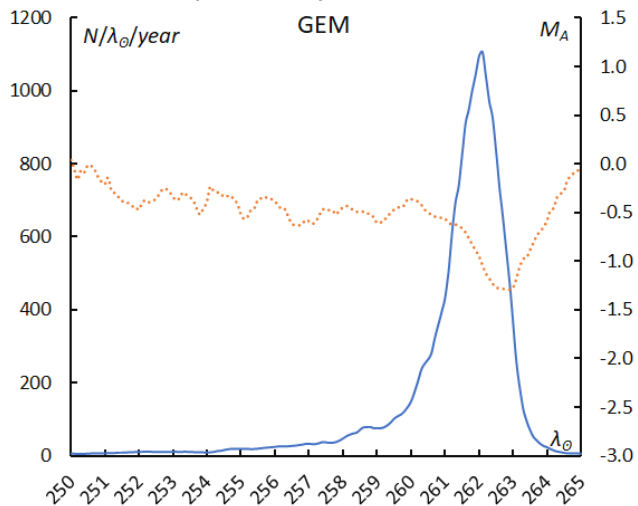


Figure 51 – The sliding mean of the number of Geminids (solid line, blue) and of the absolute magnitude (dotted line, orange) using with 1 solar longitude bin; the number is divided by the number of years of the observations.

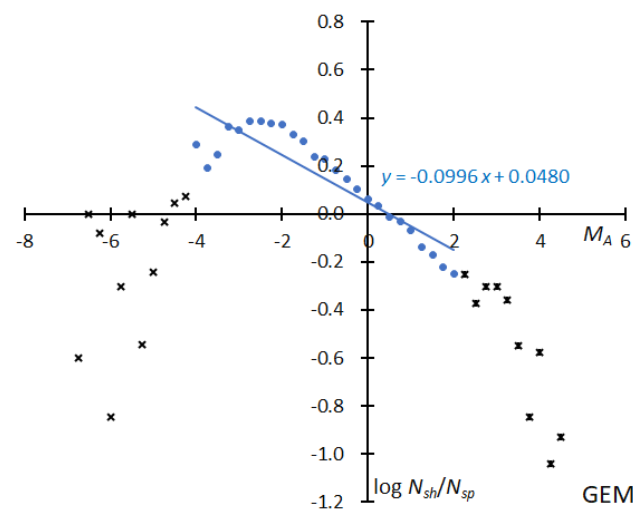


Figure 52 – The solid line indicates the result of the linear regression analysis for the Geminids, between $M_A = -4 \sim +2$, crosses on both sides are excluded from the analysis because of the scarcity of the data.

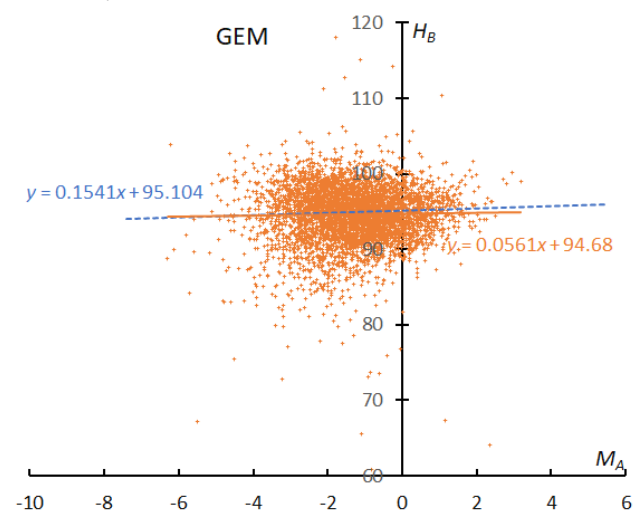


Figure 53 – The result of the linear regression for sporadic meteors is shown as a dashed line, that of the Geminids as a solid line.

It is well known that the peak of brighter Geminids appears later than that of fainter ones. The mean magnitude reaches the minimum after the maximum of the meteor rates (Figure 51). Geminids have other interesting properties, and we study them in Section 6. The magnitude distribution of GEM is unique and suggests that the number of meteors brighter than $M_A < -2$ sharply drops (Figure 52). We will study this in detail in the next section comparing with the Perseids. The regression line of GEM is almost the same as the sporadic one (Figure 53); meteoroids of GEM are not porous like those of cometary origin. The perihelion distance of GEM is the second smallest of the 14 major showers and makes GEM similar in appearance to SDA.

5.14 Comae Berenicids (COM#020)

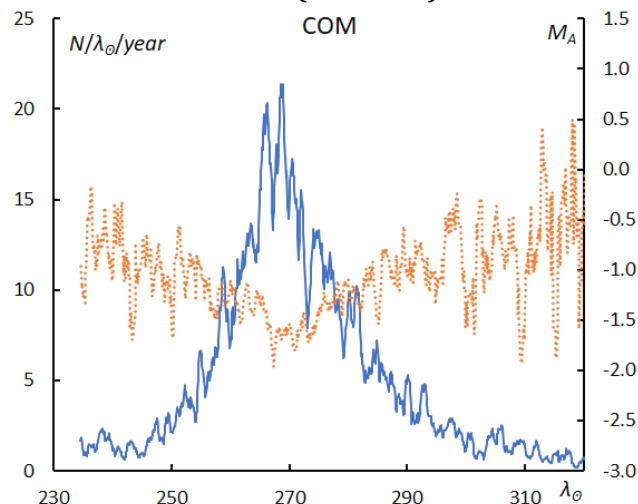


Figure 54 – The sliding mean of the number of Comae Berenicids (solid line, blue) and of the absolute magnitude (dotted line, orange) using with 1 solar longitude bin; the number is divided by the number of years of the observations.

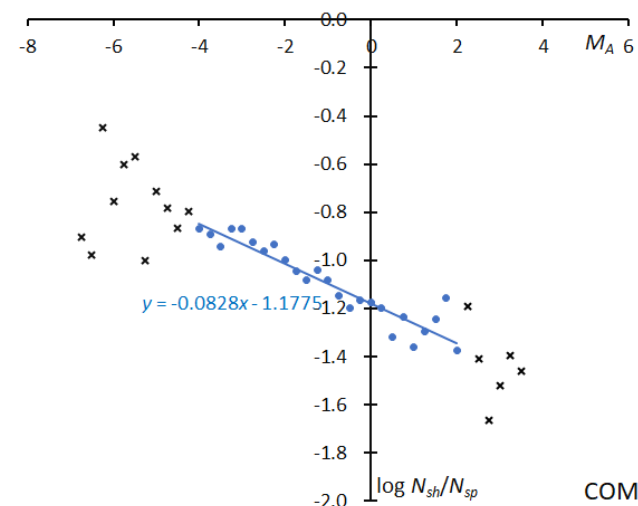


Figure 55 – The solid line indicates the result of the linear regression analysis for the Comae Berenicids, between $M_A = -4 \sim +2$, crosses on both sides are excluded from the analysis because of the scarcity of the data.

Meteor rates reach their maximum around $\lambda_{\odot} = 268^{\circ}$ and the radiant locates in Leo Minor then. The mean magnitude reaches its brightest level at the peak of the activity (Figure 54). COM produces bright meteors like the Perseids do when meteor rates are high, but COM is not so

familiar to visual observers because the meteor rates of COM are much lower than for the Perseids.

COM was detected by photographic observations and is one of the major targets in video observations. Comae Berenicids are richer in bright meteors than sigma Hydrids because the slope is steeper than in the case of sigma Hydrids (Figure 55). COM seems to be a more difficult target for visual observers than HYD.

The regression line for COM is not so high and steeper than the sporadic one, compared to the Perseids and the Leonids (Figure 56). These meteoroids may have lost their fragility because of an old age.

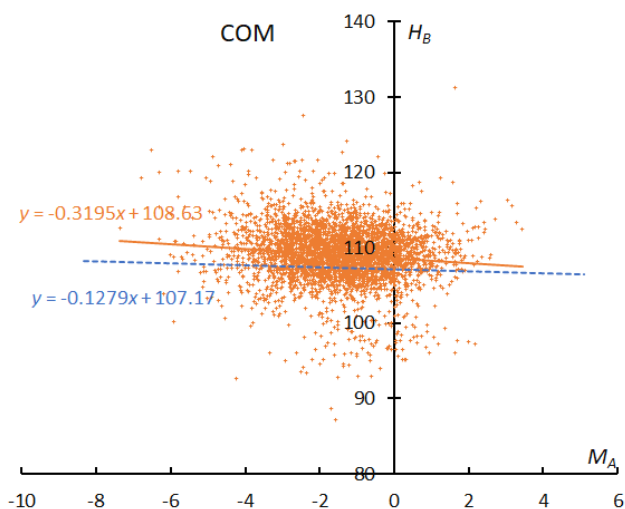


Figure 56 – The result of the linear regression for sporadic meteors is shown as a dashed line, that of the Comae Berenicids as a solid line.

6 The peculiarity of Geminids: comparison with Perseids

The magnitude distribution of the Geminids is unique as pointed out above (see Figure 51). It is not represented as a line but as a smooth curve even if we use the ratio between shower meteors and sporadic meteors (see Figure 52). We study the magnitude distribution of the Geminids in detail in function of the solar longitude compared to the Perseids.

6.1. Magnitude distribution of the Perseids in function of solar longitude

We divide the data into 24 groups with 1000 meteors each in function of the solar longitude and show the magnitude distributions of 24 groups in Figures 58–63. The first graph represents the first four groups: $\lambda_{\theta} = 124.51^{\circ}$, $\lambda_{\theta} = 129.59^{\circ}$, $\lambda_{\theta} = 131.49^{\circ}$, and $\lambda_{\theta} = 132.59^{\circ}$, each given as the mean solar longitude of the meteors within the interval with 1000 meteors (Figure 58). These four plots are in good agreement with each other. The following five graphs are similar. We calculate the slopes of the range between $M_A = -4 \sim +2$ to study the change of the slopes in function of the solar longitude; the range could be extended to a brighter magnitude of $M_A < -4$, however the numbers of meteors are small. It is unclear why these lines seem to bend and increase after $M_A > +2$, the trains left by Perseid

meteors may make them easier to record than sporadic meteors, anyway the number of meteors is rather low.

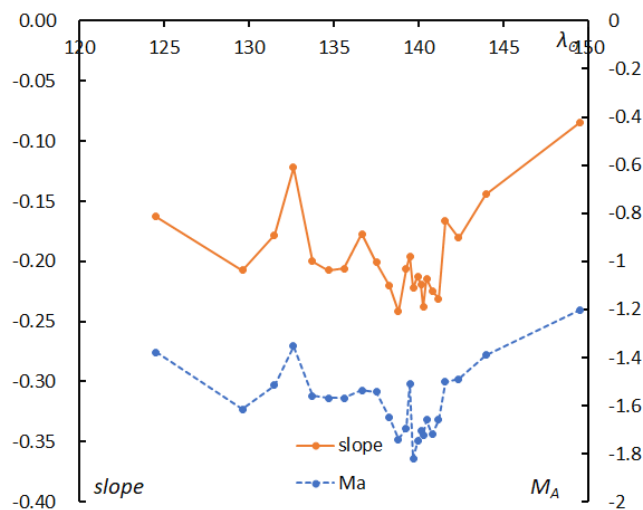


Figure 57 – The change of the magnitude distribution slopes of the Perseids in function of solar longitude compared with the mean magnitude shift. The slope (solid line) changes synchronously with the mean magnitude (dashed line).

The slopes change with time and reach the deepest point during the maximum (Figure 57); we can calculate the magnitude ratio easily as mentioned above and the summary results are given in Table 5. We also realize that this change coincides with the shift of the mean absolute magnitude calculated for the same solar longitude period using the slope. This is the explanation for the bulging seen with the Perseids in Figure 27. Almost all meteor showers show the smallest mean absolute magnitude at their maximum activity (see Figures 11, 14, 17, 20, 23, 26, 29, 30, 34, 37, 38, 42, 45, 48, 51 and 54). It is difficult to confirm the universal correlation of the mean absolute magnitude with the slope of the logarithm distribution of the ratio of shower meteors to the sporadic ones because dividing the data into enough sizes to analyze the change of the slopes is difficult for other meteor showers, except for Geminids and Perseids. We may assume that the change of the slope with time as seen in the Perseids is similar for other showers.

5.2. Magnitude distribution of the Geminids in function of solar longitude

We divide the data into 35 groups with 1000 meteors each in function of the solar longitude and show the magnitude distribution in Figures 64–72. The first graph represents the first four groups: $\lambda_{\theta} = 249.71$, $\lambda_{\theta} = 256.35$, $\lambda_{\theta} = 258.28$, and $\lambda_{\theta} = 259.20$ given as the mean solar longitude for each time bin with 1000 meteors (Figure 64). We calculate the slopes of the range between $M_A = -2 \sim +2$ to study the change of the slope in function of the solar longitude; the lines clearly change with time and the curved profiles do not permit us to use a wider magnitude range like we did for the Perseids. The summary results for the Geminids are given in Table 6. We focus on the two differences between Perseids and Geminids: the large fluctuation range of the slopes and the mean magnitude, and the curved profiles brighter than $M_A < -2$.

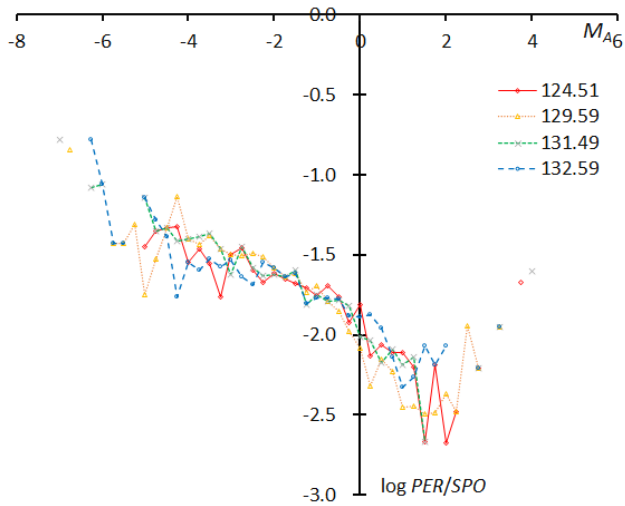


Figure 58 – The magnitude distributions of the Perseids for the time bins with 1000 meteors at $\lambda_0 = 124.51^\circ$, $\lambda_0 = 129.59^\circ$, $\lambda_0 = 131.49^\circ$, and $\lambda_0 = 132.59^\circ$.

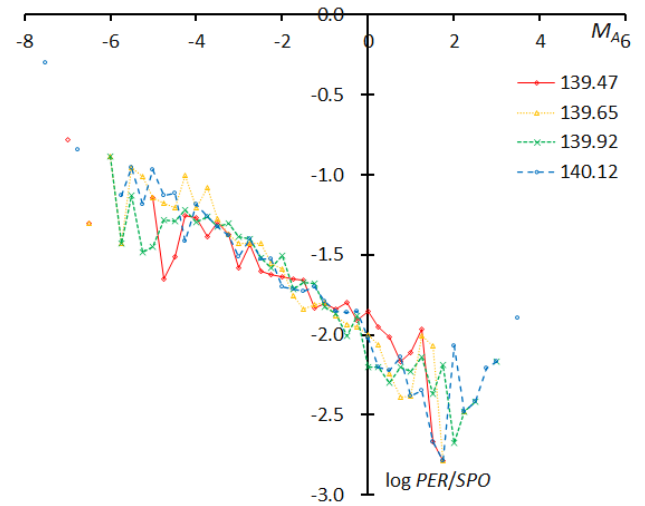


Figure 61 – The magnitude distributions of the Perseids for the time bins with 1000 meteors at $\lambda_0 = 139.47^\circ$, $\lambda_0 = 139.65^\circ$, $\lambda_0 = 139.92^\circ$, and $\lambda_0 = 140.12^\circ$.

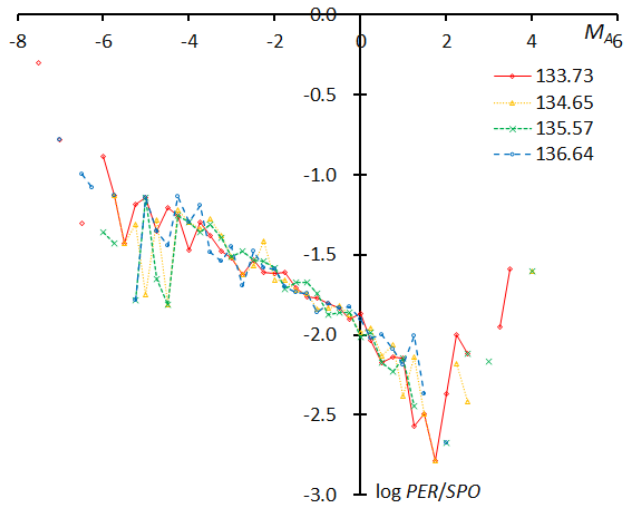


Figure 59 – The magnitude distributions of the Perseids for the time bins with 1000 meteors at $\lambda_0 = 133.73^\circ$, $\lambda_0 = 134.65^\circ$, $\lambda_0 = 135.57^\circ$, and $\lambda_0 = 136.64^\circ$.

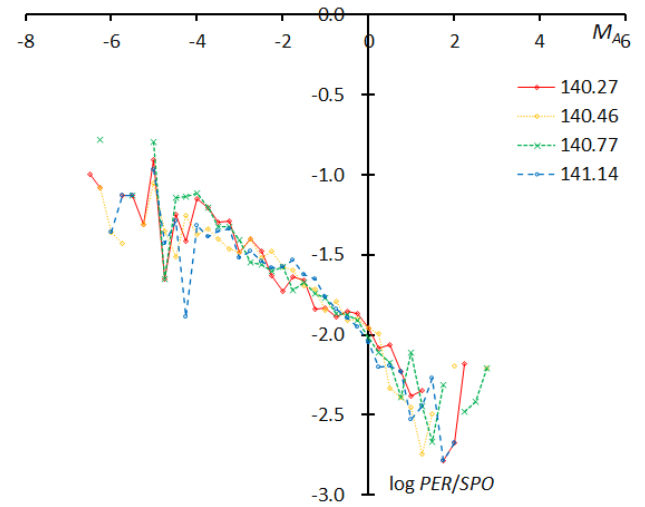


Figure 62 – The magnitude distributions of the Perseids for the time bins with 1000 meteors at $\lambda_0 = 140.27^\circ$, $\lambda_0 = 140.46^\circ$, $\lambda_0 = 140.77^\circ$, and $\lambda_0 = 141.14^\circ$.

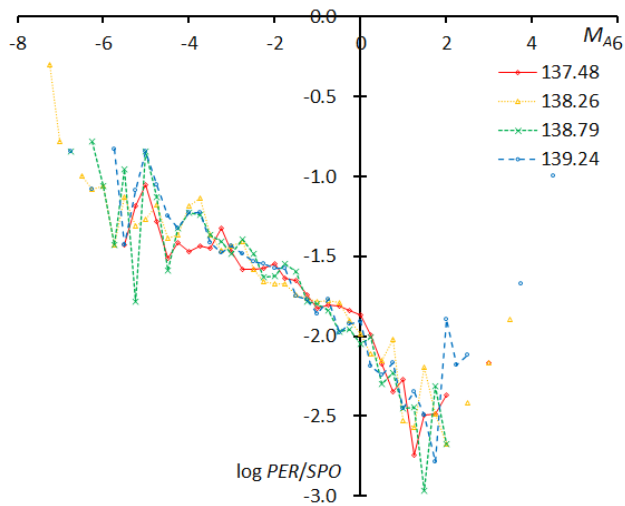


Figure 60 – The magnitude distributions of the Perseids for the time bins with 1000 meteors at $\lambda_0 = 137.48^\circ$, $\lambda_0 = 138.26^\circ$, $\lambda_0 = 138.79^\circ$, and $\lambda_0 = 139.24^\circ$.

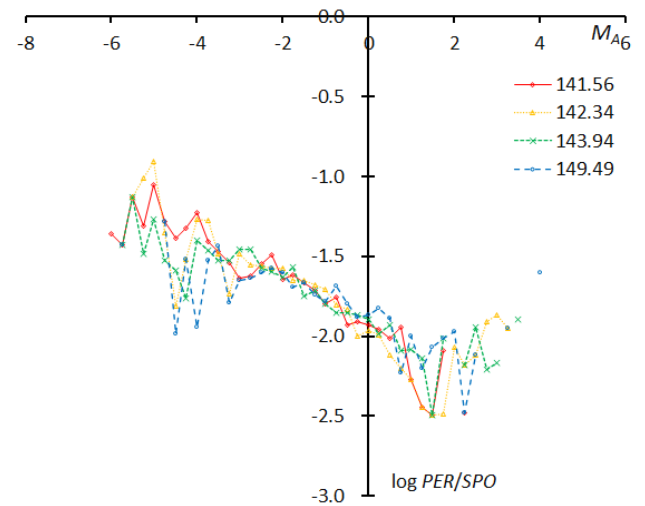


Figure 63 – The magnitude distributions of the Perseids for the time bins with 1000 meteors at $\lambda_0 = 141.56^\circ$, $\lambda_0 = 142.34^\circ$, $\lambda_0 = 143.94^\circ$, and $\lambda_0 = 149.49^\circ$.

Table 5 – The changes for the Perseids in the slope, the magnitude ratio (r), and the mean absolute magnitude (M_A) along with solar longitude (λ_θ).

λ_θ (°)	124.51	129.59	131.49	132.59	133.73	134.65	135.57	136.64	137.48	138.26	138.79	139.24
slope	-0.163	-0.208	-0.178	-0.122	-0.2	-0.207	-0.206	-0.177	-0.201	-0.22	-0.242	-0.206
r	2.68	2.42	2.59	2.95	2.46	2.42	2.43	2.6	2.46	2.35	2.24	2.43
M_A	-1.38	-1.62	-1.51	-1.35	-1.56	-1.57	-1.57	-1.54	-1.54	-1.65	-1.74	-1.69
λ_θ (°)	139.47	139.65	139.92	140.12	140.27	140.46	140.77	141.14	141.56	142.34	143.94	149.49
slope	-0.196	-0.222	-0.212	-0.22	-0.238	-0.214	-0.225	-0.231	-0.166	-0.18	-0.144	-0.084
r	2.49	2.34	2.39	2.35	2.26	2.38	2.33	2.29	2.66	2.58	2.8	3.22
M_A	-1.51	-1.82	-1.75	-1.7	-1.72	-1.66	-1.72	-1.66	-1.5	-1.49	-1.39	-1.2

Table 6 – The changes for the Geminids in the slope, the magnitude ratio (r), and the mean absolute magnitude (M_A) along with solar longitude (λ_θ).

λ_θ (°)	249.71	256.35	258.28	259.2	259.89	260.32	260.6	260.76	260.95	261.13	261.26	261.39
slope	-0.008	-0.092	-0.09	-0.122	-0.04	-0.003	-0.047	-0.06	-0.142	-0.137	-0.089	-0.102
r	3.31	2.73	2.74	2.54	3.08	3.35	3.02	2.94	2.43	2.46	2.74	2.67
M_A	-0.23	-0.52	-0.44	-0.6	-0.37	-0.34	-0.44	-0.53	-0.72	-0.63	-0.46	-0.55
λ_θ (°)	261.5	261.57	261.62	261.67	261.71	261.76	261.83	261.91	261.97	262.02	262.08	262.14
slope	-0.142	-0.181	-0.171	-0.079	-0.119	-0.133	-0.232	-0.194	-0.173	-0.203	-0.244	-0.326
r	2.43	2.22	2.28	2.81	2.57	2.48	1.97	2.16	2.26	2.11	1.92	1.59
M_A	-0.57	-0.73	-0.7	-0.58	-0.65	-0.67	-0.82	-0.74	-0.81	-0.91	-0.93	-1.12
λ_θ (°)	262.21	262.28	262.35	262.41	262.47	262.53	262.59	262.67	262.78	262.97	264.77	
slope	-0.367	-0.298	-0.273	-0.295	-0.237	-0.294	-0.361	-0.348	-0.267	-0.253	-0.129	
r	1.45	1.7	1.8	1.71	1.95	1.71	1.47	1.51	1.82	1.88	2.51	
M_A	-1.27	-1.24	-1.23	-1.2	-1.3	-1.25	-1.44	-1.47	-1.34	-1.3	-0.75	

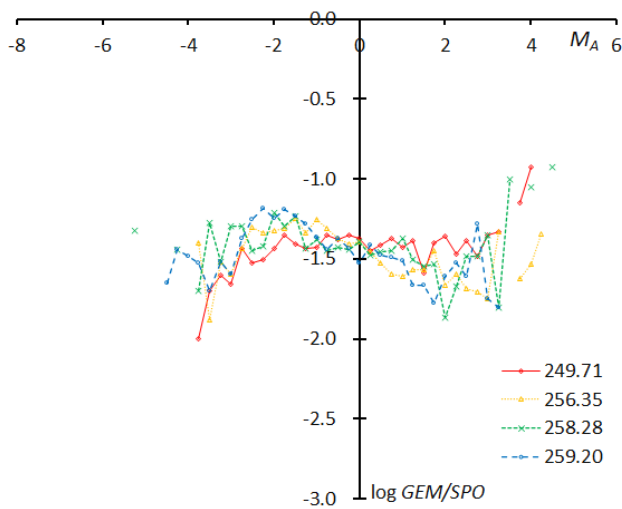


Figure 64 – The magnitude distributions of the Geminids for the time bins with 1000 meteors at $\lambda_\theta = 249.71^\circ$, $\lambda_\theta = 256.35^\circ$, $\lambda_\theta = 258.28^\circ$, and $\lambda_\theta = 259.20^\circ$.

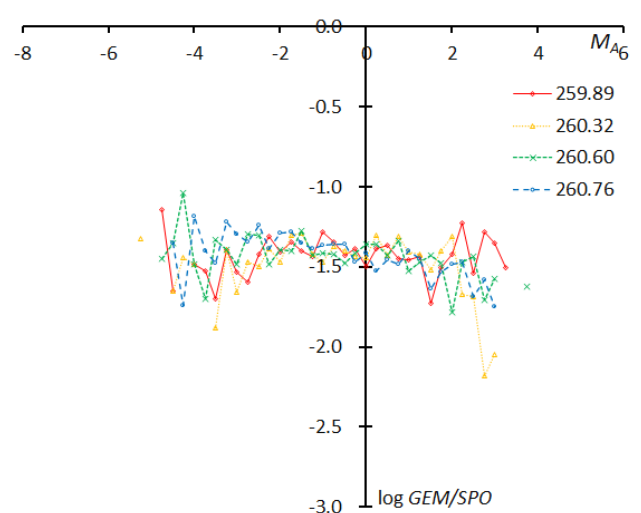


Figure 65 – The magnitude distributions of the Geminids for the time bins with 1000 meteors at $\lambda_\theta = 259.89^\circ$, $\lambda_\theta = 260.32^\circ$, $\lambda_\theta = 260.60^\circ$, and $\lambda_\theta = 260.76^\circ$.

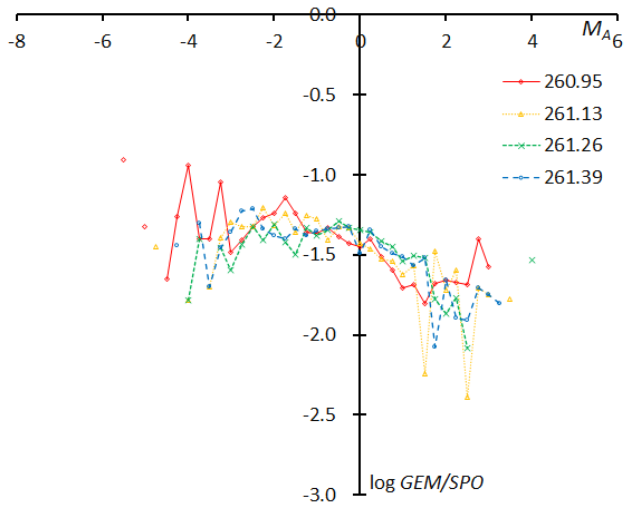


Figure 66 – The magnitude distributions of the Geminids for the time bins with 1000 meteors at $\lambda_{\theta} = 260.95^{\circ}$, $\lambda_{\theta} = 261.13^{\circ}$, $\lambda_{\theta} = 261.26^{\circ}$, and $\lambda_{\theta} = 261.39^{\circ}$.

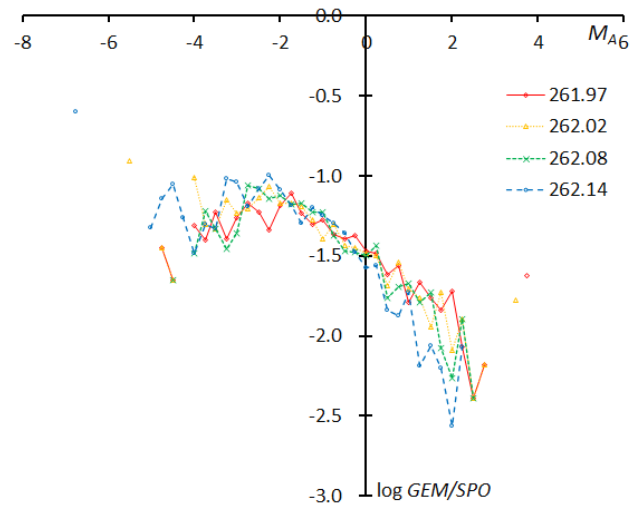


Figure 69 – The magnitude distributions of the Geminids for the time bins with 1000 meteors at $\lambda_{\theta} = 261.97^{\circ}$, $\lambda_{\theta} = 262.02^{\circ}$, $\lambda_{\theta} = 262.08^{\circ}$, and $\lambda_{\theta} = 262.14^{\circ}$.

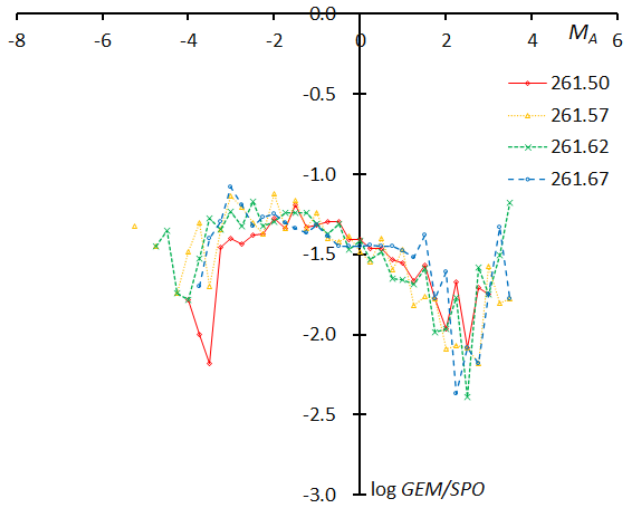


Figure 67 – The magnitude distributions of the Geminids for the time bins with 1000 meteors at $\lambda_{\theta} = 261.50^{\circ}$, $\lambda_{\theta} = 261.57^{\circ}$, $\lambda_{\theta} = 261.62^{\circ}$, and $\lambda_{\theta} = 261.67^{\circ}$.

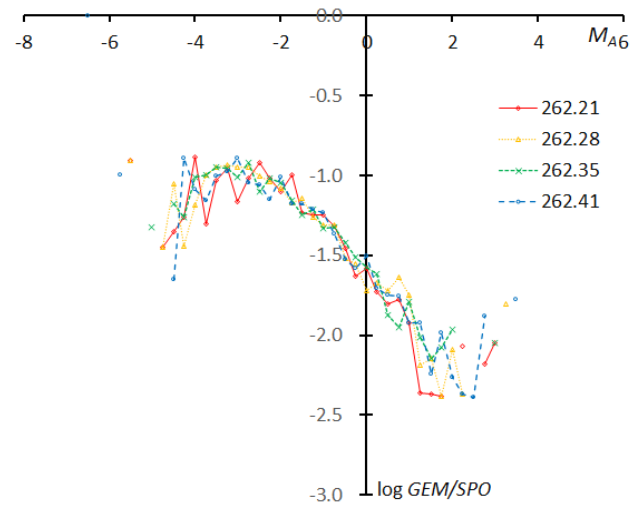


Figure 70 – The magnitude distributions of the Geminids for the time bins with 1000 meteors at $\lambda_{\theta} = 262.21^{\circ}$, $\lambda_{\theta} = 262.28^{\circ}$, $\lambda_{\theta} = 262.35^{\circ}$, and $\lambda_{\theta} = 262.41^{\circ}$.

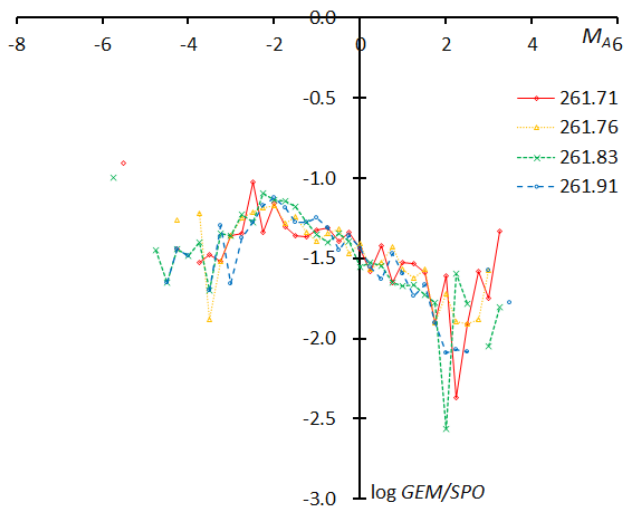


Figure 68 – The magnitude distributions of the Geminids for the time bins with 1000 meteors at $\lambda_{\theta} = 261.71^{\circ}$, $\lambda_{\theta} = 261.76^{\circ}$, $\lambda_{\theta} = 261.83^{\circ}$, and $\lambda_{\theta} = 261.91^{\circ}$.

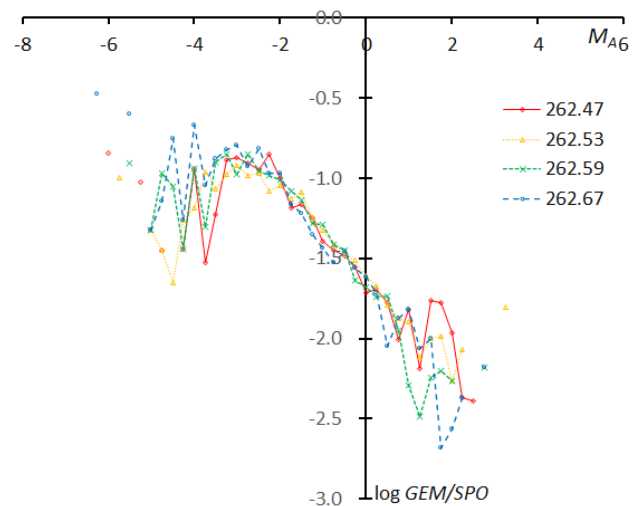


Figure 71 – The magnitude distributions of the Geminids for the time bins with 1000 meteors at $\lambda_{\theta} = 262.47^{\circ}$, $\lambda_{\theta} = 262.53^{\circ}$, $\lambda_{\theta} = 262.59^{\circ}$, and $\lambda_{\theta} = 262.67^{\circ}$.

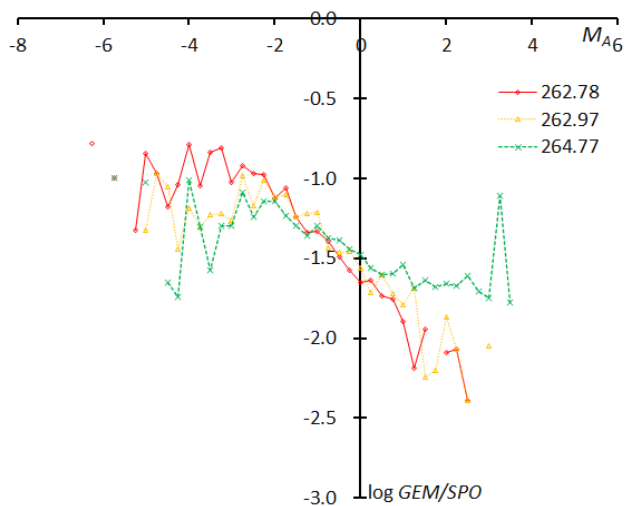


Figure 72 – The magnitude distributions of the Geminids for the time bins with 1000 meteors at $\lambda_{\theta} = 262.78^{\circ}$, $\lambda_{\theta} = 262.97^{\circ}$, and $\lambda_{\theta} = 264.77^{\circ}$.

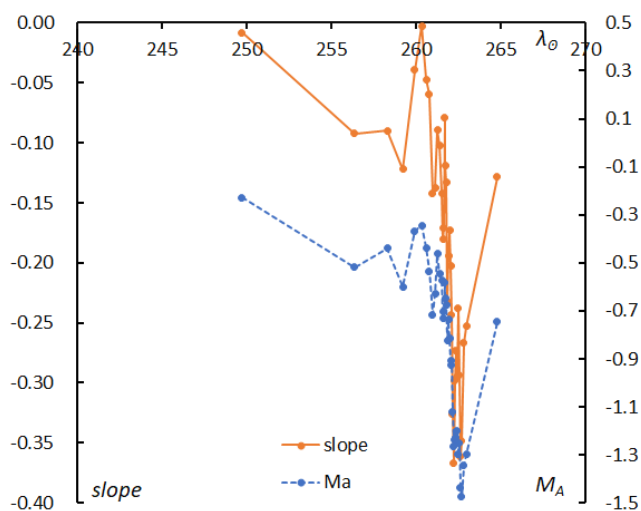


Figure 73 – The change of the magnitude distribution slopes of the Geminids in function of solar longitude compared with the mean magnitude shift. The slope (solid line) changes synchronous with the mean magnitude (dashed line).

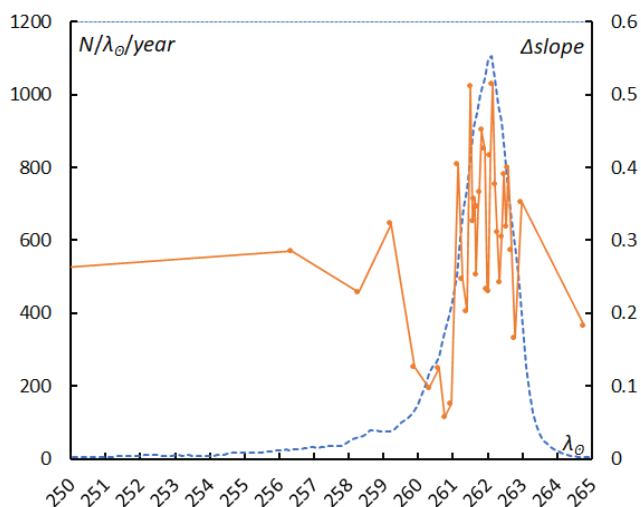


Figure 74 – The change of the difference in the slopes ($M_A = -2 \sim +2$ and $M_A = -4 \sim -2$) along with solar longitude compared with the activity profile of Geminids.

The changes in the slopes of the magnitude distribution are

related to the change in the mean absolute magnitude, and the slope reaches the lowest value a little while after the activity maximum the same way the mean absolute magnitude does (Figure 73). Both curves show a larger and more drastically fluctuation than in the case of the Perseids. We can compare Figure 73 with Figure 57 visually as both are drawn on the same scale. This is the first point; the plot appears narrow and steep.

The second point is the inflection of the graph around $M_A = -2$ (see Figures 64–72). Though we can recognize this in figures, the changes in the slope between $M_A = -4 \sim -2$ represent the peculiarity of Geminids more clearly. We calculate the difference between the two slopes, the reference slope for the Geminids ($M_A = -2 \sim +2$) and the targeted slope ($M_A = -4 \sim -2$). Both are positive over the entire period, that is, the graph is always convex. Figure 74 compares this difference in the slope with the activity profile. The fluctuations occur around the activity maximum, the difference of over 0.4 means that the bending angle is about 20 degrees. It is noteworthy to point out that brighter meteors $M_A < -2$ in the Geminids decrease in number instead of increasing and, moreover, this tendency is remarkable at the activity maximum.

7 Discussions

Video observations have problems not only with their photometric techniques but also with the perception depending on the magnitude and the geocentric velocity of meteors. It should be stressed that this research is based on SonotaCo net data and that the magnitude distributions of sporadic meteors differ depending on observational techniques (Koseki, 2015). Therefore, the slopes shown in Table 2 and the relation drawn in Figure 8 should not be applied to other video observation data.

However, we confirm that we can assume that the perception coefficients for shower meteors are equal to the sporadic ones if we choose the same magnitude range and the same velocity range. We can show that the magnitude distribution compensated by the sporadic ones works well for determining the magnitude ratio of shower meteors. The beginning height of meteors also offers clues to get information about the property of the meteoroids by comparing them with sporadic ones. It is suggested that we can get useful information in this way from any video observation groups.

We established interesting information about 14 major meteor showers, especially for the Perseids and the Geminids.

The magnitude ratio represents the mass distribution in the meteoroid streams, and we can obtain it by video data to compare 14 major showers with each other. We can establish the difference between Perseids and Geminids in the magnitude ratio of the meteoroids, and the changes in the magnitude ratio in function of the solar longitude in the case of the Perseids and the Geminids.

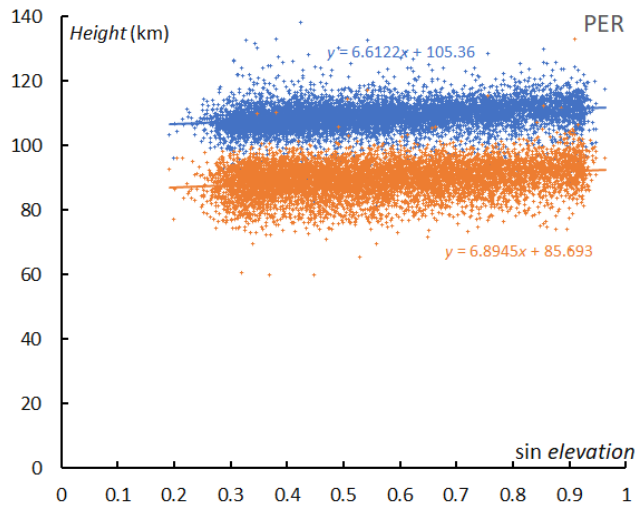


Figure 75 – The beginning height (blue) and ending (orange) of the Perseids in function of the radiant elevation.

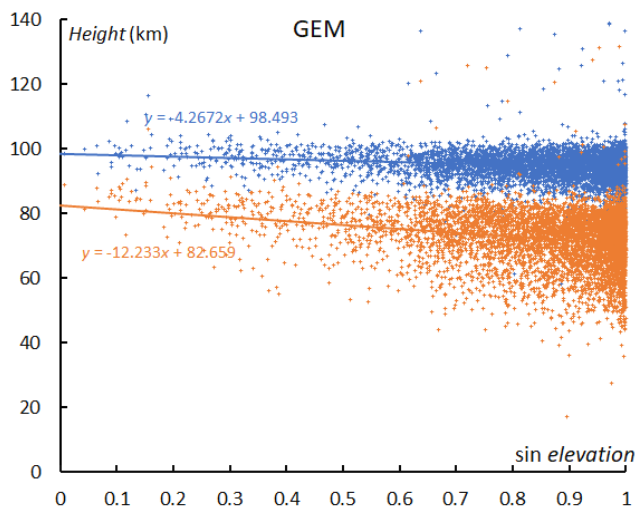


Figure 76 – The beginning height (blue) and ending (orange) of the Geminids in function of the radiant elevation.

The beginning height of meteors is an indicator for the meteoroid's property; a porous meteoroid emits light at a higher altitude than a sporadic one. We can add one more example; the beginning height and the ending height show the singularity of Geminids. Perseid meteors ablate at lower altitudes with a lower radiant elevation angle, but Geminids display an opposite situation (Figures 75 and 76).

The magnitude and the beginning height data obtained from video observations offer very useful clues to investigate the structure of meteoroid streams.

Acknowledgments

We use all published video data by SonotaCo net from 2007 to 2021. The completion of this research owes very much to all the observers who participated in the SonotaCo network.

References

- Ceplecha Z. (1968). “Discrete Levels of Meteor Beginning Height”. *Smithsonian Astrophysical Observatory Special Reports*, No. 279, 54 pages.
- Cook A. F. (1973). “Discrete Levels of Beginning Height of Meteors in Streams”. *Smithsonian Contributions to Astrophysics*, 14, 1–10.
- Koseki M. (2015). “What do we see as ANT, Apex and Toroidal sources? — What meteors are, where meteors came from, where meteoroids are going.”. *WGN, Journal of the IMO*, 43, 127–146.
- Koseki M. (2019). “Profiles of meteor shower activities inferred from the radiant Density Ratios (DR)”. *WGN, Journal of the IMO*, 47, 168–179.
- Koseki M. (2020). “Three components of ‘Taurids’ II”. *WGN, Journal of the IMO*, 48, 36–46.
- Koseki M. (2022). “Global Meteor Network: Outburst produced by dust from 73P/Schwassmann-Wachmann3”. *eMetN*, 7, 369–378.
- Koseki M. (2023). “An Attempt to estimate magnitude ratio using video observations: In the case of eight minor showers listed in 2023 Meteor Shower Calendar of IMO”. *submitted to WGN*.
- SonotaCo (2009). “A meteor shower catalog based on video observations in 2007–2008”. *WGN, Journal of the IMO*, 37, 55–62.
- SonotaCo, Uehara S., Sekiguchi T., Fujiwara Y., Maeda K., and Ueda M. (2021). “J14: A Meteor Shower and Cluster Catalog”. *WGN, Journal of the IMO*, 49, 76–97.

New meteor shower in Draco

Damir Šegon¹, Denis Vida² and Paul Roggemans³

¹ Astronomical Society Istra Pula, Park Monte Zaro 2, 52100 Pula, Croatia

² Department of Physics and Astronomy, University of Western Ontario, London, Ontario, N6A 3K7, Canada
denis.vida@gmail.com

³ Pijnboomstraat 25, 2800 Mechelen, Belgium
paul.roggemans@gmail.com

A new meteor shower on a JFC-type orbit has been detected in 2023 by the Global Meteor Network during the time interval $295.0^\circ < \lambda_\odot < 299.0^\circ$ (January 15–19) from a radiant at R.A. = 235° and Decl. = $+61^\circ$ with a geocentric velocity of 32.8 km/s. This radiant position is east from the known gamma-Ursae Minorids (GUM#0404) meteor shower which has its strongest activity when the new shower activity ends. The new meteor shower has been listed in the Working List of Meteor Showers under the temporary identification M2023-D2.

1 Introduction

The Global Meteor Network radiant map for January 16–17 2023 (*Figure 1*) showed a remarkable concentration at a distinct distance east from the known gamma-Ursae Minorids (GUM#0404). This possible new shower appears earlier in time than the gamma-Ursae Minorids and disappears once GUM reaches more significant activity. This is also visible on the radiant plot obtained by CAMS where a concentration of unidentified radiants appears east from the early GUM-radiants well in advance before the gamma-Ursae Minorids appear as a strong concentration on the map. However, most of the radiants shown on the CAMS map (*Figure 11*) are in fact taken from the Global Meteor Network data and display the same radiants.

2 Meteor shower search methodology

Once a group of meteoroid orbits has been detected on GMN plots, the method used for the determination of the shower parameters consists of the following steps.

At first, radiant positions are being roughly estimated in Sun-centered geocentric ecliptic coordinates $\lambda_g - \lambda_\odot, \beta_g$. Also, the solar longitude range during which the radiant can be seen on plots, as well as a rough radius of radiant dispersion are determined. The radius is usually taken to be a couple of degrees larger than the actual size in order to cover all contributing radiants.

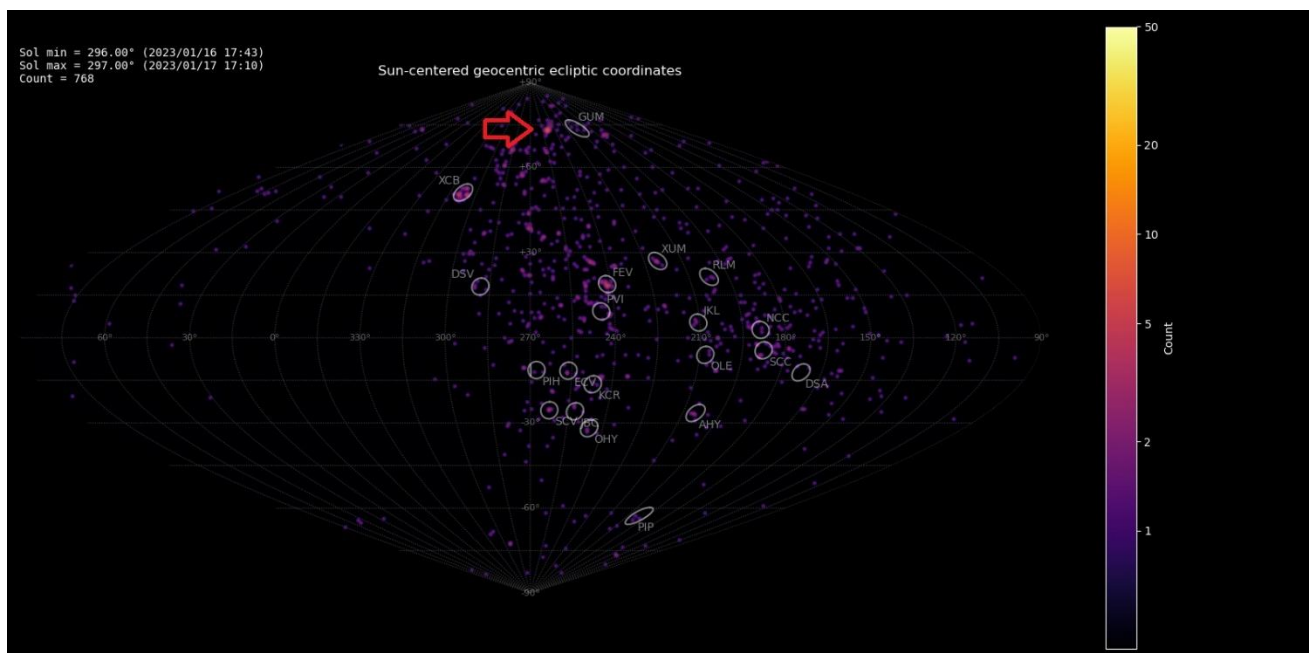


Figure 1 – Radiant plot of the Global Meteor Network data for 2023 January 16–17 in Sun-centered geocentric ecliptic coordinates. The new radiant is visible left of the GUM radiant and is marked by a red arrow.

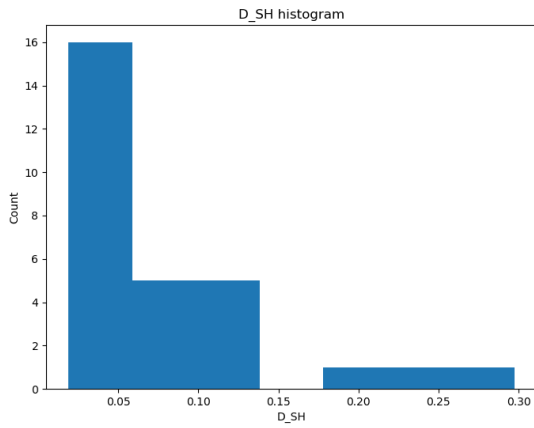


Figure 2 – Histogram of the distribution of the values of the D_{SH} criterion valid for the first mean orbit estimate.

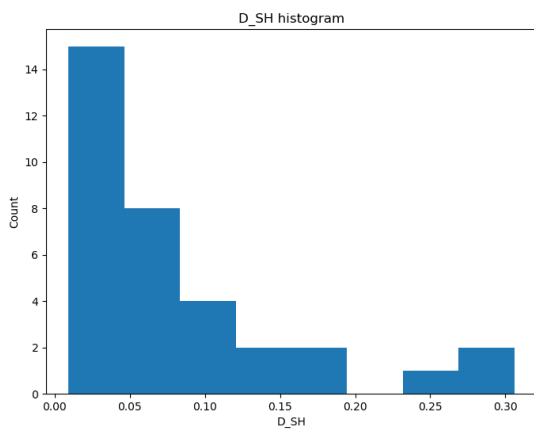


Figure 3 – Histogram of the distribution of values of the D_{SH} criterion valid for the final mean orbit.

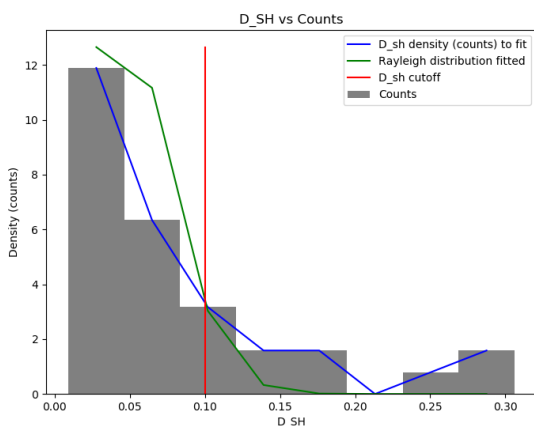


Figure 4 – Rayleigh distribution fit and D_{SH} cutoff.

The numeric average orbit of the radiants that satisfy the criteria is computed and we calculate the Southworth and Hawkins (1963) D -criterion for each selected orbit and the reference mean orbit. The resulting distribution of D -criteria plotted as a histogram (Figure 2) allows us to select the histogram bin containing most meteors. This bin is often not the bin with the smallest D -criterion value, indicating that it follows a Rayleigh distribution.

Next, we recompute the mean orbit using only these core orbits and the updated D -criterion distribution is shown in Figure 3. We then fit a Rayleigh distribution to the computed offsets and choose a D -criterion cutoff value at the 95th percentile (Figure 4). In case the fit fails, we estimate the D -criteria cutoff in a manual way, by picking the smallest D -criteria value covering the left part of the distribution down to local minima count. The Rayleigh distribution may not be the correct choice of the D -criteria distribution for all cases, but the estimated D -criteria cutoff in this case shows that the remaining non-shower orbits are not affected by the extraction from the dataset of new shower ones (see Figure 5). This D -criteria cutoff is then used to isolate only orbits satisfying it, and from this set of orbits the mean orbital parameters and radiant positions are calculated using the method of Jopek et al. (2006). On the radiant and $\Pi-i$ plots, circles represent the part of the radiants we want to emphasize while pale diamonds represent alternative ones, both solar longitude color-coded. Dimensions of circles/diamonds represent the estimated magnitudes (smallest being faintest), while error bars represent a 2-sigma error of the plotted parameter.

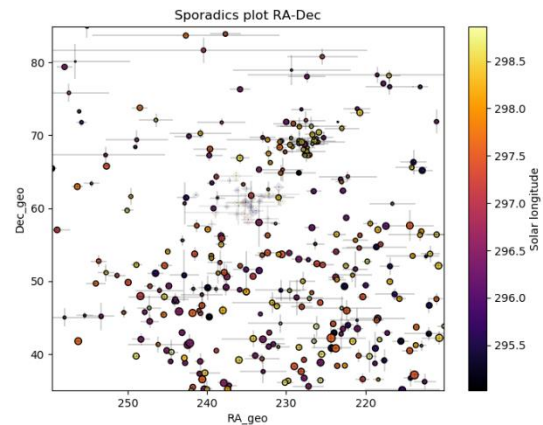


Figure 5 – All radiants in geocentric equatorial coordinates during the shower activity. The gray crosses are the new shower radiants, you can see the GUM radiants in the upper right.

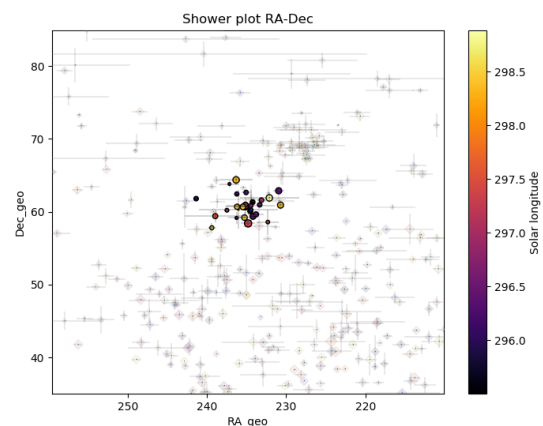


Figure 6 – The reverse of Figure 5, where the background radiants are now grayed out, all radiants in geocentric equatorial coordinates. The GUM shower radiants may be clearly seen as a separate group of orbits at their expected radiant positions (up and right from the new shower).

The shower radiants are compared to the sporadic background in Figures 5 and 6. The concentration of the orbits is also shown in the diagram of the inclination i

against longitude of perihelion Π (Figure 7). The activity period appears within the time interval $295.0^\circ < \lambda_\odot < 299.0^\circ$ (Figure 8).

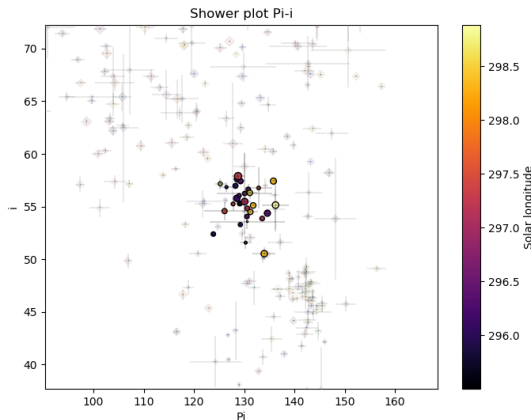


Figure 7 – The diagram of the inclination i against longitude of perihelion Π . The GUM shower radiants may be clearly seen as a separate group of orbits (down and right from the new shower).

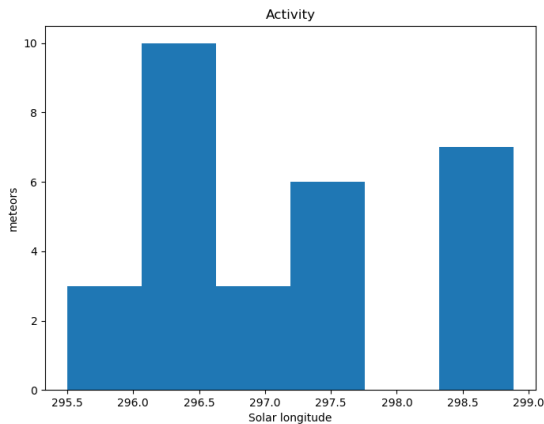


Figure 8 – The activity period with the number of orbits identified as new shower members.

3 New shower or existing shower?

Before making claims that the detected activity qualifies to be listed as a new meteor shower, the known existing meteor showers active around this time from this part of the sky have to be checked. The first suspect candidate is the afore mentioned gamma-Ursae Minorid meteor shower. In equatorial geocentric coordinates, the radiant concentrations appear as close neighbors as well as in Sun-centered ecliptic geocentric coordinates. As the new shower activity appears east and earlier than the bulk of the GUM-activity, the off-set in radiant positions cannot be explained by radiant drift. The Tisserand relative to Jupiter proves both are JFC-type orbits (Table 1). The orbits differ mainly by $\sim 7^\circ$ in inclination and $\sim 12^\circ$ in longitude of perihelion.

Further verification of the IAU MDC Working List of Meteor Showers (Jenniskens et al., 2020; Jopek and Kaňuchová, 2014; 2017; Jopek and Jenniskens, 2011; Neslušan et al., 2020) reveals two more candidate meteoroid streams, about 10 days earlier in time from a radiant position close to that of the possible new meteor

shower, in equatorial as well as in Sun-centered ecliptic coordinates. However, these two showers appear to be an erroneous duplicated entry, listed as the January eta-Draconids (JED#1099) and January iota-Draconids (JID#1107) by Jenniskens (2022). Both orbits have a Tisserand value relative to Jupiter typical for long period comet type orbits with a distinct different eccentricity e compared to the possible new shower. The longitude of perihelion differs by $\sim 15^\circ$. The different nature of this orbit compared to the one of the possible new shower, which has a JFC-type orbit, excludes that JED or JID represent the same meteoroid stream.

Table 1 – Known neighboring showers, gamma-Ursae Minorids (GUM#0404, Shiba, 2022), January eta-Draconids (JED#1099), Jenniskens, 2022), January iota-Draconids (JID#1107), Jenniskens, 2022) and the new meteor shower.

	GUM	JED	JID	New
λ_\odot ($^\circ$)	299.7	287.6	286.9	296.3
λ_{Ob} ($^\circ$)	296.2	–	–	295.5
λ_{Oe} ($^\circ$)	304.9	–	–	298.9
a_g ($^\circ$)	229.0	237.3	236.3	235.2
δ_g ($^\circ$)	+67.7	+62.6	+62.3	+60.7
Δa_g ($^\circ$)	0.99	–	–	–
$\Delta \delta_g$ ($^\circ$)	–0.70	–	–	–
v_g (km/s)	29.4	37.3	37.3	32.8
λ ($^\circ$)	157.1	180.5	180.6	184.2
$\lambda_g - \lambda_\odot$ ($^\circ$)	217.4	252.9	253.7	247.1
β_g ($^\circ$)	+74.3	+75.6	+75.1	+73.7
a (A.U.)	2.79	25.6	19.4	2.73
q (A.U.)	0.952	0.979	0.979	0.973
e	0.659	0.962	0.950	0.644
i ($^\circ$)	48.0	59.5	59.6	55.3
ω ($^\circ$)	203.1	187.4	187.7	193.1
Ω ($^\circ$)	299.7	287.5	286.9	297.1
Π ($^\circ$)	142.8	114.9	114.6	130.2
T_j	2.60	0.82	0.88	2.54
N	60	28	21	29

4 Another search method

Another method has been applied to check this new meteor shower discovery. The starting point here can be any visually spotted concentration of radiant points or any other indication for the occurrence of similar orbits. The method has been described before (Roggemans et al., 2019). The main difference with the method described in Section 2 is that three different discrimination criteria are combined in order to have only those orbits which fit different criteria. Instead of using a cutoff value for the D-criteria these values are considered in different classes with different thresholds of similarity. Depending on the dispersion and the type of orbits, the most appropriate threshold of similarity is selected to locate the best fitting mean orbit as a result of an iterative procedure.

Applying this search method, the same orbits are found as with the higher described method. *Figure 9* shows the radiant in Sun-centered geocentric ecliptic coordinates with the sporadic background (black), the gamma-Ursae Minorids (blue) and two similarity classes for the new shower (yellow and red). The average radiant of the new shower is east of that of the gamma-Ursae Minorid radiants.

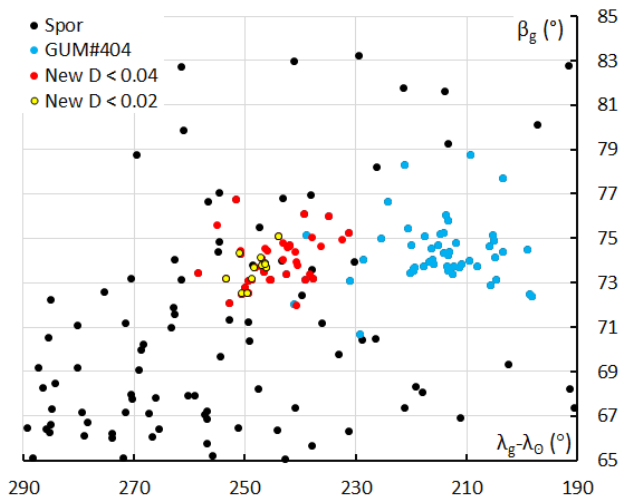


Figure 9 – Close up of the Sun-centered ecliptic geocentric coordinates for the possible new shower and the orbits identified as gamma-Ursae Minorids.

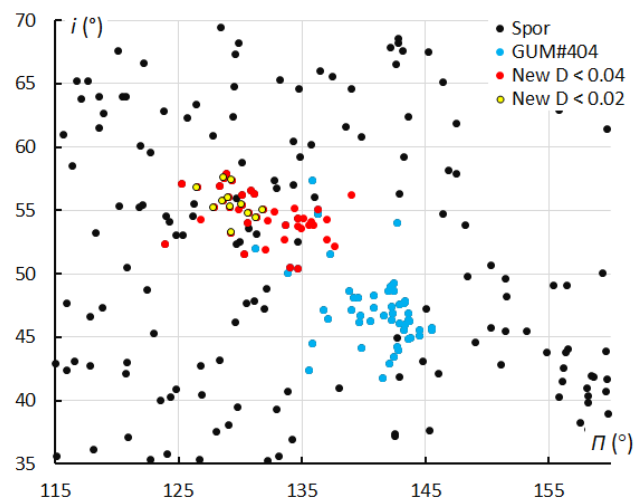


Figure 10 – Diagram of the inclination i against the longitude of perihelion Π for the new shower and the gamma-Ursae Minorids.

The offset in the concentration of orbits is also very obvious in the diagram showing the inclination i against the longitude of perihelion Π (*Figure 10*). The 12 best fitting orbits within the interval $295.0^\circ < \lambda_0 < 299.0^\circ$, according to this method yield a mean orbit which is in perfect agreement with the results presented in *Table 1*.

- $a = 2.75$ AU
- $q = 0.974$ AU
- $e = 0.6465$
- $i = 55.6^\circ$
- $\Omega = 296.80^\circ$

- $\omega = 192.52^\circ$

5 Comparing older data and other datasets

Looking up past years orbit data for Global Meteor Network, we find only 16 similar orbits with $D_{SH} < 0.1$ and $D_D < 0.04$ for the period 2019 to 2022. Checking the CAMS data for 2011–2016 we also find 16 similar orbits with $D_{SH} < 0.1$ and $D_D < 0.04$. The SonotaCo data for 2007–2021 yield 12 orbits with $D_{SH} < 0.1$ and $D_D < 0.04$. And EDMOND data for 2006–2016 had only 6 similar orbits with $D_{SH} < 0.1$ and $D_D < 0.04$. 2023 appears to be the first year with noticeable activity for this new shower.

As mentioned in the introduction, the new shower appears also as a group of unidentified radiants on the CAMS map for January 16–17 (*Figure 11*). However, this data consists mainly of GMN data and it is not possible to select only CAMS data in this display.

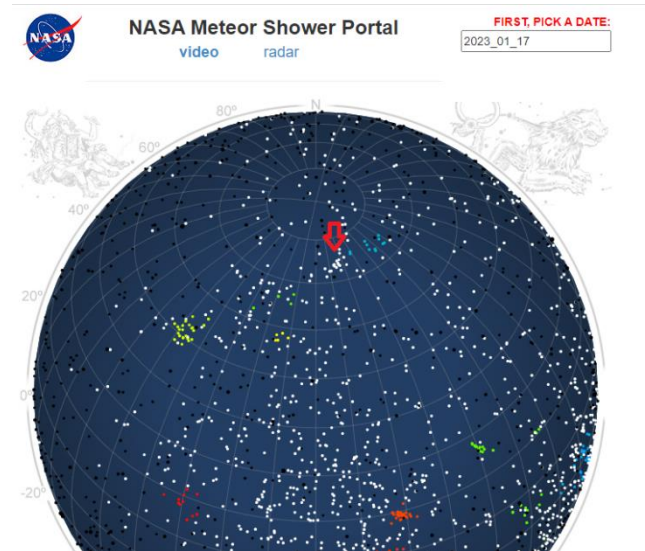


Figure 11 – Radiant plot for CAMS on 2023 January 17. The radiant concentration is indicated with a red arrow.

6 Conclusion

A new meteor shower radiant has been discovered in Global Meteor Network data around 2023 January 16–17 with a radiant close but still distinct from the known gamma-Ursae Minorids. A mean orbit could be established based on 29 orbits. The new shower and the GUM orbits being of the same type and relatively close apart in space, may be somehow related and belong to a small complex of common origin.

The new meteor shower has been reported to the IAU and has been listed in the Working List of Meteor Showers² under the temporary identification M2023-D2.

² https://www.ta3.sk/IAUC22DB/MDC2022/Roje/pojedynczy_obiekt.php?porz=01595&kodstrumienia=01215

Acknowledgment

The authors thank all people who support the Global Meteor Network by contributing meteor camera data or in any other way to help monitoring meteor activity around the clock worldwide. The Global Meteor Network results were obtained thanks to the efforts of the following volunteers: *Richard Abraham, Victor Acciari, Rob Agar, Jonathan Alexis Valdez Aguilar, Salvador Aguirre, Yohsuke Akamatsu, David Akerman, Daknam Al-Ahmadi, Jamie Allen, Edison José Felipe Pérezgómez Álvarez, Alexandre Alves, Don Anderson, Željko Andreić, Martyn Andrews, Miguel Diaz Angel, Enrique Arce, Georges Attard, David Attreed, Chris Baddiley, David Bailey, Erwin van Ballegoij, Roger Banks, Hamish Barker, Jean-Philippe Barrilliot, Alejandro Barriuso, Amy Barron, Ricky Bassom, Richard Bassom, Creina Beaman, Alan Beech, Dennis Behan, Ehud Behar, Josip Belas, Alex Bell, Florent Benoit, Denis Bergeron, Serge Bergeron, Jorge Augusto Acosta Bermúdez, Steve Berry, Adrian Bigland, Frantisek Bilek, Jim Blackhurst, Chris Blake, Thomas Blog, Arie Blumenzweig, Ventsislav Bodakov, Claude Boivin, Robin Boivin, Bruno Boniconro, Mia Boothroyd, Ludger Börgerding, Fabricio Borges, Ubiratan Borges, Steve Bosley, Dorian Božičević, David Brash, Mike Breimann, Stuart Brett, Ed Breuer, Martin Breukers, John W. Briggs, Gareth Brown, Peter G. Brown, Nial Bruce, Laurent Brunetto, Nigel Bubb, Tim Burgess, Jason Burns, Jon Bursey, Yong-Ik Byun, Sylvain Cadieux, Dino Čaljkusić, Peter Campbell-Burns, Andrew Campbell-Laing, Pablo Canedo, Sepe Canonaco, Jose Carballada, Rolf Carstens, Steve Carter, David Castledine, Gilton Cavallini, Andrew Challis, Brian Chapman, Jason Charles, Jim Cheetham, Zhuoyang Chen, Matt Cheselka, Ivica Ćiković, Tim Claydon, Trevor Clifton, Fiona Cole, Manel Colldecarrera, Michael Cook, Bill Cooke, Simon Cooke-Willis, Christopher Coomber, Brendan Cooney, Edward Cooper, Jamie Cooper, Andrew Cooper, Tim Cooper, Bernard Côté, Paul Cox, Jim Critchley, Richard Croy, Llewellyn Cupido, Christopher Curtis, Chris Dakin, Fernando Dall'igna, James Davenport, Peter Davis, Richard Davis, Pedro Augusto Hay Day, Steve Dearden, Christophe Demeautis, Bart Dessoy, Pat Devine, Paul Dickinson, Ivo Dijan, Tammo Jan Dijkema, Pieter Dijkema, Luciano Miguel Diniz, Marcelo Domingues, Jürgen Dörr, Lucia Dowling, Stacey Downton, Stewart Doyle, Zoran Dragić, Iain Drea, John Drummond, Daniel Duarte, Igor Duchaj, Jean-Paul Dumoulin, Garry Dymond, Jonathan Eames, Robin Earl, Howard Edin, Raoul van Eijndhoven, Ollie Eisman, Carl Elkins, Peter Eschman, Bob Evans, Nigel Evans, Bev M. Ewen-Smith, Mark Fairfax, James Farrar, Seraphin Feller, Andres Fernandez, Louw Ferreira, Andrew Fiamingo, Barry Findley, Rick Fischer, Richard Fleet, Murray Forbes, Jim Fordice, Ange Fox, Kyle Francis, Patrick Franks, Ryan Frazer, Stefan Frei, Gustav Frisholm, Pierre Gamache, José María García, Enrique Chávez Garcilazo, Ivan Gašparić, Mark Gatehouse, Chris George, Megan Gialluca, Kevin Gibbs-Wragge, Marc Corretgé Gilart, Lachlan Gilbert, Jim Gilbert, Jason Gill, Philip Gladstone, Uwe Glässner, Roel Gloudemans, Tim Gloudemans, Chuck*

Goldsmith, Hugo González, Brenda Goodwill, Nikola Gotovac, Ian Enting Graham, Neil Graham, Colin Graham, Pete Graham, Phillip Wilhelm Maximilian Grammerstorf, Sam Green, Bob Greschke, Stephen Grimes, Daniel J. Grinkevich, Larry Groom, Dominique Guiot, Tioga Gulon, Margareta Gumilar, Peter Gural, Nikolay Gusev, Kees Habraken, Bernard Hagen, Alex Haislip, John Hale, Peter Hallett, Graeme Hanigan, Erwin Harkink, Ed Harman, Marián Harnádek, Ryan Harper, David Hatton, Jason van Hattum, Tim Havens, Mark Haworth, Paul Haworth, Richard Hayler, Andrew Heath, Paul Heelis, Sam Hemmelgarn, Igor Henrique, Rick Hewett, Lee Hill, Nicholas Hill, Don Hladiuk, Alex Hodge, Simon Holbeche, Jeff Holmes, Lisa Holstein, Steve Homer, Anthony Hopkinson, Nick Howarth, Matthew Howarth, Jeff Huddle, Gordon Hudson, Bob Hufnagel, Roslina Hussain, Mike Hutchings, Jan Hykel, Roland Idaczyk, Anatoly Ijon, Russell Jackson, Jean-Marie Jacquart, Jost Jahn, Tihomir Jakopčić, Nick James, Chris James, Rick James, Phil James, Ken Jamrogowicz, Ilya Jankowsky, Peter Jaquierey, Alex Jeffery, Klaas Jobse, Richard Johnston, Kath Johnston, Dave Jones, Fernando Jordan, Romulo Jose, Vladimir Jovanović, Ron James Jr, Alfredo Dal' Ava Júnior, Jocimar Justino, Javor Kac, Richard Kacerek, Milan Kalina, Jonathon Kambulow, Steve Kaufman, Scott Kaufmann, Paul Kavanagh, Ioannis Kedros, Peter Kent, Jürgen Ketterer, Alex Kichev, Harri Kuisinen, Jean-Baptiste Kikwaya, Sebastian Klier, Dan Klinglesmith, John Kmetz, Zoran Knez, Danko Kočič, Korado Korlević, Stanislav Korotkiy, Bela Szomi Kralj, Josip Krpan, Zbigniew Krzeminski, Reinhard Kühn, Patrik Kukić, Remi Lacasse, Gaétan Laflamme, Steve Lamb, Hervé Lamy, Stuart Land, Jean Francois Larouche, Ian Lauwerys, Peter Lee, Hartmut Leiting, Damien Lema, Guy Létourneau, David Leurquin, Gareth Lloyd, Rob de Corday Long, Robert Longbottom, Jose Galindo Lopez, Eric Lopez, Paul Ludick, José Martin Luis, Pete Lynch, Frank Lyter, Anton Macan, Jonathan Mackey, John Maclean, Igor Macuka, Nawaz Mahomed, Simon Maidment, Mirjana Malarić, Nedeljko Mandić, Alain Marin, Bob Marshall, Colin Marshall, Gavin Martin, Andrei Marukhno, Keith Maslin, Nicola Masseroni, Bob Massey, Jacques Masson, Damir Matković, Filip Matković, Dougal Matthews, Alan Maunder, Michael Mazur, Sergio Mazzi, Stuart McAndrew, Lorna McCalman, Alex McConahay, Mason McCormack, Charlie McCormack, Robert McCoy, Jamie McCulloch, Vincent McDermott, Tommy McEwan, Mark McIntyre, Peter McKellar, Simon McMillan, Damien McNamara, Peter Meadows, Edgar Mendes Merizio, Aleksandar Merlak, Horst Meyerderks, Filip Mezak, Pierre-Michael Micaletti, Greg Michael, Matej Mihelčić, Simon Minnican, Wullie Mitchell, Georgi Momchilov, Dean Moore, Edson Valencia Morales, Lubomir Moravek, Nelson Moreira, Kevin Morgan, Roger Morin, Nick Moskovitz, Daniela Cardozo Mourão, Dave Mowbray, Andrew Moyle, Gene Mroz, Muhammad Luqmanul Hakim Muharam, Adam Mullins, Juan Luis Muñoz, Brian Murphy, Carl Mustoe, Przemek Nagański, Jean-Louis Naudin, Damjan Nemarnik, Attila Nemes, Dave Newbury, Colin Nichols, Tommy B. Nielsen, Nick Norman, Philip Norton, Zoran Novak, Gareth

Oakey, Washington Oliveira, Jorge Oliveira, Angélica López Olmos, Jamie Olver, Christine Ord, Nigel Owen, Michael O’Connell, Dylan O’Donnell, Thiago Paes, Carl Panter, Neil Papworth, Filip Parag, Gary Parker, Ian Parker, Simon Parsons, Ian Pass, Lovro Pavletić, Igor Pavletić, Richard Payne, Pierre-Yves Pechart, Holger Pedersen, Eduardo Fernandez Del Peloso, William Perkin, Heather Petelo, Enrico Pettarin, Alan Pevec, Mark Phillips, Alan Pickwick, Anthony Pitt, Patrick Poitevin, Tim Polfliet, Renato Poltronieri, Pierre de Ponthière, Callum Potter, Derek Poulton, Janusz Powazki, Aled Powell, Alex Pratt, Miguel Preciado, David Price, Nick Primavesi, Paul Prouse, Paul Pugh, Chuck Pullen, Terry Pundiak, Anzhari Purnomo, Lev Pustil’Nik, Dan Pye, Nick Quinn, Chris Ramsay, David Rankin, Steve Rau, Mike Read, Dustin Rego, Chris Reichelt, Danijel Reponj, Fernando Requena, Maciej Reszelsk, Jessica Richards, Ewan Richardson, Terry Richardson, Martin Richmond-Hardy, Mark Robbins, Martin Robinson, David Robinson, Heriton Rocha, Paul Roche, Herve Roche, Paul Roggemans, Adriana Roggemans, Alex Roig, David Rollinson, Marthinus Roos, Andre Rousseau, Brian Rowe, Jim Rowe, Nicholas Ruffier, Nick Russel, Janis Russell, Dmitrii Rychkov, Robert Saint-Jean, Michel Saint-Laurent, Jason Sanders, Clive Sanders, Ivan Sardelić, Simon Saunders, Rob Saunders, John Savage, Lawrence Saville, Vasilii Savtchenko, Philippe Schaak, William Schauff, Ansgar Schmidt, Thomas Schmiereck, James Scott, Geoff Scott, Yfore Scott, Jim Seargeant, Damir Šegon, Marko Šegon, Jay Shaffer, Steven Shanks, Mike Shaw, Jamie Shepherd, Angel Sierra, Ivo Silvestri, François Simard, Terry Simmich, Noah Simmonds, Murray Singleton, Nikos Sioulas, Ivica Skokić, Zané Smit, Ian A. Smith, Dave Smith, Ned Smith, Tracey Snelus, Germano Soru, Warley Souza, Mark Spink, Denis St-Gelais, James Stanley, Radim Stano, Laurie Stanton, Robert D. Steele, Yuri Stepanychev, Graham Stevens, Thomas Stevenson, Richard Stevenson, Peter Stewart, William Stewart, Paul Stewart, Con Stoitsis, Andrea Storani, Andy Stott, David Strawford, Mark Suhovecky, Claude Surprenant, Rajko Sušan, Ciaran Tangney, René Tardif, Jeremy Taylor, David Taylor, Yakov Tchenak, Jacqui Thompson, Murray Thompson, John Thurmond, Steven Tilley, Stanislav Tkachenko, Christopher Tofts, Steve Tonkin, Sarah Tonorio, Eric Toops, Torcuill Torrance, Peter Triffitt, Steve Trone, Wenceslao Trujillo, John Tuckett, Sofia Ulrich, Myron Valenta, Jean Vallieres, Paraksh Vankawala, Neville Vann, Robert Veronneau, Marco Verstraaten, Arie Verveer, Jochen Vollsted, Predrag Vukovic, Aden Walker, Martin Walker, Bill Wallace, John Waller, Jacques Walliang, Didier Walliang, Christian Wanlin, Tom Warner, Andrew Washington, Neil Waters, Steve Welch, Tobias Westphal, Tosh White, Jonathan Whiting, Alexander Wiedekind-Klein, John Wildridge, Ian Williams, Mark Williams, Guy Williamson, Graham Winstanley, Urs Wirthmueller, Jan Wisniewski, Bill Witte, Jeff Wood, Martin Woodward, Jonathan Wyatt, Anton Yanishevskiy, Penko Yordanov, Justin Zani, Stephane Zaroni, Bob Zarnke, Christof Zink, Pető Zsolt, Dario Zubović, Marcelo Zurita, Asociación de Astronomía de

Marina Alta, Costa Blanca Astronomical Society, Perth Observatory Volunteer Group, Royal Astronomical Society of Canada Calgary Centre (list established 2 May 2023).

References

- Drummond J. D. (1981). “A test of comet and meteor shower associations”. *Icarus*, **45**, 545–553.
- Jenniskens P., Jopek T. J., Janches D., Hajduková M., Kokhirova G. I., Rudawska R. (2020). “On removing showers from the IAU Working List of Meteor Showers”. *Planetary and Space Science*, **182**, article id. 104821.
- Jenniskens P. (2022). Submitted.
- Jopek T. J., Rudawska R. and Pretka-Ziomek H. (2006). “Calculation of the mean orbit of a meteoroid stream”. *Monthly Notices of the Royal Astronomical Society*, **371**, 1367–1372.
- Jopek T. J., Jenniskens P. M. (2011). “The Working Group on Meteor Showers Nomenclature: A History, Current Status and a Call for Contributions”. In, W.J. Cooke, D.E. Moser, B.F. Hardin, and D. Janches, editors, *Meteoroids: The Smallest Solar System Bodies, Proceedings of the Meteoroids Conference held in Breckenridge, Colorado, USA, May 24-28, 2010*. NASA/CP-2011-216469, pages 7–13.
- Jopek T. J., Kaňuchová Z. (2014). “Current status of the~IAU MDC Meteor Showers Database”. In, T.J. Jopek, F.J.M. Rietmeijer, J. Watanabe, I.P. Williams, editors, *Meteoroids 2013 Proceedings of the Astronomical Conference held at A.M. University, Poznan, Poland, Aug. 26-30, 2013*, A.M. University Press, pages 353–364.
- Jopek T. J., Kaňuchová Z. (2017). “IAU Meteor Data Center-the shower database: A status report”. *Planetary and Space Science*, **143**, 3–6.
- Neslušan L., Poručan V., Svoreň J., Jakubík M. (2020). “On the new design othe IAU MDC portal”. *WGN, Journal of the International Meteor Organization*, **48**, 168–169.
- Roggemans P., Johannink C. and Campbell-Burns P. (2019a). “October Ursae Majorids (OCU#333)”. *eMetN*, **4**, 55–64.
- Shiba Y. (2022). “Jupiter Family Meteor Showers by SonotaCo Network Observations”. *WGN, Journal of the International Meteor Organization*, **50**, 38–61.
- Southworth R. B. and Hawkins G. S. (1963). “Statistics of meteor streams”. *Smithsonian Contributions to Astrophysics*, **7**, 261–285.

New meteor shower in Bootes

Damir Šegon¹, Denis Vida² and Paul Roggemans³

¹ Astronomical Society Istra Pula, Park Monte Zaro 2, 52100 Pula, Croatia

² Department of Earth Sciences, University of Western Ontario, London, Ontario, N6A 5B7, Canada
denis.vida@gmail.com

³ Pijnboomstraat 25, 2800 Mechelen, Belgium
paul.roggemans@gmail.com

A new meteor shower on a LPC-type orbit has been detected in 2022 by the Global Meteor Network during the time interval $282.41^\circ < \lambda_o < 282.83^\circ$ (2022, January 2–3) from a radiant at R.A. = 219° and Decl. = $+28^\circ$ with a geocentric velocity of 58.9 km/s. The new meteor shower has been listed in the Working List of Meteor Showers under the temporary identification M2023-D1.

1 Introduction

Verification of older radiant plots of the Global Meteor Network revealed a radiant concentration south of the Quadrantid radiant, active for as little as 10 hours during the night of 2–3 January 2022 (Figure 1).

2 Meteor shower search methodology

The method has been described in Šegon et al. (2023), but for this specific case we choose not to use the Southworth and Hawkins (1963) D -criterion, but the criterion defined by Valsecci et al. (1999). The idea to use another discrimination criterion is to show that this method works regardless the kind of criterion which is applied. The resulting distribution of D -criteria plotted as a histogram (Figure 2) allows us to select the histogram bin containing most meteors.

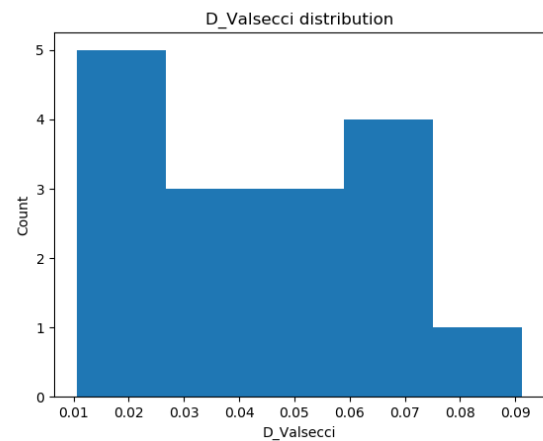


Figure 2 – Histogram of the distribution of the values of the D_V criterion valid for the first mean orbit estimate.

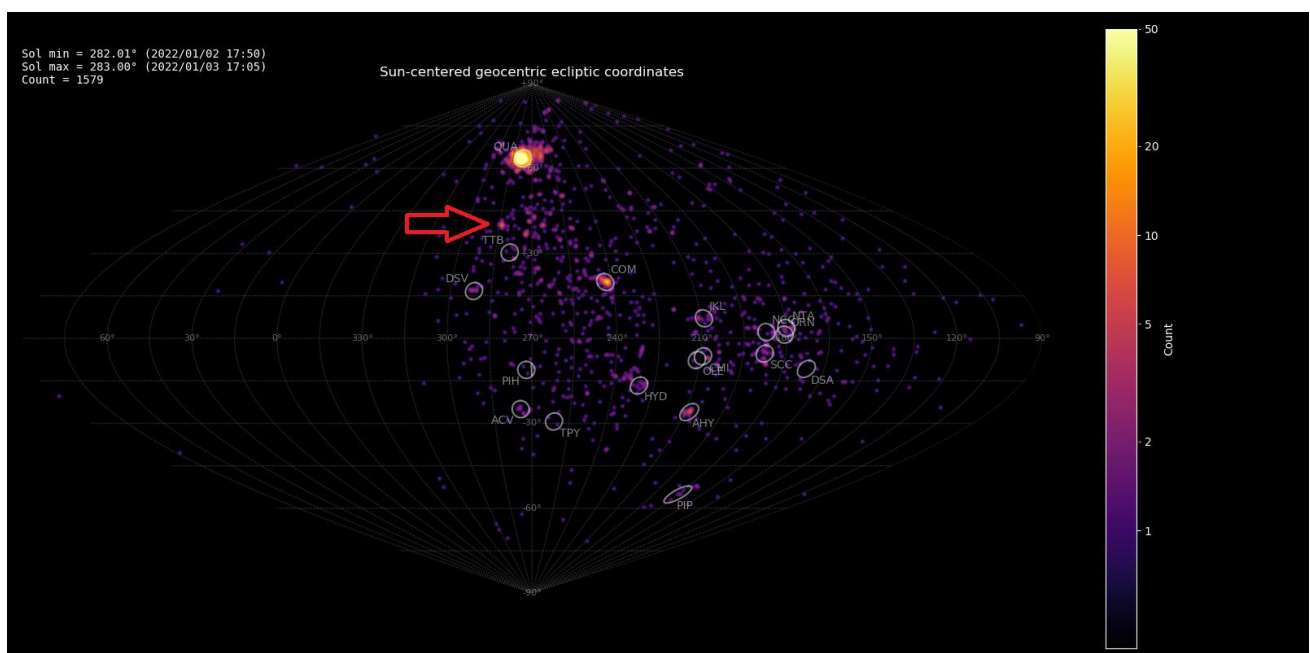


Figure 1 – Radiant plot of the Global Meteor Network data for 2022 January 2–3 in Sun-centered geocentric ecliptic coordinates. The new radiant is visible south of the QUA radiant and is marked by a red arrow.

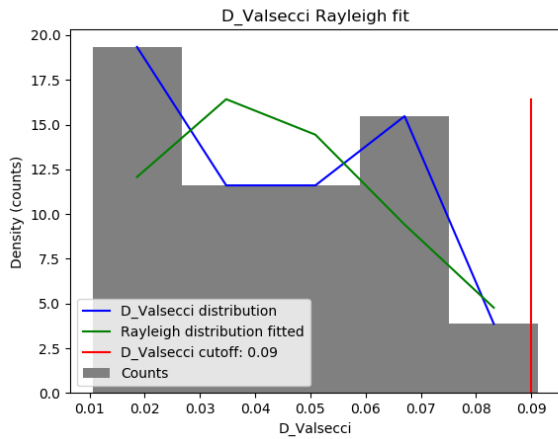


Figure 3 – Rayleigh distribution fit and D_V cutoff.

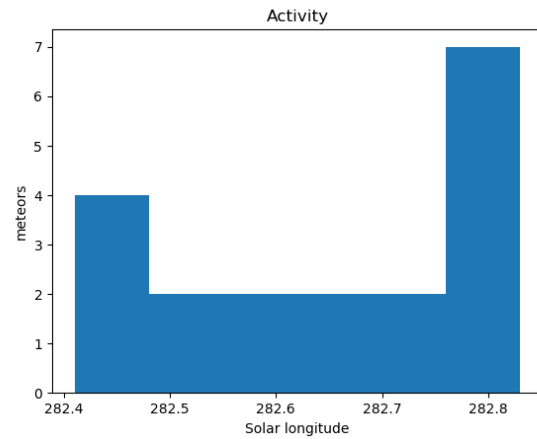


Figure 6 – The activity period with the number of orbits identified as new shower members.

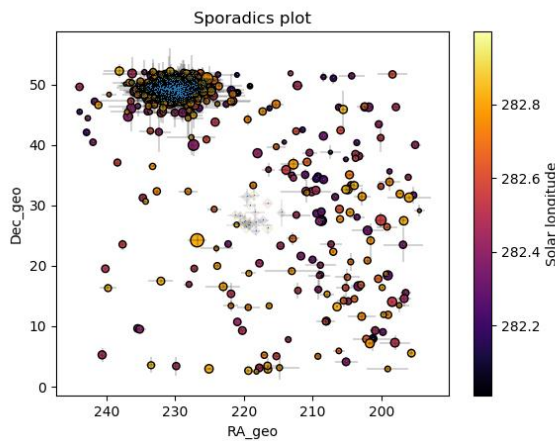


Figure 4 – All radiants in geocentric equatorial coordinates during the shower activity. The gray crosses are the new shower radiants, you can see the QUA radiants in the upper left.

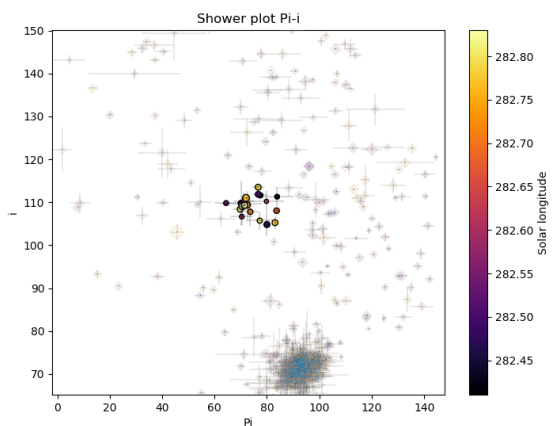


Figure 7 – The diagram of the inclination i against longitude of perihelion Π . The QUA shower radiants may be clearly seen as a separate group of orbits (down and right from the new shower).

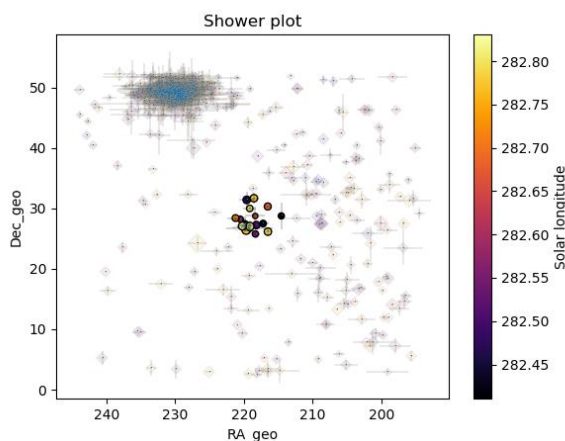


Figure 5 – The reverse of Figure 4 where the background radiants are now grayed out, all radiants in geocentric equatorial coordinates. The QUA shower radiants may be clearly seen as a separate group of orbits at their expected radiant positions (up and left from the new shower).

The Rayleigh distribution fit results in $D_V = 0.09$. The resulting mean orbit calculated with the method of Jopek et al. (2006) is listed in Table 1. The radiant plot in equatorial coordinates is shown in Figures 4 and 5. The activity period appears to be very short, about 10 hours within the interval $282.41^\circ < \lambda_\theta < 282.83^\circ$ (Figure 6).

3 New shower or existing shower?

Verification of the IAU MDC Working List of Meteor Showers (Jenniskens et al., 2020; Jopek and Kaňuchová, 2014; 2017; Jopek and Jenniskens, 2011; Neslušan et al., 2020) reveals two meteoroid streams with the same type of orbits. One shower is active the same date, the other one more than 10 days later in time with slightly different radiant positions, in equatorial and in Sun-centered ecliptic coordinates.

Both the Southworth and Hawkins as well as the Drummond D -criteria exceed the upper limits to suggest any similarity. All three orbits in Table 1 are Long Period-type comet (LPC) retrograde orbits, but differ mainly in longitude of perihelion. Nevertheless, the occurrence within a period of weeks with radiants not too far apart may suggest some common origin for these same orbit type meteoroid streams. The ten-hour duration activity observed in 2022 could not be associated with any existing shower and therefore has been suggested as a new meteor shower.

Table 1 – Known neighboring showers, Canum Venaticids-Bootids (TCV#0579) and Serpentids-Coronae Borealis (RSE#0594), both (Gural et al., 2014) and the new meteor shower.

	TCV	RSE	New
λ_o (°)	282	298	282.66
λ_{ob} (°)	275	293	282.4
λ_{oe} (°)	288	303	282.85
α_g (°)	210.1	234.9	218.8
δ_g (°)	+29.4	+25.1	+28.2
$\Delta\alpha_g$ (°)	0.69	0.71	–
$\Delta\delta_g$ (°)	–0.17	–0.20	–
v_g (km/s)	59.9	56.6	58.9
λ (°)	195.3	224.5	204.9
$\lambda_g - \lambda_o$ (°)	273.3	286.5	282.2
β_g (°)	+38.6	+43.2	+40.8
a (A.U.)	7.0	10.9	14.9
q (A.U.)	0.977	0.902	0.9296
e	0.861	0.917	0.9375
i (°)	113.7	103.7	109.1
ω (°)	171.6	145.9	153.1
Ω (°)	281.8	298.4	282.7
Π (°)	93.4	84.3	75.7
T_j	0.27	0.21	–0.04
N	21	17	18

4 Another search method

Another method has been applied to search for this new meteor shower combining three different discrimination criteria (Roggemans et al., 2019).

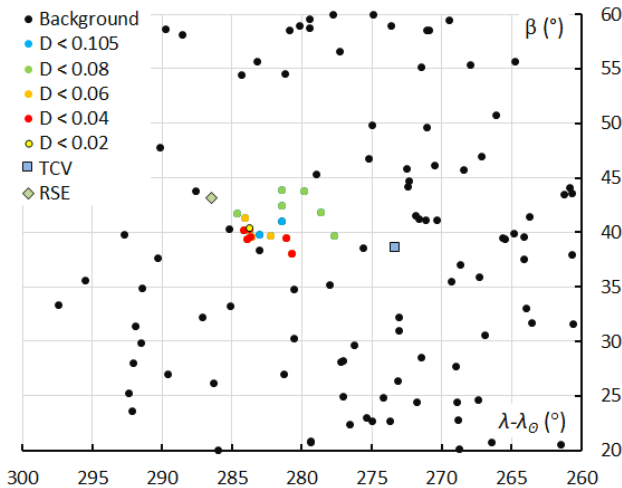


Figure 8 – Close up of the Sun-centered ecliptic geocentric coordinates for the possible new shower and the two known showers TCV and RSE.

This stream search detects 18 similar orbits in the 2022 data but with a large dispersion. Only 6 of these orbits fit with $D_{SH} < 0.1$ and $D_D < 0.04$. The large spread is very well visible in the Sun-centered ecliptic coordinates (Figure 8). The positions of the Canum Venaticids-Bootids

(TCV#0579) and Serpentids-Coronae Borealis (RSE#0594) are also marked in this plot to show the offset relative to the radiants of the new shower. The diagram of inclination i against the longitude of perihelion Π (Figure 9) shows the large dispersion in longitude of perihelion.

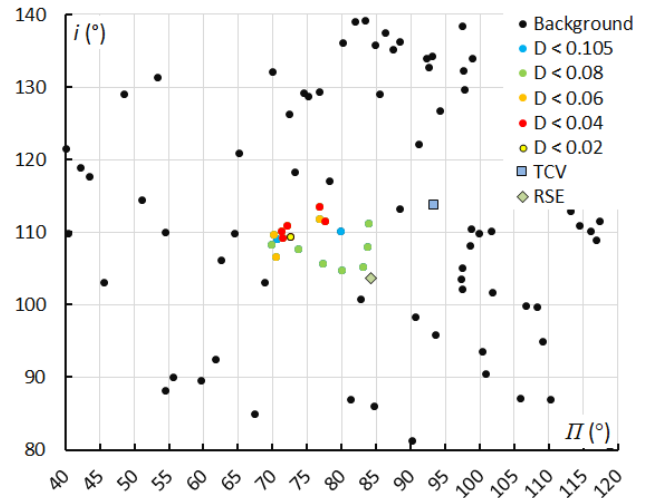


Figure 9 – Diagram of the inclination i against the longitude of perihelion Π for the new shower and the two known showers TCV and RSE.

The 6 best fitting orbits within the interval $282.43^\circ < \lambda_o < 282.85^\circ$, according to this method yield a mean orbit which is in good agreement with the results presented in Table 1.

- $a = 17.9$ AU
- $q = 0.926$ AU
- $e = 0.948$
- $i = 110.9^\circ$
- $\Omega = 283.1^\circ$
- $\omega = 151.9^\circ$
- $\Pi = 75.0$
- $T_j = -0.12$

5 Comparing older data and other datasets

Looking up past years orbit data for Global Meteor Network, we find only 4 similar orbits with $D_{SH} < 0.1$ and $D_D < 0.04$ for 2023. Checking the CAMS data for 2011–2016 we find 13 similar orbits with $D_{SH} < 0.1$ and $D_D < 0.04$, one or few each year, spread in time. The SonotaCo data for 2007–2022 yield 4 orbits with $D_{SH} < 0.1$ and $D_D < 0.04$, only one for 2022 at $\lambda_o = 284.0^\circ$ but nothing during the activity interval according to GMN although SonotaCo had 47 orbits collected in 2022 during this interval. And EDMOND data for 2006–2016 had only 4 similar orbits with $D_{SH} < 0.1$ and $D_D < 0.04$.

The new shower appears also as a group of unidentified radiants on the CAMS map for 2022, January 2–3 (Figure 10). However, this data includes GMN data and it is not possible to select only CAMS data in this display. As

CAMS data has not been released publicly since 2016, no comparison is possible.

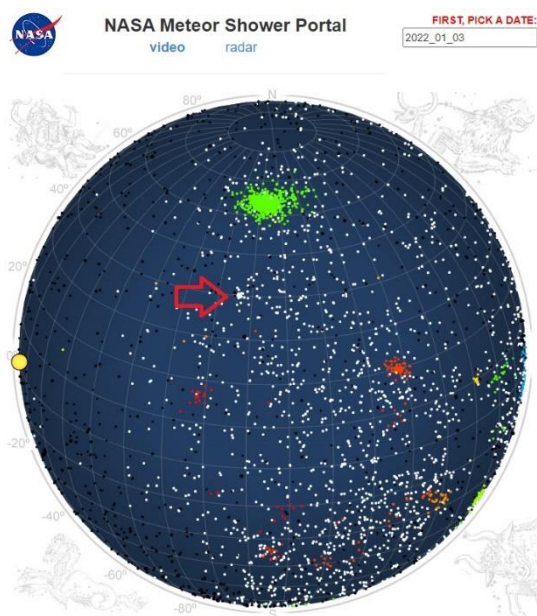


Figure 10 – Radiant plot for CAMS on 2022 January 3. The radiant concentration is indicated with a red arrow.

6 Conclusion

A new meteor shower radiant has been discovered in Global Meteor Network data around 2022 January 2–3 at R.A. = 218.7° and Decl. = +28.0°. A mean orbit could be established based on 19 orbits. The new shower may be related to two nearby meteoroid streams, Canum Venaticids-Bootids (TCV#0579) and Serpentids-Coronae Borealis (RSE#0594) which have the same type of orbit.

The new meteor shower has been reported to the IAU and has been listed in the Working List of Meteor Showers³ under the temporary identification M2023-D1.

Acknowledgment

The authors thank all people who support the Global Meteor Network by contributing meteor camera data or in any other way to help monitoring meteor activity around the clock worldwide. For the list of GMN contributors we refer to Šegon et al. (2023).

References

- Drummond J. D. (1981). “A test of comet and meteor shower associations”. *Icarus*, **45**, 545–553.
- Gural P., Šegon D., Andreić Ž., Skokić I., Korlević K., Vida D., Novoselnik F., Gostinski D. (2014). “Results of CMN 2013 search for new showers across CMN and SonotaCo databases II”. *WGN, Journal of the International Meteor Organization*, **42**, 132–138.
- Jenniskens P., Jopek T. J., Janches D., Hajduková M., Kokhirova G. I., Rudawska R. (2020). “On

removing showers from the IAU Working List of Meteor Showers”. *Planetary and Space Science*, **182**, article id. 104821.

- Jopek T. J., Rudawska R. and Pretka-Ziomek H. (2006). “Calculation of the mean orbit of a meteoroid stream”. *Monthly Notices of the Royal Astronomical Society*, **371**, 1367–1372.
- Jopek T. J., Jenniskens P. M. (2011). “The Working Group on Meteor Showers Nomenclature: A History, Current Status and a Call for Contributions”. In, W.J. Cooke, D.E. Moser, B.F. Hardin, and D. Janches, editors, *Meteoroids: The Smallest Solar System Bodies, Proceedings of the Meteoroids Conference held in Breckenridge, Colorado, USA, May 24-28, 2010*. NASA/CP-2011-216469, pages 7–13.
- Jopek T. J., Kaňuchová Z. (2014). “Current status of the IAU MDC Meteor Showers Database”. In, T.J. Jopek, F.J.M. Rietmeijer, J. Watanabe, I.P. Williams, editors, *Meteoroids 2013 Proceedings of the Astronomical Conference held at A.M. University, Poznan, Poland, Aug. 26-30, 2013*, A.M. University Press, pages 353–364.
- Jopek T. J., Kaňuchová Z. (2017). “IAU Meteor Data Center—the shower database: A status report”. *Planetary and Space Science*, **143**, 3–6.
- Neslušán L., Poručan V., Svoreň J., Jakubík M. (2020). “On the new design of the IAU MDC portal”. *WGN, Journal of the International Meteor Organization*, **48**, 168–169.
- Roggemans P., Johannink C. and Campbell-Burns P. (2019a). “October Ursae Majorids (OCU#333)”. *eMetN*, **4**, 55–64.
- Šegon D., Vida D., Roggemans P. (2023). “New meteor shower in Draco”. *eMetN*, **8**, 171–176.
- Southworth R. B. and Hawkins G. S. (1963). “Statistics of meteor streams”. *Smithsonian Contributions to Astrophysics*, **7**, 261–285.
- Valsecchi G. B., Jopek T. J., Froeschlé Cl. (1999). “Meteoroid stream identification: a new approach – I. Theory”. *Monthly Notices of the Royal Astronomical Society*, **304**, 743–750.

³ https://www.ta3.sk/IAUC22DB/MDC2022/Roje/pojedynczy_obiekt.php?porz=01594

February Hydrids (FHY#1032) in 2023

Peter Jenniskens

SETI Institute, 339 Bernardo Avenue, Mountain View, CA 94043, USA
pjenniskens@seti.org

An outburst of the February Hydrids meteor shower (FHY#1032) was detected in CAMS data during February 11–17. The meteoroids originated from an unidentified Jupiter family comet. The shower was previously detected in 2013 and 2018. The periodicity is consistent with dust trapped in the 5:2 mean motion resonance with Jupiter.

1 Introduction

The February Hydrids (IAU shower FHY#1032) is a Jupiter-family comet shower that was first recognized in 2018 from twelve triangulated orbits (Jenniskens et al., 2018a; 2018b). Three meteors were also triangulated in 2013, but in other years this shower is mostly absent.

In 2023, the global Cameras for Allsky Meteor Surveillance (CAMS) low-light video-camera networks detected an outburst of the February Hydrid meteors (shower FHY#1032) (Jenniskens, 2023). (See *Figure 1*).

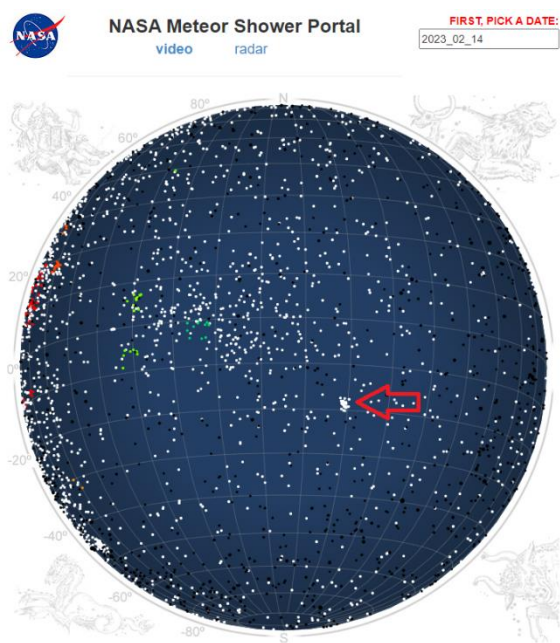


Figure 1 – The concentration of February Hydrid radiants detected by CAMS.

2 The 2023 outburst

The shower was not prominent in any of the individual CAMS networks, but a large number of networks recorded a few shower members. The following camera networks detected this shower: CAMS California (coordinated by

J. Albers, E. Eglund, B. Grigsby, and T. Beck), CAMS Florida (A. Howell), CAMS BeNeLux (C. Johannink, M. Breukers), Lowell Observatory CAMS (N. Moskovitz, S. Hemmelgarn, and B. Rachford), United Arab Emirates Astronomical Camera Network (M. Odeh), CAMS Arkansas (L. Juneau, S. Austin), CAMS Australia (M. Towner, D. Rollinson), CAMS Chile (S. Heathcote, E. Jehin, and T. Abbott), CAMS Namibia (T. Hanke, E. Fahl, R. van Wyk), and CAMS Texas (W. Cooney).

In the period of February 11–17, a total of twenty-nine February Hydrid meteors were triangulated during the solar longitude interval of $321.9^\circ - 327.2^\circ$ (equinox J2000.0) (See *Figure 1*). The median orbit of 2023 is compared with that of 2018 in *Table 1*.

Table 1 – The median orbital elements, and their standard error on the median, for the orbits of the February Hydrids (FHY#1032) triangulated in 2023, compared to those measured in 2018 (Jenniskens et al., 2018b).

	2018	2023
λ_θ ($^\circ$)	324.3	324.6
α_g ($^\circ$)	123.9	123.8 ± 0.1
δ_g ($^\circ$)	+1.5	$+0.4 \pm 0.2$
v_g (km/s)	16.4	16.4 ± 0.1
$\lambda - \lambda_\theta$ ($^\circ$)	161.6	160.7
β ($^\circ$)	-17.8	-18.9
a (AU)	2.68	2.80 ± 0.08
q (AU)	0.812	0.8223 ± 0.0018
e	0.697	0.705 ± 0.006
ω ($^\circ$)	55.5	53.7 ± 0.2
Ω ($^\circ$)	144.3	145.4 ± 0.2
i ($^\circ$)	8.3	8.6 ± 0.1
Π ($^\circ$)	199.8	199.1
N	17	29

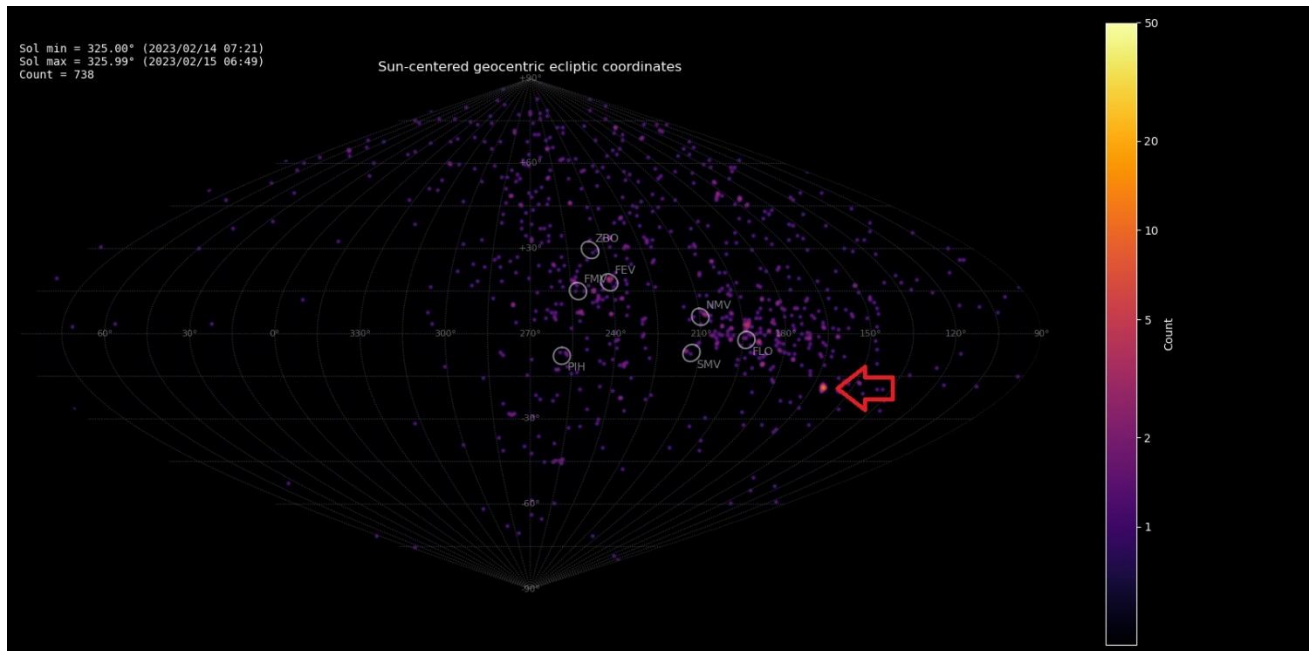


Figure 2 – The concentration of February Hydrid radiants detected by the Global Meteor Network. Image courtesy of GMN.

3 Discussion

The activity of this shower was also detected by the Global Meteor Network, based on public data (Figure 2). In recent years, GMN networks have grown around CAMS BeNeLux, LO-CAMS and CAMS Australia, but the other CAMS networks above provide an independent detection.

The nearly 5-year periodicity of the returns and the 2.8 AU semi-major axis suggests that the shower is due to dust trapped in the 5:2 mean-motion resonance with Jupiter, with a corresponding 4.7-year periodicity. If so, the next return will be in 2027 and/or 2028.

References

Jenniskens P., Johannink C., Moskovitz N. (2018a). “February Hydrids outburst (IAU#1032, FHY)”. *WGN, Journal of the International Meteor Organization*, **46**, 85–86.

Jenniskens P., Baggaley J., Crumpton I., Aldous P., Pokorny P., Janches D., Gural P. S., Samuels D., Albers J., Howell A., Johannink C., Breukers M., Odeh M., Moskovitz N., Collison J. and Ganjuag S. (2018b). “A survey of southern hemisphere meteor showers”. *Planetary Space Science*, **154**, 21–29.

Jenniskens P. (2023). “February Hydrid meteors 2023”. CBET 5231, edited by Daniel W. E. Green, 2023 March 6.

Increased activity 68 Virginid (OAV#00651) in 2023

Yury Harachka¹, Ivan Sergei² and Ruslan Zavadich

¹ Minsk, Belarus

astronominsk@gmail.com

² Mira Str.40-2, 222307, Molodechno, Belarus

seriv76@tut.by

During the night of April 8–9, Yury Harachka and Ruslan Zavadich's video cameras recorded increased activity of the OAV shower (#00651).

1 Introduction

Normally, the minor shower OAV can be barely distinguished from the generally weak activity of the ANT antihelium meteors. However, in 2023, *Yuri Harachka* detected increased activity of this shower.

The analysis of the video data has been made by *Yury Harachka* from Minsk for the observational data from Derazhnoye, Gorodyatichi and Minsk.

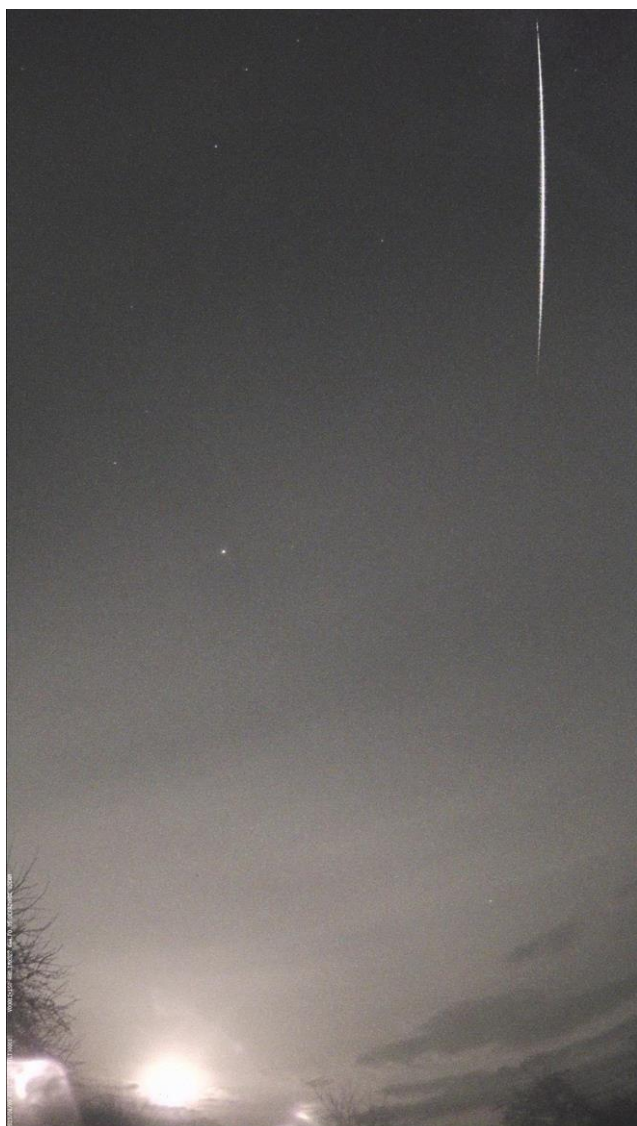


Figure 1 – Bright OAV on April 08 at 22^h15^m13^s UT by Yuri Harachka on video observations in Derazhnoe.



Figure 2 – Bright OAV on April 10 at 21^h18^m32^s UT by Yuri Garachka on video observations in Derazhny.

Figures 1 and 2 show images of bright OAV meteors from the video camera. The meteors moved from bottom to top.

2 Some results

Of the 8 paired meteors during the night of April 8–9, 3 formed a perfect and tight fit compared to the theoretical OAV radiant. The averaged radiant coordinates and orbital elements are compared in *Table 1*.

Table 1 – The average orbit compared to the reference orbit given for the 68 Virginids (OAV#00651).

	2023	Jenniskens et al. (2016)
λ_o (°)	18.478 ± 0.095	16.0
α_g (°)	203.6 ± 0.7	202.0
δ_g (°)	$-14.5^\circ \pm 0.4^\circ$	-13.5
v_g (km/s)	28.2 ± 0.4	28.9
a (A.U.)	2.39 ± 0.06	2.36
q (A.U.)	0.40 ± 0.01	0.392
e	0.831 ± 0.006	0.842
ω (°)	$108.4^\circ \pm 1.6$	109.8
Ω (°)	$198.47^\circ \pm 0.09$	197.4
i (°)	$4.8^\circ \pm 0.3$	4.7
T_j	2.93	2.93

3 CAMS Data

Figure 3 and 4 show OAV shower orbit activity based on CAMS data as of April 16, 2023.

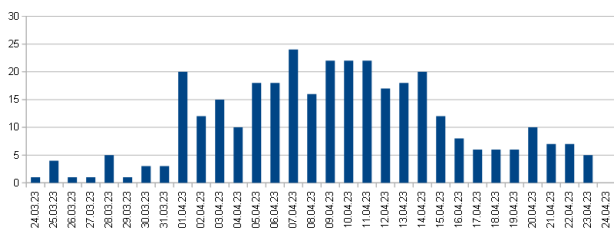


Figure 3 – OAV activity (#00651) in 2022 according to CAMS.

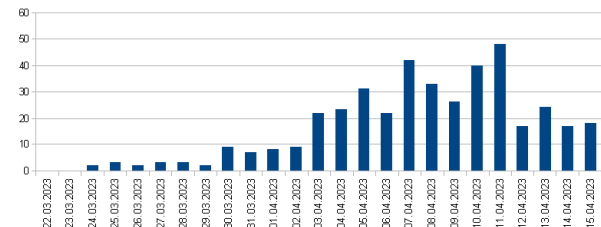


Figure 4 – OAV activity (#00651) in 2023 according to CAMS.

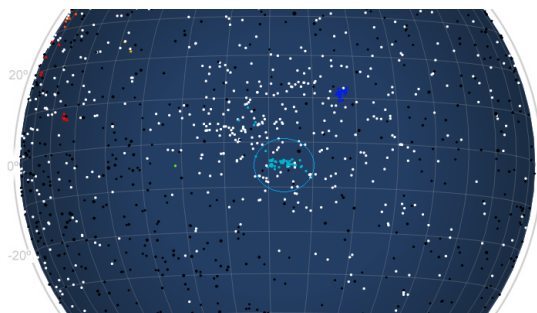


Figure 5 – Radiant position OAV on April 11, 2023 according to CAMS data.

Figure 5 shows the location of the OAV radiant on April 11, 2023 at the time of maximum activity.

4 Conclusion

Data from the Belarusian video network and CAMS data proves that the 68 Virginid (OAV#00651) displayed increased activity in 2023.

Acknowledgments

Thanks to *Yuri Harachka* from the astronomical group “Astronominsk”⁴ and all observers of the Belarusian video network. I thank *Paul Roggemans* for correcting this article.

References

Jenniskens P., Nénon Q., Gural, P. S., Albers J., Haberman B., Johnson B., Morales R., Grigsby B. J., Samuels D., Johannink C. (2016). “CAMS newly detected meteor showers and the sporadic background”. *Icarus*, **266**, 384–409.

Jenniskens P., Gural P. S., Dynneson L., Grigsby B. J., Newman K. E., Borden M., Koop M., Holman D. (2011). “CAMS: Cameras for Allsky Meteor Surveillance to establish minor meteor showers”. *Icarus*, **216**, 40–61.

⁴ http://www.astronominsk.org/index_en.htm

Using GUI RMS on Linux to support multiple cameras

Ed Harman, Peter Eschman, Bob Massey, and Washington Olivera

New Mexico Meteor Array, Albuquerque, New Mexico, USA
 peschman@gmail.com, bobmassey1@gmail.com

This document describes the steps necessary to set up and configure a Linux OS system (Ubuntu 20.04) running a single instance of RMS supporting multiple stations (cameras). Document sections describe initial Linux setup / configuration, RMS installation, adding additional stations (cameras), as well as migrating RPi installed cameras to the Linux based system. Most of these tasks are accomplished using provided scripts, which minimize the chance for configuration errors.

A final Tips and Tricks section provides additional information of use both during installation and later operations.

1 Introduction

Ed Harman wrote much of the initial document as well as the RMS install scripts and helper scripts. *Peter Eschman* worked with Ed, Bob and Washington to develop this GUI RMS Linux system project. Bob and Peter added and expanded a number of document sections.

We used the directory data structure and station specific config file approach pioneered by Washington. *Denis Vida* made changes to RMS to support this project. In addition to this document, we presented a talk titled “The GUI RMS Linux system” in the first session of the 2023 GMN conference, however, since then, we have changed our scripts directory to the one shown in this revised document.

We hope that this document will guide you towards creating a good GUI RMS Linux system for one or more of your cameras.

In this document, we describe the steps necessary to set up and configure a Linux OS system (Ubuntu 20.04) running a single instance of RMS supporting multiple stations (cameras). Document sections describe initial Linux setup and configuration, RMS installation, adding additional stations (cameras), as well as migrating RPi installed cameras to the Linux based system. Most of these tasks are accomplished using scripts we provide, which minimize the chance for configuration errors.

A final *Tips and Tricks* section provides additional information of use both during installation and later operations.

We highly recommend reading through the entire document prior to commencing installation.

2 Overview

Conventionally an RMS station requires three files unique to a single camera:

- .config
- platepar_cmn2010.cal
- mask.bmp

all of which are located within the /home/pi/source/RMS directory on a RPi station (*Figure 1*).

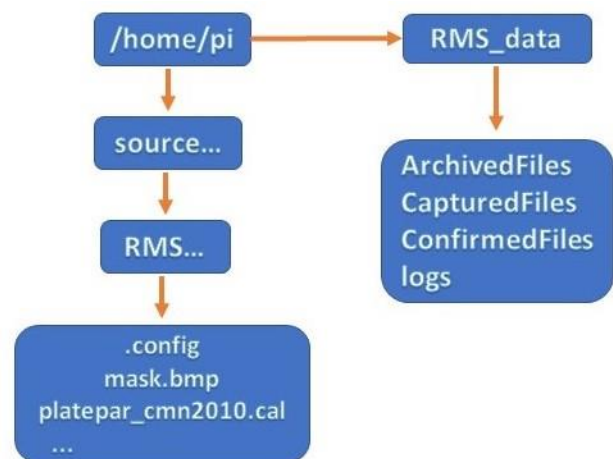


Figure 1 – Directory scheme on the RPi station.

We have developed scripts to modify this directory layout so multiple cameras can be configured under a single user and instance of RMS.

The scripts can be used to turn a ‘vanilla’ Linux Desktop host into something that looks like the familiar desktop that a user sees on the RMS RPi installation for a single station, including desktop launchers for common tasks like:

- ShowLiveStream
- StartCapture
- CMNbinViewer

Users who are not familiar or comfortable using Linux commands from a terminal to perform day to day tasks can use familiar GUI tools from the RMS RPi environment.

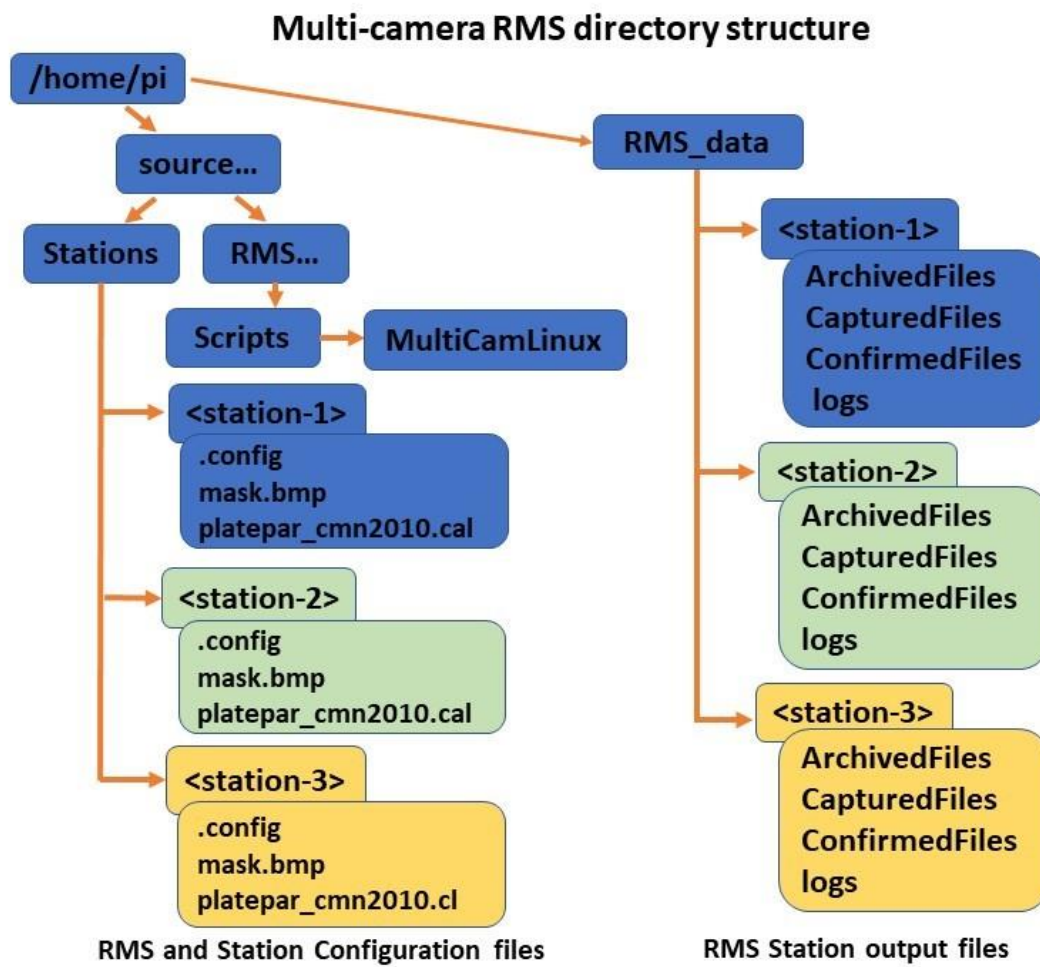


Figure 2 – Multi-camera RMS directory structure. <station-1>, <station-2>, <station-3> refer to folders named after individual GMN camera-ids, e.g. <XX000Y> etc.

These scripts rely upon the fact that the RMS code base has been modified so that it does not matter where the user's three RMS station configuration files are located. Providing you have enabled the vRMS virtualenv (a python tool for creating isolated python environments), RMS will use the station relevant configuration files it finds within the current working directory.

Given that many folks may not be super diligent in checking directory locations, spelling etc., these scripts provide a useful and consistent directory framework to run and maintain an RMS station. These scripts allow the majority of RMS related tasks to be performed via GUI tools.

This structure builds upon the well-known system that RPi RMS users currently use, which provides numerous advantages:

- There is a single RMS installation to maintain and update.
- One or more cameras can be supported within the 'Stations' and 'RMS data' structures.
- The custom scripts described in this document reside in the directory named `~/home/pi/source/RMS/Scripts/MultiCamLinux`. They make no changes to anything installed under the RMS directory tree. Updates to

RMS files can be performed without risk of anything being overwritten because RMS updates will not touch your individual station configuration files.

3 Prerequisites

At a high level the RMS scripts rely upon an Ubuntu Desktop base install. If you think you may need support from others, we suggest that the Ubuntu user you create during the install is called pi. This username is not strictly necessary, but it may make life easier for many folks because it follows existing RPi station conventions.

RMS will run quite happily on relatively low spec hardware. The underlying hardware will determine how many cameras you can support. Our experience to date has shown that anything equivalent to an Intel i3 @2.0GHz with 8GB RAM can support at least two cameras. Our recent testing indicates that an Intel Celeron N5105 @2.0GHz with 8GB RAM can run 6 cameras which can see 360 degrees in azimuth.

All other specs, HDD sizes, etc., are so dependent upon variables such as camera location, weather, time of year, etc., that it is impossible to predict with any certainty how many cameras your specific machine can support.

To give you an idea as to how RMS will perform on a low-end platform, the image in *Figure 3* is a screenshot of a two-camera installation during a recent overnight capture on a pretty rainy night. This processor is an Intel i3-4330 @3.5GHz - circa 2013 vintage, 4GB RAM and a 125GB SSD.

This two camera RMS system runs just fine. Some of us don't normally run Desktops as we prefer to log into hosts remotely and export the DISPLAY variable. In this case, on the rare occasions we need to run a GUI such as CMNbinViewer or SkyFit2, the UIs are pretty responsive and snappy.

Also, for those concerned about networking requirements, you can see from the inbound traffic of the two IMX291 cameras, that the average traffic is a paltry 1MB/s and not 1MiB/s, and not the gnome developers have mistakenly labelled the units.

We recommend these ballpark specs as a starter – i3 or equivalent AMD @2.0GHz clock, 8GB RAM, plus~100GB free HDD storage per camera.

A bare minimum Desktop installation takes up an insignificant ~13GB, however RMS occupies an additional ~37GB of space so as large an HDD or SSD you can afford makes sense.

So, two cameras in real terms are consuming 0.1% of a 1Gb link.



Figure 3 – A two-camera installation during. This processor is an Intel i3-4330 @3.5GHz - circa 2013 vintage, 4GB RAM and a 125GB SSD

These scripts will run under most flavors of Linux. However, each distribution has its own preferences with respect to display managers and default installed applications. We have standardized on Ubuntu 20.04.5 LTS. This release is slated to be retired in 2025 and by that time a lot of other things will have likely changed, so this version is a safe bet for now.

The scripts only rely upon bash, awk and sed to run, which are installed by default for most Linux distros. The only area where these scripts might break in other distributions

will be GUI desktop shortcuts, where we know first-hand that the GUI has subtly changed even moving to Ubuntu 22.04 Desktop LTS.

After the base Linux desktop installation, you will need to deploy RMS and at least two of the three RMS scripts mentioned in this document.

4 How to create your RMS Linux RMS system from scratch

If you already have a Ubuntu compatible Desktop installed proceed to the *section Install RMS on Linux RMS system*.

Step by step install instructions

Install Ubuntu Desktop 20.04.5 LTS

Transfer a downloaded .iso onto a USB stick or burn to CD if you prefer. You can load it onto a USB stick with Balena Etcher or Rufus. If you experience problems with Etcher, try Rufus instead.

Place your chosen media into the new hardware and within the BIOS (or by whatever function key your BIOS supports), select boot from the inserted media.

By default, Ubuntu performs a check of the installation media which can take a while so you can bypass this by hitting CTRL-C to cancel it.

If you run into problems during the install steps, and you become concerned about your .iso download, then check Canonical's website for the iso checksums and compare with what you have downloaded.

Upon boot, the installation it will read a lot of data into RAM and eventually launch an X-11 screen with the live temporary Ubuntu desktop running, showing the options displayed in *Figure 4*.

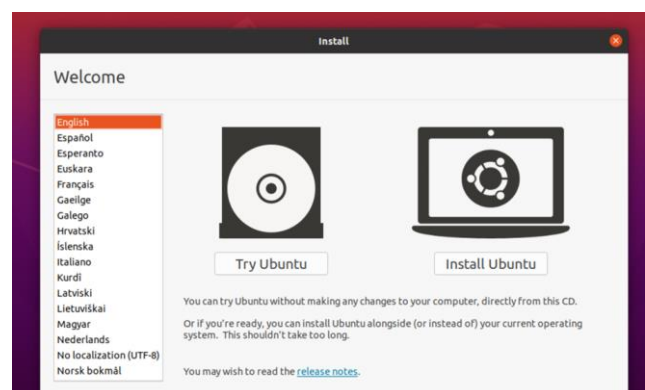


Figure 4 – Ubuntu desktop running: different options.

The installer will attempt to auto detect your location and corresponding language and keyboard layout. It is important to ensure that these are correct before proceeding.

Select <Install Ubuntu>

Select the desired language & keyboard layout, Continue.

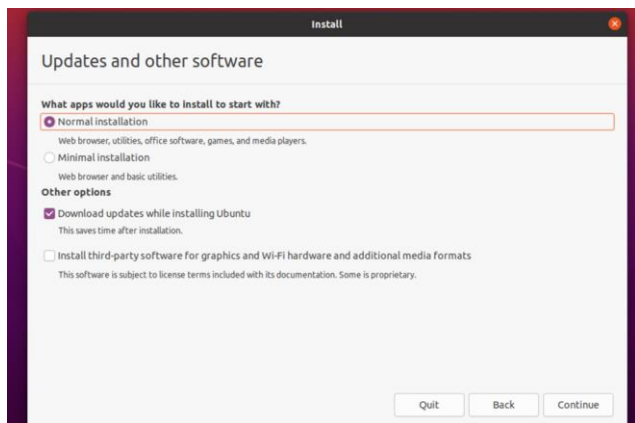


Figure 5 – Ubuntu installation: different options.

Select “Minimal installation” (Figure 5) if you want to conserve space and press <Continue>.

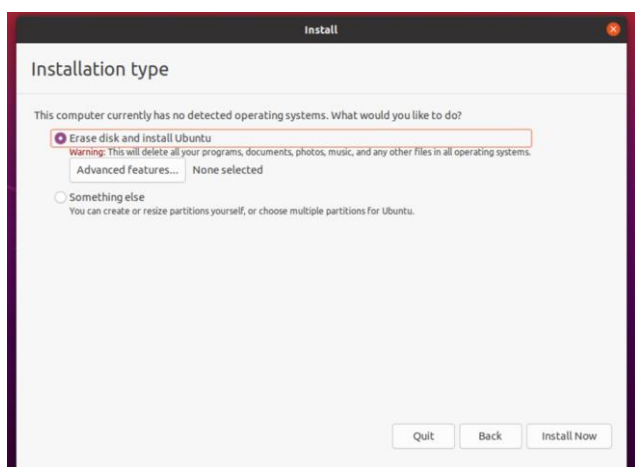


Figure 6 – Ubuntu installation.

If your existing disk contained a recognizable o/s you will be prompted to install alongside it (create a dual-boot machine) or erase existing content and overwrite. The choice is yours. In this example it is a fresh disk which it thinks has something on it but it is in fact empty so Erase and install is ok (Figure 6), -> <Install Now>



Figure 7 – Ubuntu installation.

You’ll get this ‘last chance’ to change your mind (Figure 7) -> <Continue>

The installer discovers your ISP public IP address and performs a lookup (likely via IANA) to determine your country/region (Figure 8).



Figure 8 – Ubuntu verifying your location.

Accepting the default is fine, as is the time zone offset for your region along with regional keyboard, language and numeric formatting settings. Since the RMS standard time zone is UTC, the scripts you run later will automatically set your time zone to UTC.

-> <Continue>

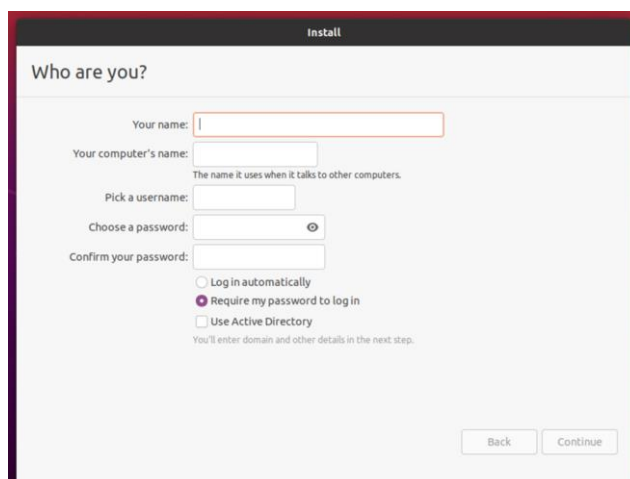


Figure 9 – Ubuntu personal data.

Enter your details as you wish (Figure 9). If you wish to emulate the RPi station behavior, then enable auto login. Some of us prefer not to enable auto login, but that’s just a personal preference, when complete -> <Continue>

Note: If you are configuring a remotely managed station, you are strongly advised to enable auto logon. Sometimes a session will crash, and auto logon will prevent a problem when the X-11 server dies and control returns to the login page. When stuck on the login page there will be no X-Server session running, so your configured cameras will not restart and, effectively, your station will not be recording any data because it is down.

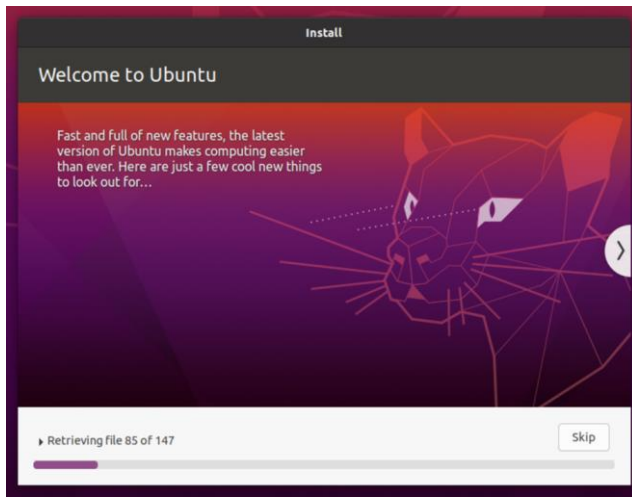


Figure 10 – Ubuntu installation screen.

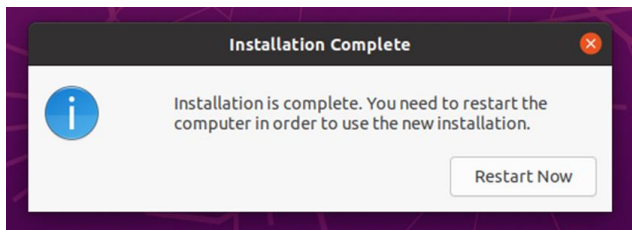


Figure 11 – Ubuntu installation screen.

The operating system will then proceed to install (Figures 10 and 11).

Select <Restart Now>



Figure 12 – Ubuntu installation screens.

Eject CD or remove USB key and press <Enter> (Figure 12).

The system will restart and then you can log in using the credentials entered earlier.

We will now install RMS on the Ubuntu based Linux system.

Install RMS on a Linux Ubuntu system

Open a terminal window and get the required RMS installation file:

```
wget
https://raw.githubusercontent.com/CroatianMeteorNetwork/RMS/master/Scripts/MultiCamLinux/GRMSL\_Install.sh
```

With the shell script downloaded to your home directory, make it executable by typing in the terminal:

```
chmod +x *.sh
```

then type

```
./GRMSL_Install.sh
```

The script will likely prompt for your password and then the lengthy installation process will commence. The script will automatically call additional scripts as needed.

On Ubuntu, you will be prompted to accept an EULA license for the TrueType fonts and you will have to navigate the EULA screens. At the first screen, hit the tab button and the <OK> box should be highlighted red, then hit return. At the second screen hit the tab once and the <Yes> option should be highlighted in red, then press return – the install process will then continue to completion.

The install script may take some time depending on your hardware, but install time is usually under 30 minutes. At the end of the install steps, the script will give you the option to add some additional software packages, and then schedule a cron job for the GRMSUpdater script, which can stop all running RMS instances, perform an RMS update and then restart all configured stations.

Don't worry if you enabled the cron job and later wish to reschedule it. Just enter

```
crontab -e
```

and you can edit or delete the scheduled job to suit any time you wish.

At the end of the GUI_RMS_Linux_Install script, you will be asked “Do you wish to configure some stations?” if you say yes, it will call add_GStation.sh to install stations, or you can elect to run the add_GStation script manually later.

The add_GStation script will add the first station (camera) or set of stations by creating the RMS station directories and populating them with starting copies of the station files.

Note: For detailed descriptions of the add_GStation, GRMSUpdater and Migrate scripts, please refer to the *Script Details* section of this article.

If you are migrating existing RMS RPi cameras to this Linux installation, please refer to the section “Moving existing stations” to your Linux RMS system at this point. Otherwise, you will need to customize each station's .config file.

Each station's .config file is located relative to your current working directory (~ /source/RMS) at ../Stations/<station-id>/.config

Use whatever editor you feel comfortable with (we use nano in the following example) to edit each .config:

```
nano ../Stations/<station-id>/.config
```

Use the editor to update these fields:

- Your camera location details.
- Your camera connection device string with appropriate IP address.
- Any other options you wish to change, such as post processing jobs, ssh keys, etc.

We do not recommend a daily system reboot after analysis is complete, since RMS will run for many months on Linux without requiring a system restart. Also, if multiple cameras are installed, we do not want any reboot until all stations have finished processing data. In any case, the recommended cron job will provide functionality equivalent to an RMS reboot every week, or more often if you desire.

If you close your terminal window now, and re-launch Gnome terminal or the newly installed lxterminal, you will see that the session now automatically places you in the vRMS env in directory ~/source/RMS.

If you log out and log back in, the X-Session will start, and then it will auto-launch lxterminal windows bearing the station name in their title, and RMS will commence for each camera.

After RMS has reached the ‘waiting to commence capture’ line you can use the file browser to view each station’s log files and review the initially empty Archive and Capture directories within ~/RMS_data (or another mount point if you chose that option).

You can run the add_GStation script multiple times to add additional stations. It will not overwrite anything nor allow you to add duplicate station names. For example, if you acquire a new camera at a later date, and have the computed resources to host it, you can easily add it to your existing configuration.

Setting your camera IP address

Next you will need to configure your camera’s IP address, so it is accessible from your Linux RMS system. New IMX-291 cameras usually come from the vendor with their IP address set to 192.168.1.1. You may need to reset this number so that it is on the same subnet as your Linux RMS system and is not set to the Gateway IP address. You can use the CMS utility to alter the camera address. CMS is the utility often used to configure all the other camera parameters. If you need more help setting a good IP address for your camera, you may find helpful information in the next section about changing the address for an existing camera.

After you have configured your station cameras you can check each camera’s connectivity by launching the desktop <StationID>-ShowLiveStream link(s).

Moving existing stations to your Linux RMS system

If you are moving existing stations, you can manually copy files or run the Migrate script to bring across these RPi station files:

- .config
- platepar_cmn2010.cal

- mask.bmp
- .ssh/id_rsa

If you are doing this manually, then the first three files need to be placed into the ~/source/Stations/<station-id> directory you created earlier using the add_Gstation script. The fourth file .ssh/id_rsa (private key file) needs to be copied to the .ssh directory for the user you have established for the Linux RMS system. If you need to copy more than one private key file, be sure to rename any duplicate filenames and reference them correctly on the .config line that specifies the location and file name of the private key file for that station (camera). This .config parameter is:

```

; Path to the SSH private key.
rsa_private_key: ~/.ssh/id_rsa

```

The Migrate script can be used to automate moving an existing station. The script will prompt you for your RPi’s host address and will initially attempt to copy your current RPi username’s public key to the RPi.

In this context, the IP may be the local IP address of the RPi, or the OpenVPN designation if you are using the OpenVPN from GMN. An OpenVPN designation would look like

```
<stationID>.gmnet, so XX000X.gmnet.
```

Because this is probably the first time this host has seen the RPi you will get a warning that the RPi’s ECDSA fingerprint is not recognized by your new Linux host, do you want to proceed?

```
Type yes <Enter>
```

After this, the script will attempt to install your public key onto the RPi, and it will prompt you for user pi’s password on the RPi.

Once this is entered, the script will install the public key into the RPi’s authorized hosts file, and then the script will use scp to transfer:

- .config
- platepar_cmn2010.cal
- mask.bmp
- .ssh/id_rsa

to a temporary directory on your Linux host.

The script then looks into the .config, parses the station id, and uses that to copy platepar_cmn2010.cal & mask.bmp to ~/source/Stations/<station-id>.

Next, it copies your RPi’s private key id_rsa to .ssh/<station_id>_id_rsa.

Finally, it updates that stations’ .config to set the field id_private_key: ~/.ssh/<station-id>_id_rsa

This last step means that you don’t need to email Denis Vida with your hosts’ new public key, since you can continue to

use the one already authorized for your RPi’s camera. You can run the Migrate script as many times as is necessary.

Finally, we need to change the old camera IP address to one that is on the subnet seen by the Linux RMS system.

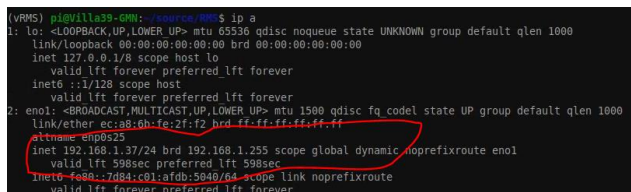
If you are using an unmodified RPi image, the camera is connected directly to the RPi’s ethernet port and the RPi’s ethernet port is assigned the default static address of 192.168.42.1/24. Using the default RMS image, the camera will have the default address of 192.168.42.10.

You will need to complete these steps to migrate a camera from your RPi RMS to your Linux RMS local subnet:

1. Determine your Linux RMS systems’ local subnet. From a lterminal prompt type the following:

```
(vRMS) pi@raspberrypi:~/source/RMS$ ip a
```

The result will be a multi-line response (Figure 13):



```
(vRMS) pi@villag9-0M: ~$ ip a
1: lo: <LOOPBACK,UP,LOWER_UP> mtu 65536 qdisc noqueue state UNKNOWN group default qlen 1000
    link/loopback 00:00:00:00:00:00 brd 00:00:00:00:00:00
    inet 127.0.0.1/8 scope host lo
        valid lft forever preferred lft forever
    inet6 ::1/128 scope host
        valid lft forever preferred lft forever
2: en01: <BROADCAST,MULTICAST,UP,LOWER_UP> mtu 1500 qdisc fq_codel state UP group default qlen 1000
    link/ether ec:a8:6b:fe:2f:f2 brd ff:ff:ff:ff:ff:ff
    inet 192.168.1.37/24 brd 192.168.1.255 scope global dynamic noprefixroute en01
        valid lft 598sec preferred lft 598sec
    inet6 fe8a::7d84:c01:afab:5940/64 scope link noprefixroute
        valid lft forever preferred lft forever
```

Figure 13 – Multi-line response.

In this case our Linux system’s address is 192.168.1.37. Therefore the subnet is 192.168.1.xx. Now that we know what the subnet is, we want to assign a permanent (static) address that is not currently in use. You can query your router to see what addresses have already been assigned. If it is not feasible to query your router, you may try using a number in the 200 to 255 range, which is often not used by dhcp (for instance 192.168.1.202).

2. Log on to your RPi and set the camera to its new static IP address. Start a terminal window and type the following command:

```
<within the vRMS env> python -m Utils.CameraControl SetParam Network HostIP <your new IP>
```

At this point the RPi will lose connectivity to the camera.

3. Disconnect the camera from the RPi and plug the camera cable into a spare ethernet port on your system.
4. Edit the .config file and change the device string to the new static IP address. Change the first line under the [capture] section:

device:

```
rtsp://192.168.42.10:554/user=admin&password=&channel=1&stream=0.sdp ; device id
```

to something like this:

device:

```
rtsp://192.168.1.202:554/user=admin&password=&channel=1&stream=0.sdp ; device id
```

If all is well, you should now be able to ping the camera on its new IP from the Linux host and run the Desktop LiveViewer shortcut to ensure all is working as expected.

5 Script details

This section provides further information about each of the scripts used in creating and operating a GUI RMS Linux system. If you experience problems with the installation of RMS, these details may be useful.

There are two required and one optional script. The scripts are all located in ~/source/Stations/Scripts

add_GStation.sh

```
~/source/RMS/Scripts/MultiCamLinux/add_GStation.sh
```

This script takes a vanilla RMS install and adds the required directory structures and desktop environment shortcuts. The script can accept an optional argument that specifies the path to a custom data storage location should the default location not suit your needs. Please see the section “Some additional tips and tricks” for further details.

The add_GStation script will prompt the user to enter each station camera code, which was assigned to that camera by the Global Meteor Network. It will then prompt for the next station code.

By default, the script will set the user’s data directory for each stations capture data to be

```
~/RMS_data/<station-id>
```

When a blank station code is entered by simply hitting the return key, the script will generate the required per-station directories, and desktop shortcuts, and make global changes to the user environment to mimic the look and feel of RMS running on an RPi. Tasks include:

- Modifying the user env to auto enable vRMS.
- Disabling screen lock when the system is idle.
- Creating autostart entries that are launched at login or reboot.
- Configuring other system defaults.

As indicated earlier, this script will create a default crontab entry to schedule stopping RMS, updating RMS code, and restarting the stations (this uses the GRMUpdater script discussed next). You can modify the timing of the cron job on the fly at this point in the script execution.

Note: We originally considered parsing one of the user’s .config files to get the geolocation codes and scripting a suitable time to auto schedule the job, however at this time we have not worked out those details, so the default schedule is to run every Sunday at 1500 UTC.

Post install, the cron entry can be modified anytime by opening a terminal and typing:

```
crontab -e
```

This website⁵ has a useful list of common scheduling options should the user require help.

If you are curious about other settings that are changed – and there are a lot – we would suggest opening up the `add_GStation` script in your editor of choice and perusing the code – it is fairly heavily commented so it should be fairly obvious what each step does.

GRMSUpdater.sh

```
~/source/RMS/Scripts/MultiCamLinux/GRMSUpdater.sh
```

This script performs three functions – stop all running RMS instances, perform a regular RMS update and finally restart all the configured stations. This script is best run as a scheduled cron job to perform these three functions on a regular basis. It is not meant to be run standalone, but can be run it that way if you wish. It can take an optional argument to alter the default behavior.

1. If run with no argument it will kill all running RMS processes, perform a regular `RMS_Update`, and then look in the user's Stations directory to start every station it finds.

2. If it is run with any argument the mode of operation changes – instead of restarting all configured stations it will only restart those stations that were originally running before the script started. This way, if a user is hosting three cameras, and one of them is not functioning for whatever reason, the user can kill the capture process from the `lxterminal` window by either typing a `CTRL-C` in the session, or by closing the window. Ordinarily the updater process will restart it, but if the user has an inoperative camera, they can set a flag – any character (other than `#` or `\`) at the end of the `crontab` entry. In this case, the script will scan the running system and gather a list of currently running station names, then following the RMS code update, it will only restart those previously running stations.

Migrate.sh

```
~/source/RMS/Scripts/MultiCamLinux/Migrate.sh
```

If you are migrating existing stations already configured on a RPi, or any other platform, then you can transfer the files by hand using whatever tools you are comfortable with, or use this utility script to automate the process.

Note: For this script to work you need to have previously run the `add_Gstations` script to generate the related station directory structure.

`Migrate.sh` automates copying from any RMS host the following files:

- `~/source/RMS/.config`
- `~/source/RMS/platepar_cmn2010.cal`

- `~/source/RMS/mask.bmp`
- `~/ssh/id_rsa`

`Migrate` will transfer these to a temp dir on the previous RMS host, extract the station name from the `.config` file, and then move all these files to the appropriate `~/source/Stations/<station_dir>/` folder on the Linux installation.

Note: The `ssh id_rsa` private key will be renamed and moved into `~/ssh/<station-name>_id_rsa`, and that station's `.config` file will be updated so that `rsa_private_key` points to the renamed private key.

The only requirement for this script to work is that `ssh` access is enabled on the RPi. This can be confirmed or achieved by navigating to the top left RPi icon - `>Preferences->Raspberry Pi Configuration->Interface` tab and then checking or selecting the `ssh` enable radio button as shown in the next graphic (*Figure 14*).

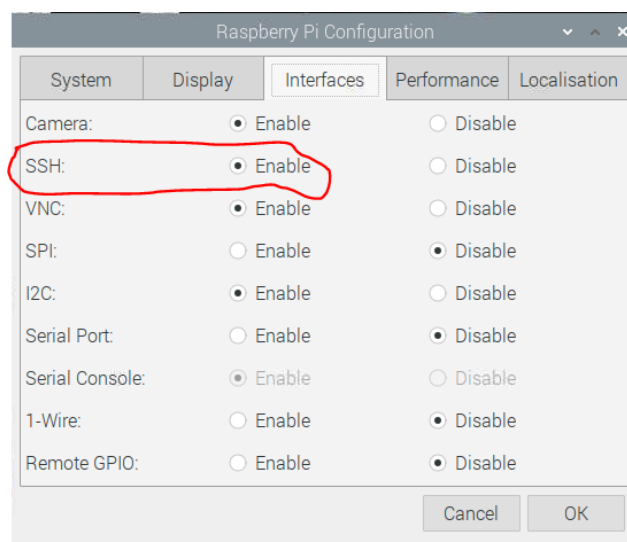


Figure 14 – Raspberry Pi Configuration, Interface tab.

The script itself prompts the user for the Pi's IP address, and then using user `pi`, it attempts to place your host's public key into the RPi's authorized hosts file. The RPi hosts IP address can be found by typing in terminal `ip a` – (*Figure 15*)

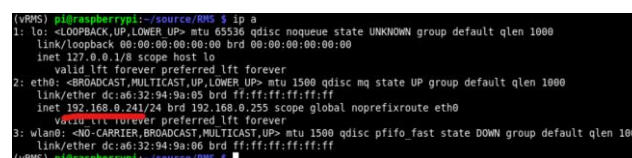


Figure 15 – The RPi hosts IP address.

It will also prompt you for user `pi`'s password to execute the copy, then uses Linux secure copy (`scp`) to transfer the required files to the local host's `tmp` dir.

⁵ <https://crontab.guru/examples.html>

Below is an example Migrate.sh script run along with some explanatory notes:

- (vRMS) eharman@rms-test:~/source/RMS\$./Migrate.sh
- Enter the RPi's IP address:

If this host's keys are not present on raspberrypi, you will be asked to add the host's unique fingerprint to your `~/.ssh/known_hosts` file, so when prompted, answer 'yes'.

Next you will be prompted for the user pi's password to copy the key to the `authorized_keys` file located in the `~/.ssh` folder on the RPi.

Below is example dialogue for entering host's unique fingerprint:

- `/usr/bin/ssh-copy-id`: INFO: Source of key(s) to be installed: `"/home/eharman/.ssh/id_rsa.pub"`
- The authenticity of host 'raspberrypi (192.168.0.239)' can't be established. *<-this is my host verifying I want to connect to this host since its fingerprint isn't in my .ssh/known_hosts file.*
- ECDSA key fingerprint is SHA256:BMobzcaupuWf3q56dvzuoCL9xio5v0CcW3DEUPmshZk.
- Are you sure you want to continue connecting (yes/no/[fingerprint])? *Yes -user input to accept hosts fingerprint.*
- `/usr/bin/ssh-copy-id`: INFO: attempting to log in with the new key(s), to filter out any that are already installed.
- `/usr/bin/ssh-copy-id`: INFO: 1 key(s) remain to be installed *if you are prompted now it is to install the new keys.*
- pi@raspberrypi's password: *<- pi's password entered here.*
- Number of key(s) added: 1 *<- host has put my hosts pub key in its authorized_host file so now passwordless ssh/scp can take place.*

Now log into the machine, with "ssh 'pi@raspberrypi'" and check to make sure that only the key(s) you wanted were added.

- `.config`
100% 13KB 9.1MB/s 00:00
- `mask.bmp`
100% 901KB 52.7MB/s 00:00
- `platepar_cmn2010.cal`
100% 12KB 8.6MB/s 00:00
- `id_rsa.`
100% 396 597.0KB/s 00:00
- Found station UK001C !

Station UK001C's `.config` has been moved, `RMS_data` location updated, `mask.bmp` and `platepar_cmn2010.cal` have been moved unchanged to the following directory -

- `/home/eharman/source/Stations/UK001C`

Whether you have used the Migrate script or moved files manually, it is still necessary to migrate your camera hardware network address to the new Linux system.

6 Some additional tips and tricks

Backup your configuration

We strongly recommend that you backup all `~/source/Stations` once things are working well. This will give you a good disaster recovery backup should you need to recover from problems later. We may consider providing a script to automate this backup.

Delay upgrading to Ubuntu 22.04?

As indicated earlier, we recommend installation using Ubuntu 20.04, which is not slated to be retired until 2025.

The newest version of Ubuntu is v22.04. However, this version introduces difficulties with Wayland graphics that interfere with remote connection utilities including AnyDesk, NoMachine, RealVNC viewer, and possibly others. We anticipate that these remote connection utilities will eventually incorporate fixes for this problem, but until then, it may be wise to avoid upgrading to Ubuntu 22.04.

You should have no problems running RMS on Ubuntu 22.04 if you don't need remote connection capability. Ubuntu frequently offers to upgrade from v20.04 to v22.04. Although you do want updates that fix potential problems with v20.04, you may not want to run the risk of accidentally saying you want to upgrade to v22.04. You can tell Ubuntu not to offer updates to v22.04 by going into Settings, About, Software & Updates, Updates and set "Notify me of a new Ubuntu version: Never".

Storage Configuration

If you are repurposing old hardware, it may be appropriate to add a faster higher capacity HDD or SSD. Also, instead of merely swapping out the old drive and replacing it with a new one, if your machine supports dual drives, you can add the 2nd drive and reserve it for camera data, while leaving the original HDD for the operating system and RMS codebase:

- Drive#1 - Operating system + RMS codebase
- Drive#2 - RMS camera data storage

Typically, the operating system and RMS codebase do not impose heavy i/o loads to the disk-subsystem, however when RMS writes to capture and log directories, we do see fairly heavy i/o, particularly at the end of a night's run, when the captured data is processed. Moving this captured and processed data to a separate HDD or SSD may be a sensible option for you.

If you do take this route then there are numerous ways to effect that change:

1. The simplest way is to mount the additional drive to the directory `~/RMS_data`

2. One could achieve the same result by mounting the new drive to a directory in the root filesystem e.g., /BigDisk and then creating a symbolic link named ~/RMS_data and pointing that to the real mount point /BigDisk:

```
rmdir ~/RMS_data
ln -s /BigDisk ~/RMS_data
```

There is no measurable overhead in doing it the second way.

3. You could mount the new drive before the mount point /BigDisk and then when using add_GStations.sh pass the target RMS storage directory as an argument:

```
~/source/RMS/Scripts/MultiCamLinux/add_GStation.sh /BigDisk
```

Then the script will create each station's storage directory to be subdirectories under /BigDisk and it will amend the stations' .config to reflect that change.

The options above are a few examples of the many possible ways you can achieve this.

Your old ExternalScript is set to reboot the station?

If you typically run an ExternalScript that is set to reboot at the end of capture and data processing, you should disable the reboot, since frequent reboots are not necessary on Ubuntu 20.04. In addition, it is not appropriate for one camera that has finished to call for a reboot before all other cameras are done processing!

New stations have their default .config changed to have the following set:

```
reboot_after_processing: false
```

However, if you have subsequently copied over your old RPi .config you may want to edit this value, because it is set to true in a default .config file.

iStream.py is an example of an external script that typically reboots the RPi station. In late December of 2022, iStream.py was modified so it will only reboot if run from a RPi station, so it will not cause any issues for an RMS Linux multi camera system.

File sharing

If you are using a PC, Laptop or other device as your day-to-day host, e.g., read mail, browse the internet, and such, you may want to install a file sharing mechanism that will allow you to map the RMS capture directory to that host. If you do this, you will be able to peruse the captured data and data summaries, logs, etc., remotely from the Linux RMS host without having to actually log on to the physical host running RMS.

There are numerous options to choose from, however, we will only detail SMB since that's what we primarily use between hosts and Windows desktop. This will also work for Mac users.

In a terminal window:

```
sudo apt install -y samba
```

once installed, in your favorite editor open the following file and add the content below:

```
nano /etc/samba/smb.conf
```

navigate to the end of the file and add:

```
[RMS_data] <- sharename
path = /home/<username>/RMS_data <-replace with your
username
p browsable=yes
p read only=yes (set to no if you want to run CMNbinViewer on
your desktop and have the capability of it writing data to your
/RMS_data/<station-id>/CapturedFiles directory)
p guest ok=no
```

Save the file, and note that you do not need to restart the SMB Daemon service because it will reload the smb.conf when it sees that the contents have changed.

Next, you need to add your user account to SMB's list of known users - this is separate from the usual Linux authentication scheme as it allows Samba to integrate with Microsoft Domain structures. To add yourself as an authorized user, in a terminal window type:

```
smbpasswd -a <your username> # once you press Enter,
you will be prompted for your password, this can be
different to your Linux password, however in practice it's
safe to use the same one if you wish. The utility will ask you
then to Re-type your password:
```

- New SMB password:
- Re-type new password:

That's it, you are done configuring the Linux host!

Next, from your windows desktop machine, open the filemanager and rightmouse over 'This PC' and from the dropdown menu select map a drive.

Sometimes Windows can be a bit picky at this point, you can either use the Browse button to let it auto discover available shares or you can enter the full UNC path to the share you've just created which takes the form:

```
\\hostname\sharename
```

Whichever route you choose make sure you tick the box 'Connect using different credentials'

Hopefully it should find your new share and prompt for your hosts logon credentials, at which point Windows will mount the share to the next free drive letter on your system, and you can click on it and see the data.

You don't need any fancy graphics application installed onto this host to view a stacked image of the nights run, or indeed any of the other graphics that are found in a typical night capture directory, you can merely drag the image from a file-browser window into an opened web-browser page

and the browser will open a new tab and display the image - it really is that easy once you have things set up!

There are numerous other integration tools available for both Windows and Apple platforms that would allow you to manage your RMS capture host remotely, but that will need to be covered in a future Wiki entry.

Using AnyDesk to manage your Linux RMS system remotely

AnyDesk provides mechanisms to connect to and manage your Linux RMS system remotely. It does not rely on any ssh key validation or the OpenVPN addressing that can be provided by GMN. AnyDesk provides the means to copy files to and from the RMS system. We will not attempt to provide full AnyDesk documentation here, however, we do recommend setting a good password on AnyDesk installed on your Linux RMS system. If you do not install a password for remote access, someone with physical access to the RMS system will have to authorize every AnyDesk connection you try to make to the RMS system.

To set a password, click on the icon showing four horizontal lines located near the upper right-hand corner of the AnyDesk window. If you hover the cursor over this icon, it should display the word “General”. Under “Security” you need to “Unlock Security Settings” then enable unattended access, and set a good password.

Typically, when you connect using AnyDesk you will see the screen of the Linux RMS system. Just to the left of the icon with the red underline near the upper right-hand corner of the AnyDesk screen you will see the outline of a file with a right arrow inside it. If you activate this icon, you will switch to a file transfer screen, allowing you to copy files to and from the Linux RMS system. After file copy, you can switch back to the first icon and display the screen of the Linux RMS system again.

Using RealVNC to manage your Linux RMS system remotely

If you are used to using RealVNC for remote connections, please be aware that although it is free to use on RPi, you may be required to purchase a license to use the RealVNC viewer to connect to your Linux RMS system.

Modifying icons on taskbar

If you have allowed the add_GStation script to install the pcmanfm file manager, and mousepad text editor, you may wish to replace default favorite apps on the left-hand taskbar of the GUI screen. For instance, you may also want to add lxterminal as a favorite on your taskbar in place of the default terminal app. To do this, click on the icon showing a 3 × 3 array of dots at the bottom of the taskbar, locate the new software icons among the GUI tools menu, right click the icon and select “Add to Favorites”. At this time, you may also want to locate the similar default app icons in the taskbar and right click “Remove from Favorites”. Note that any desktop icons for folders will still open using the original default file manager, so they will not behave the way they do when opened with pcmanfm file manager.

If you want a graphic display of system usage

You can use GUI monitoring tool and add it to Favorites on the left-hand Taskbar:

Open Utilities icon

System Monitor (right click to add to favorites)

- Click the middle tab “Resources”
- Click Preferences, Resources, Update interval in seconds
- For instance, setting to 3 seconds will graph activity over the last 180 seconds)

If you need to use OpenVPN

OpenVPN is provided by GMN for remote connections. You can configure it by running a command from a terminal window. Open a terminal window, which should start up in ~/source/RMS, and type:

```
Scripts/DownloadOpenVPNconfig.sh <StationID>
```

Keep in mind that although you may have multiple stations installed on your Linux RMS system, you can only do this for one OpenVPN designation. It might be wise to pick the lowest station ID and use that to link a single OpenVPN designation to the RMS system.

Changing which stations start at reboot/login

If one or more of your stations (cameras) is not working properly and you want to take it out of service for a while, you can have that station skipped at reboot/login. You can use the GUI tool “Startup Applications Preferences” to remove or restore a checkmark next to the stations you want to start or not start at login/reboot. If you do this, please remember to run the GRMSUpdater script from cron with trailing argument so that only currently running RMS sessions are restarted.

Another way to disable one or more of your stations is to simply cut the station directory out of ~/source/stations and paste it into your home directory. After things have been repaired, cut the directory out of your home directory, and paste it back under ~/source/stations to enable the station again.

Desktop shortcut file names

When you use the file manager (pcmanfm), please be aware that the file manager detects the .desktop extension and displays the Name field attribute of the .desktop object, and *not* the actual filename of the object. The actual file names can be seen by using ls command from a terminal session. For example, if you see these names in the file manager:

- XX0001-ShowLiveStream.desktop
- XX0001-StartCapture.desktop

They will correspond to these actual filenames (ls -l ~/Desktop):

- -rwxrwxr-x 1 pi pi 195 Nov 10 19:34 Show_LiveStream-XX0001.desktop

- `lnwxrwxrwx 1 pi pi 50 Nov 13 18:10
XX0001_StartCap.desktop ->
/home/pi/.config/autostart/XX0001_StartCap.desktop`

Performing a maintenance task on all your stations

If you have a task you want to perform on all of your stations, you may want to take a look at the GRMSUpdate script. You can use a similar code block to iterate over all the stations on your Linux RMS system.

Adding a new station to an existing Linux RMS system

If you are adding a new station to a Linux RMS system that has been running one or more stations for a period of time, make sure there is ample free space on your storage drive so that the new station will be able to start capture. The new station will not yet own any files it can delete to free up space, so it will not be able to honor the `extra_space_gb`: value you have set in your `.config` file when it starts capture for the first night. As time goes by, you may find you need to manually delete `CapturedFiles` directories and possibly `ArchivedFiles` directories on some earlier stations so that a new station can get caught up and be able to retain data for the same number of nights as the older stations.

Cabling and component examples

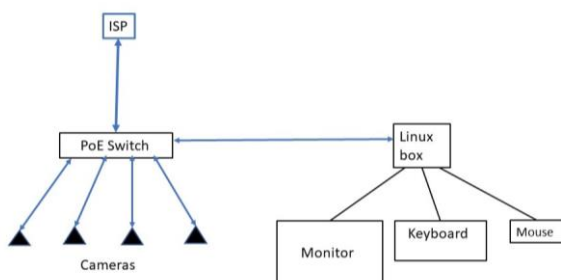


Figure 16 – An example of a simple installation.

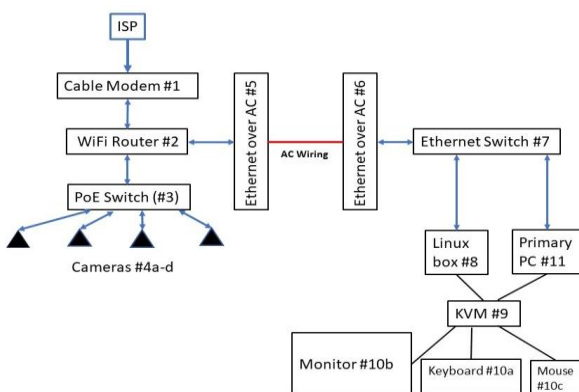


Figure 17 – An example of a simple installation.

There are a number of things to consider when you run cables to the Linux RMS system. In most cases, it makes sense to add a PoE (Power over Ethernet) switch, located where the cables home from the cameras. One port of the switch is used to connect the switch to the rest of your local network by way of an Ethernet cable which runs to your home router. You can co-locate the Linux RMS system near the PoE switch, or you can place the Linux RMS system anywhere else you like, by using a long Ethernet cable to

connect from a second location to the PoE switch. This “long Ethernet cable” can actually be two devices that allow you to send Ethernet over the AC wiring of your house.

Given that each camera only sends about 500 Bps, even a slow link at 200Mbps will be enough to support 40 cameras! You may wish to add a KVM (keyboard/video/mouse) switch, which allows you to use your primary computer monitor, keyboard and mouse on the Linux RMS system alongside your primary home computer.

We don’t think running cameras over a Wifi link is a good idea, however you might be able to do this using high-end hardware.

The diagram in *Figure 16* shows an example of a simple installation, followed by a diagram of a more complex install. Details about each numbered part on the more complex configuration are given in the text following the second diagram in *Figure 17*.

Equipment in the back room of house:

- Netgear cable modem:
CM500-1AZNAS (16×4) DOCSIS 3.0 Cable Modem (#1)
- Netgear wifi router
Netgear Nighthawk X6S, AC3000 Tri-Band Wifi Router, Model R7900P (#2)
- TP-Link 4 port PoE switch with one non PoE port
TL-SG1005P V2 or later, 5 Port Gigabit PoE Switch, 4 PoE+ Ports @65W (#3), cables from up to four cameras (#4a-d) are connected to this PoE switch, and one cable from PoE switch is connected to Netgear wifi router
- TP-Link AV1200 Gigabit Powerline ethernet Adapter (Ethernet over AC wiring) (#5)
cabled to Netgear wifi router

Equipment in the front room of house:

- TP-Link AV1200 Gigabit Powerline ethernet Adapter (Ethernet over AC wiring) (#6)
(TP-Link tpPLC utility shows typical transfer rate of 210 to 260Mbps in one install)
- TP-Link 5-port gigabit switch (#7) cabled to TP-Link AV1200
- HP EliteDesk i5-6500T with 20GB RAM, 1T m.2 SSD drive, RMS Linux RMS system (#8)
- cabled to 5-port switch
- KVM (Keyboard/Video/Mouse switch) (#9),
Keyboard/Monitor/Mouse (#10a-c)
- Primary computer, also cabled to 5-port switch (#11)

Note, in some cases the Cable Modem (#1) and wifi router (#2) may be contained in the same box. If the Linux RMS system (#8) is at a distance from the PoE switch (#3), parts #5 and #6 plus the AC wiring could be replaced by a single long Ethernet cable.

February 2023 report CAMS-BeNeLux

Carl Johannink

Am Ollenkamp 4, 48599 Gronau, Germany

c.johannink@t-online.de

A summary of the activity of the CAMS-BeNeLux-network during the month of February 2023 is presented. This month was good for a total of 12552 multi-station meteors resulting in 3543 orbits. Like previous year, most of them were collected in the last part of this month.

1 Introduction

Meteor activity in February is almost at the lowest level of the year for northern latitudes. Nevertheless, because of the long nights, results during this month can still be very good during periods with clear nights.

2 February 2023 statistics

In February the unstable poor weather continued. Mean temperatures were again fairly high, due to the lack of complete clear skies during the night. In 7 nights, we couldn't collect any single orbit which is a rather large number of completely cloudy nights. We could collect a larger number of orbits around February 7, February 14 and towards the end of the month. Statistics are compared in *Figure 1* and *Table 1*.

CAMS-BeNeLux collected 12552 multi-station meteors this month, resulting in a total of 3543 orbits, 1096 of them in the last 4 nights, or approximately 30% of the total number of orbits this month. The number of orbits derived from more than two stations was approximately 57%.

On average 96 cameras, nearly 90% of all 107 available cameras, were active during all nights this month. This number is much higher than last year. Several new cameras were added to the network recently. This month, two RMS-cameras from Kirton (*Martin Richmond-Hardy*) and Clapton (*Andy Washington*) in the eastern part of England now provide coverage on the most western parts of our network. In Hagnicourt (*Pierre-Yves Péchart*), France, two extra RMS cameras contribute their results now to our network. The more (south)eastern parts of our network got support from extra RMS cameras in Germany in Ludwigshafen (*Eduardo Fernandez del Peloso*) and Solingen (*Hartmut Leiting*). *Felix Bettonvil* (Utrecht, Netherlands) and *Koen Miskotte* (Ermelo, Netherlands) reported that their cameras became active again this month.

From all available CAMS data, higher than usual activity was detected for the February Hydrids, like in 2013 and 2018. Between solar longitude 321.9° and 327.2° a total of 29 FHY-meteors were collected. In other years this shower is nearly absent. It now looks like this stream has a 4.7-year periodicity from dust trapped in a 5:2 mean motion resonance with Jupiter (Jenniskens, 2023).

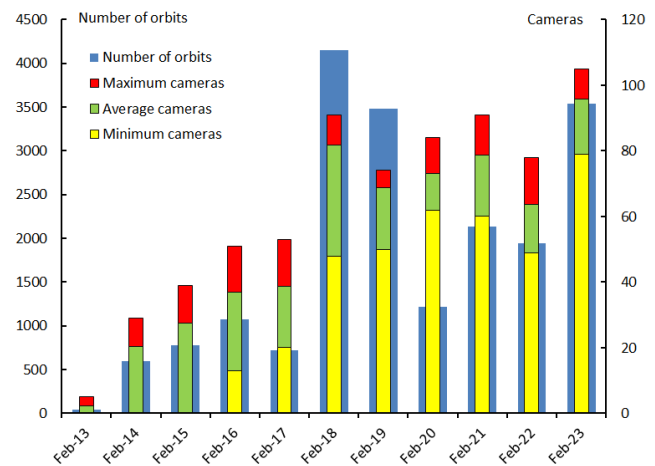


Figure 1 – Comparing February 2023 to previous months of February in the CAMS-BeNeLux history. The blue bars represent the number of orbits, the red bars the maximum number of cameras capturing in a single night, the green bars the average number of cameras capturing per night and the yellow bars the minimum number of cameras.

Table 1 – Number of orbits and active cameras in the BeNeLux during the month of February in the period 2013–2023.

Year	Nights	Orbits	Stations	Max. Cams	Min. Cams	Mean Cams
2013	9	38	6	5	–	2.3
2014	21	601	12	29	–	20.3
2015	21	777	14	39	–	27.4
2016	24	1075	17	51	13	36.9
2017	16	717	18	53	20	38.6
2018	26	4147	22	91	48	81.7
2019	24	3485	18	74	50	68.8
2020	24	1215	22	84	62	73.1
2021	25	2136	26	91	60	78.6
2022	23	1939	24	78	49	63.7
2023	21	3543	37	105	79	95.9
Total	234	19673				

3 Conclusion

The results for February 2023 are second best for this month during 11 years of CAMS-BeNeLux.

Acknowledgement

Many thanks to all participants in the CAMS-BeNeLux network for their dedicated efforts. The CAMS-BeNeLux team was operated by the following volunteers during the month of February 2023:

Hans Betlem (Woold, Netherlands, Watec 3071, 3072, 3073, 3074, 3075, 3076, 3077 and 3078), *Felix Bettonvil* (Utrecht, Netherlands, Watec 376), *Jean-Marie Biets* (Wilderen, Belgium, Watec 379, 380 and 381), *Ludger Boergerding* (Holdorf, Germany, RMS 3801), *Günther Boerjan* (Assenede, Belgium, RMS 3823), *Martin Breukers* (Hengelo, Netherlands, Watec 320, 321, 322, 323, 324, 325, 326 and 327, RMS 319, 328 and 329), *Sepp Canonaco* (Genk, RMS 3818 and 3819), *Pierre de Ponthiere* (Lesve, Belgium, RMS 3816 and 3826), *Bart Dessoy* (Zoersel, Belgium, Watec 804, 805 and 806), *Tammo Jan Dijkema* (Dwingeloo, Netherlands, RMS 3199), *Isabelle Ansseau*, *Jean-Paul Dumoulin*, *Dominique Guiot* and *Christian Wanlin* (Grapfontaine, Belgium, Watec 814 and 815, RMS 3814 and 3817), *Uwe Glässner* (Langenfeld, Germany, RMS 3800), *Luc Gobin* (Mechelen, Belgium, Watec 3890, 3891, 3892 and 3893), *Tioga Gulon* (Nancy, France, Watec 3900 and 3901), *Robert Haas* (Alphen aan de Rijn, Netherlands, Watec 3160, 3161, 3162, 3163, 3164, 3165, 3166 and 3167), *Robert Haas* (Texel, Netherlands, Watec

811), *Kees Habraken* (Kattendijke, Netherlands, RMS 3780 and 3781), *Klaas Jobse* (Oostkapelle, Netherlands, Watec 3030, 3031, 3032, 3033, 3034, 3035, 3036 and 3037), *Carl Johannink* (Gronau, Germany, Watec 3100, 3101, 3102), *Reinhard Kühn* (Flatzby, Germany, RMS 3802), *Hervé Lamy* (Dourbes, Belgium, Watec 395, RMS 3825 and 3841), *Hervé Lamy* (Humain, Belgium, RMS 3821 and 3828), *Hervé Lamy* (Ukkel, Belgium, Watec 393), *Hartmut Leiting* (Solingen, Germany, RMS 3806), *Koen Miskotte* (Ermelo, Netherlands, Watec 3051, 3052 and 3053), *Pierre-Yves Péchart* (Hagnicourt, France, RMS 3902, 3903, 3904 and 3905), *Eduardo Fernandez del Peloso* (Ludwigshafen, Germany, RMS 3805), *Tim Polfliet* (Gent, Belgium, Watec 396, RMS 3820 and 3840), *Steve Rau* (Oostende, Belgium, RMS 3822), *Steve Rau* (Zillebeke, Belgium, Watec 3850 and 3852, RMS 3851 and 3853), *Martin Richmond-Hardy* (Kirton, England, RMS 3701), *Paul and Adriana Roggemans* (Mechelen, Belgium, RMS 3830 and 3831, Watec 3832, 3833, 3834, 3835, 3836 and 3837), *Jim Rowe* (Eastbourne, Great Britain, RMS 3829), *Philippe Schaack* (Roodt-sur-Syre, Luxemburg, RMS 3952), *Hans Schremmer* (Niederkruechten, Germany, Watec 803), *Jan Thoemel* (Luxemburg, Luxemburg, Watec 3950), *Erwin van Ballegoij* (Heesh, Netherlands Watec 3148 and 3149), *Andy Washington* (Clapton, England, RMS 3702).

March 2023 report CAMS-BeNeLux

Carl Johannink

Am Ollenkamp 4, 48599 Gronau, Germany

c.johannink@t-online.de

A summary of the activity of the CAMS-BeNeLux network during the month of March 2023 is presented. This month was good for 4472 multi-station meteors resulting in 1328 orbits, a small number for the month of March.

1 Introduction

Meteor activity is now reaching the lowest level for northern latitudes in March. Contrary to 2022, this month wasn't very sunny. This resulted in a less than usual number of orbits.

2 March 2023 statistics

When we look at the mean daytime temperatures, March was very normal. But the night temperatures were nearly two degrees higher than normal.

That means we often suffered cloudy conditions at night this month. Indeed, in six nights not a single orbit was obtained from our data. In another five nights we have collected less than 10 orbits per night. Only three nights with more than 100 orbits occurred this month with as a result, a very small monthly total for our network, even for a month with low meteor activity.

CAMS-BeNeLux collected 4472 multi-station meteors this month, resulting in a total of 1328 orbits. 54% of all orbits were captured by more than two stations.

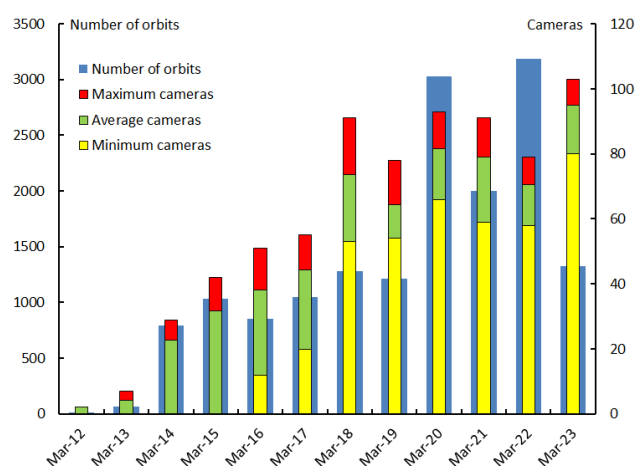


Figure 1 – Comparing March 2023 to previous months of March in the CAMS-BeNeLux history. The blue bars represent the number of orbits, the red bars the maximum number of cameras capturing in a single night, the green bars the average number of cameras capturing per night and the yellow bars the minimum number of cameras.

On average 95.0 cameras were active during the nights this month. This number is much higher than last year (70.6),

since the number of stations increased significantly in the last few months.

At least 80 cameras were active every night. This number makes it even clearer that stations were very often clouded for at least a part of the night.

Table 1 – Number of orbits and active cameras in the BeNeLux during the month of March in the period 2012–2023.

Year	Nights	Orbits	Stations	Max. Cams	Min. Cams	Mean Cams
2012	2	12	2	2	–	2.0
2013	10	69	6	7	–	4.2
2014	24	793	12	29	–	22.8
2015	23	1033	14	42	–	31.7
2016	23	856	16	51	12	38.2
2017	26	1048	19	55	20	44.4
2018	25	1280	22	91	53	73.5
2019	29	1215	20	78	54	64.4
2020	27	3026	25	93	66	81.7
2021	28	1998	27	91	59	78.9
2022	29	3189	24	79	58	70.6
2023	25	1328	37	103	80	95.0
Total	271	15847				

3 Conclusion

The results for March 2023 are rather poor compared to the results in recent years.

Acknowledgment

Many thanks to all participants in the CAMS-BeNeLux network for their dedicated efforts. The CAMS-BeNeLux team was operated by the following volunteers during the month of March 2023:

Hans Betlem (Woold, Netherlands, Watec 3071, 3072, 3073, 3074, 3075, 3076, 3077 and 3078), *Felix Bettonvil* (Utrecht, Netherlands, Watec 376), *Jean-Marie Biets* (Wilderen, Belgium, Watec 379, 380 and 381), *Ludger Boergerding* (Holdorf, Germany, RMS 3801), *Günther Boerjan* (Assenede, Belgium, RMS 3823), *Martin Breukers* (Hengelo, Netherlands, Watec 320, 321, 322, 323, 324, 325,

326 and 327, RMS 319, 328 and 329), *Sepe Canonaco* (Genk, RMS 3818 and 3819), *Pierre de Ponthiere* (Lesve, Belgium, RMS 3816 and 3826), *Bart Dessoy* (Zoersel, Belgium, Watec 804, 805 and 806), *Tammo Jan Dijkema* (Dwingeloo, Netherlands, RMS 3199), *Isabelle Ansseau*, *Jean-Paul Dumoulin*, *Dominique Guiot* and *Christian Wanlin* (Grapfontaine, Belgium, Watec 814 and 815, RMS 3814 and 3817), *Uwe Glässner* (Langenfeld, Germany, RMS 3800), *Luc Gobin* (Mechelen, Belgium, Watec 3890, 3891, 3892 and 3893), *Tioga Gulon* (Nancy, France, Watec 3900 and 3901), *Robert Haas* (Alphen aan de Rijn, Netherlands, Watec 3160, 3161, 3162, 3163, 3164, 3165, 3166 and 3167), *Robert Haas* (Texel, Netherlands, Watec 811), *Kees Habraken* (Kattendijke, Netherlands, RMS 3780 and 3781), *Klaas Jobse* (Oostkapelle, Netherlands, Watec 3030, 3031, 3032, 3033, 3034, 3035, 3036 and 3037), *Carl Johannink* (Gronau, Germany, Watec 3100, 3101, 3102), *Reinhard Kühn* (Flatzby, Germany, RMS 3802), *Hervé Lamy* (Dourbes, Belgium, Watec 395, RMS 3825 and 3841), *Hervé Lamy* (Humain, Belgium, RMS 3821 and 3828), *Hervé Lamy* (Ukkel, Belgium, Watec 393 and 817), *Hartmut Leiting* (Solingen, Germany, RMS 3806), *Koen Miskotte* (Ermelo, Netherlands, Watec 3051, 3052 and 3053), *Pierre-Yves Péchart* (Hagnicourt, France, RMS 3902, 3903, 3904 and 3905), *Eduardo Fernandez del Peloso* (Ludwigshafen, Germany, RMS 3805), *Tim Polfliet* (Gent, Belgium, Watec 396, RMS 3820 and 3840), *Steve Rau* (Oostende, Belgium, RMS 3822), *Steve Rau* (Zillebeke, Belgium, Watec 3850 and 3852, RMS 3851 and 3853), *Martin Richmond-Hardy* (Kirton, England, RMS 3701), *Paul and Adriana Roggemans* (Mechelen, Belgium, RMS 3830 and 3831, Watec 3832, 3833, 3834, 3835, 3836 and 3837), *Jim Rowe* (Eastbourne, Great Britain, RMS 3829), *Philippe Schaack* (Roodt-sur-Syre, Luxemburg, RMS 3952), *Hans Schremmer* (Niederkruechten, Germany, Watec 803), *Jan Thoemel* (Luxemburg, Luxemburg, Watec 3950), *Erwin van Ballegoij* (Heesh, Netherlands Watec 3148 and 3149), *Andy Washington* (Clapton, England, RMS 3702).

First steps of the CARMELO network (Cheap Amateur Radio Meteors Echoes LOGger)

Lorenzo Barbieri, Gaetano Brando, Paolo Fontana, and Silvana Sarto

AAB (Associazione Astrofili Bolognesi)
barbieriofiuco@gmail.com

The CARMELO network project, after a year of uninterrupted activity, proved to be reliable and gave us a glimpse of an unpredictable result: the reconstruction of meteor trajectories. After an analysis of the current situation and the models, the first results are shown, especially on simultaneous registrations. These radio recordings, compared with the optical counterpart, demonstrate how much the CARMELO instrument can be exploited for trajectory reconstruction. Finally, the construction of a “local” network linked to its own transmitter is proposed, a solution to overcome the limits imposed by the GRAVES radar.

1 Description

The CARMELO network for observing radio meteors is made up of RDS (Radio Defined Software) receivers spread throughout the country and all operating with the same standard. The characteristics of the CARMELO receiver are illustrated here⁶.

As described in the cited article, each receiver performs the fast Fourier transform on each meteor it observes, recording a file which allows the reconstruction of the radioelectric power waveform of the meteor echo.

Unlike the kind of listening for echoes carried out so far by amateur astronomers all over the world, CARMELO is not based on the audio output of an analog receiver but directly measures the radioelectric power of the meteor echo analogously to a real radar. Its operation is completely automatic, and the unique standard means that every measurement made anywhere in the world can be compared with all the other measurements made by other receivers.

The CARMELO receiver can tune into any frequency, for this purpose it is sufficient to write the value of the carrier to be listened to in the appropriate receiving station data file. The frequencies used so far are 143 MHz for receivers in Europe and 52 MHz for receivers in the USA.

The observational data produced by each individual observer is transmitted in real time to the “Astrofili a Bologna/CARMELO” server and represented with suitable diagrams. Both the presentation of single events⁷ and the hourly rates⁸ can be consulted in detail online. The past data history can be seen here⁹.

After a few years of analogue radio listening with the RAMBO system¹⁰ our conviction was that the only possible observation using meteor scatter was the investigation of

the hourly rate and this way the observation of meteor showers behavior, year by year, of both, day and nighttime.

The first results of the CARMELO network have shown us that this project can also establish the trajectories and thus, if this goal can be achieved, the meteor radiants can be determined.

To date, the network is made up of some receivers in Europe and a few in the USA¹¹, the network has been recently established and should be expanded both in number of observers willing to collaborate, and in the coverage of the territory.

2 Observations from Italy

No transmitter dedicated to listening for radio meteors is currently available in Italy. For this reason, the Italian observers use the French Graves transmitter operating as a south-facing radar transmitter on the 143 MHz frequency (Figure 1).



Figure 1 – The French Graves transmitter operating as a south-facing radar transmitter.

⁶ http://www.astrofiliabologna.it/static/file/carmelo/2022_emn.pdf

⁷ <http://www.astrofiliabologna.it/graficocarmelo>

⁸ <http://www.astrofiliabologna.it/graficocarmelohr>

⁹ http://www.astrofiliabologna.it/carmelo_archive

¹⁰ <http://www.astrofiliabologna.it/rambo>

¹¹ http://www.astrofiliabologna.it/obs_on_line

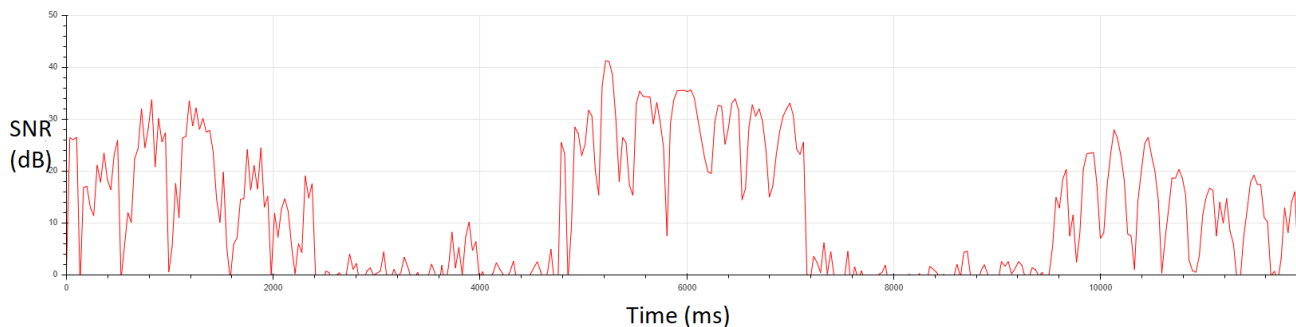


Figure 2 – A strong meteor echo with a long duration. The transmitter sweeping behaviour is clearly visible.

As will be described later, this solution involves some limits which penalize listening, making the interpretation of the results more complicated. The average distance between this transmitter and the receivers located in Italy exceeds 500 km.

The wave transmitted by Graves sweeps southern Europe at a fixed frequency generating an alternating presence and absence of the radioelectric signal clearly visible in the plot in Figure 2. This means that for at least 50% of the time the transmission is not present and therefore at least half of the meteor radio echoes are lost. Furthermore, the sweeping of the radar can lead to the fact that a meteor trail gets the signal only after its appearance, or vice versa, so that its echo disappears from the reception before its dissolution.

Another feature of Graves is the fact that it transmits on a too high frequency, at least three times the frequency normally used to listen for meteor radio echoes. The evidence for this limit is shown by comparing the American data with the Italian data. If the hourly rates are compared, it can be seen that the number of meteors received per observer in the USA is at least three times larger than that in Italy (Figure 3).

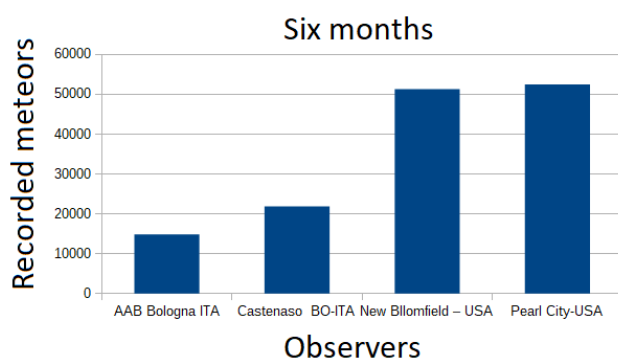


Figure 3 – Comparison between 50 Mhz and 143 Mhz receiving systems.

It should be noted that the transmitter used in the USA is a television transmitter, i.e., a broadcaster which in all probability uses antennas with a flat radiation lobe, aimed essentially at ground reception and certainly not aimed at the sky, nevertheless the efficiency of the reception on this frequency is evident.

Hence the need to create a transmitter on 50Mhz with upward transmission in Italy too, similarly to what has already been done in Belgium, Japan and recently also in Great Britain.

While waiting for this solution, it would be interesting to test the CARMELO system also in some of these countries for a first comparison with the Italian data which we illustrate in the next section.

3 First results

The CARMELO system allows the creation of a database in which all the data related to each single reception are automatically recorded, in addition to the data relating to each single receiver. The information in this database include location, latitude, longitude, Tx frequency, noise floor (dB), antenna, gain (dB), sampling duration (ms), meteor duration (ms), max power (snr), angle of view covered by the antenna ($^{\circ}$), identifying sign of the receiving station, identifying color of the receiving station and instant of meteor beginning (in milliseconds).

Querying this database allows statistical analysis and comparisons with observations made in different ways, for example visual observations, and this has allowed us to compare our data with the Global Meteor Network (GMN) database based on the automatic observation of meteors using video cameras.

Each single recording allows us to analyze the waveforms with graphic representation of both amplitude (signal to noise ratio of the received electromagnetic field) and the frequency (Figure 4). It is also possible to superimpose receptions of the same meteor by different observers. An initial evaluation of CARMELO's potential can be obtained from the representation of the waveform generated by a fireball with a duration of several seconds (Figure 2) which shows the sweeping frequency of the Graves transmitter.

As mentioned, CARMELO performs the fast Fourier transformation for each sampling performed; the duration of each sample varies from 30 to 33 milliseconds. The temporal resolution of the system is therefore equal to this value and the system exclusively observes overdense meteors, due to the fact that underdense meteors have a

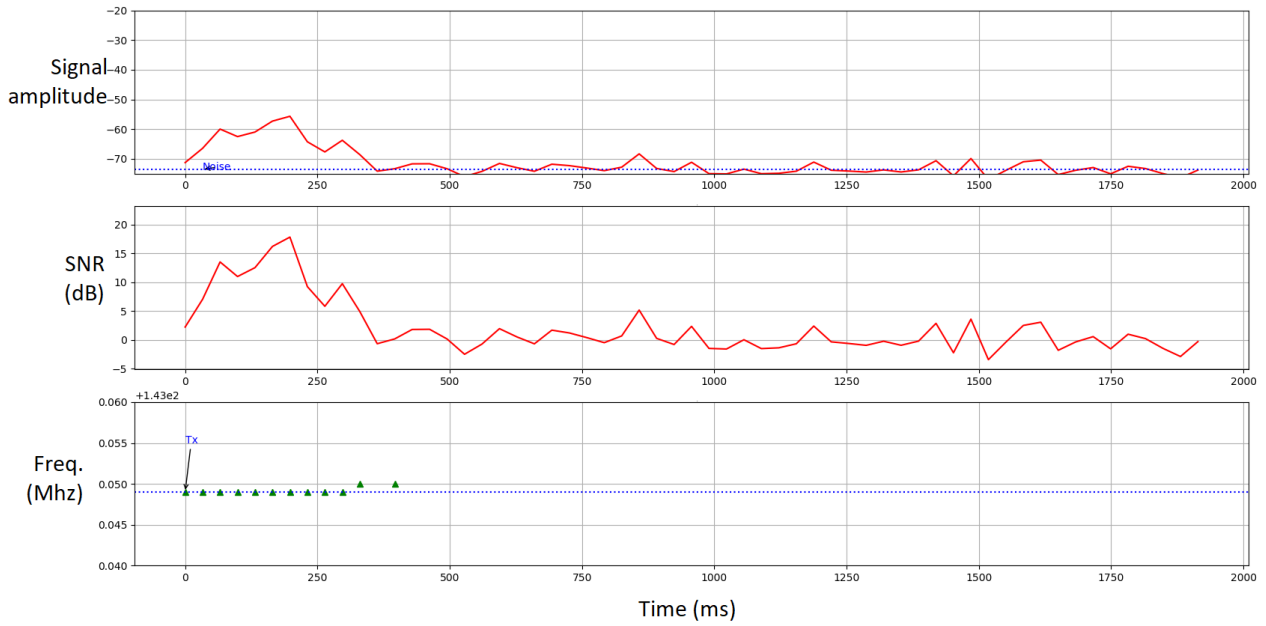


Figure 4 – Graphical representation of a CARMELO recording. Note in the third graph that, when the meteor echo ends (SNR goes to zero) the frequency (random) of the noise always falls off the scale.

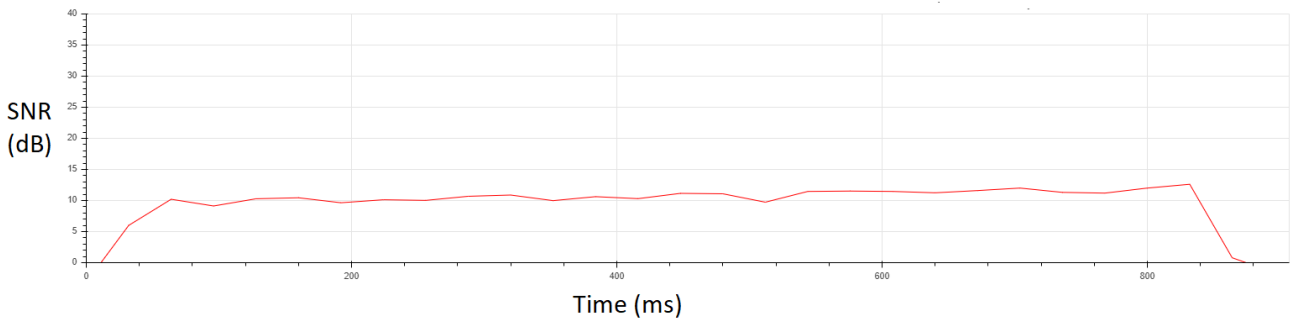


Figure 5 – Meteor event recorded on 2022 October 19 at 11^h47^m01^s UTC by observer San Giovanni in Persiceto BO, Italy.

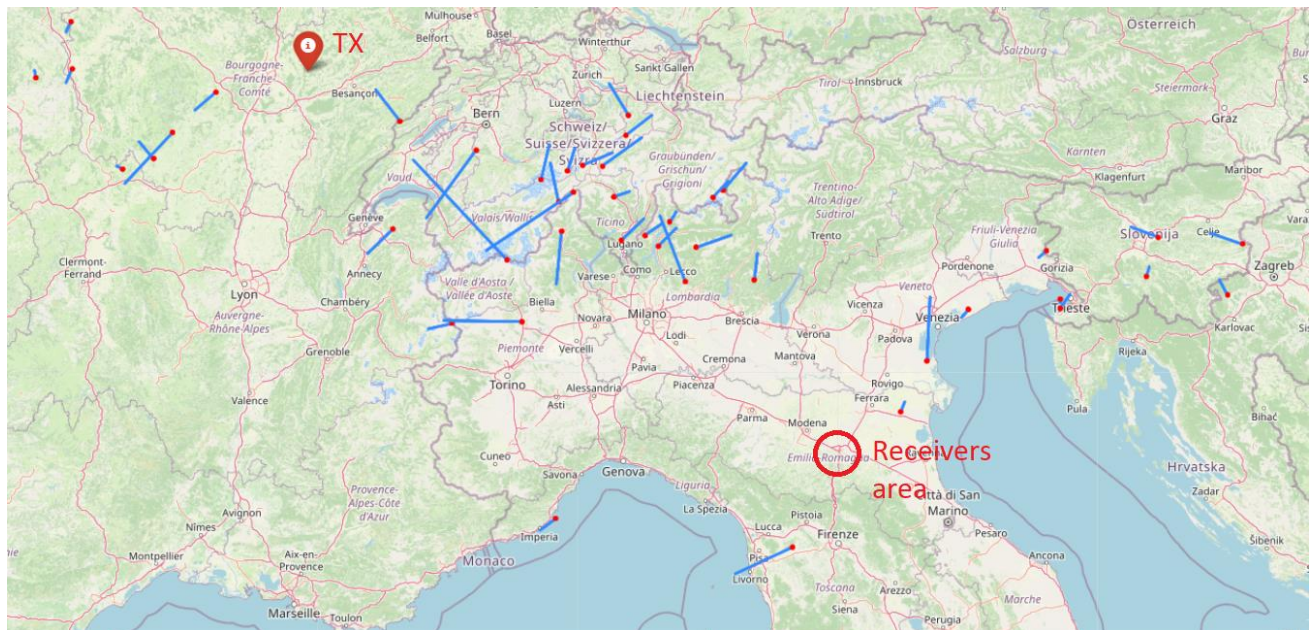


Figure 6 – A few dozen meteors recorded by CARMELO projected on the ground of the corresponding optical counterparts? The blue segments indicate the direction, the red dots are the beginning of the meteors.

duration shorter than the sampling time (*Figure 5*). This makes it more suitable for observing meteor showers and less suitable for observing sporadic meteors.

The meteors recorded in the first months of the CARMELO network in Italy show that we observe an extremely wide field of view (*Figure 6*). The trajectories of the observed meteors are scattered in all directions. The transmitter and receivers are located at a great distance (on average 550 km), the transmitter has radiating panels which cover a beam between 15 and 40 degrees of elevation, and the receiving antennas also have an elevation of about 30°. For these reasons the majority of the positions of the meteors are located between the transmitter and the receivers, but in some cases, it is possible to see them north of the transmitter or south of the receivers.

4 Theoretical considerations

The physics of radio meteors teach us that the reflection of radio waves in the meteor trail is specular, i.e.: the necessary condition for receiving an echo is that the angle of incidence is equal to that of reflection (*Figure 7*).

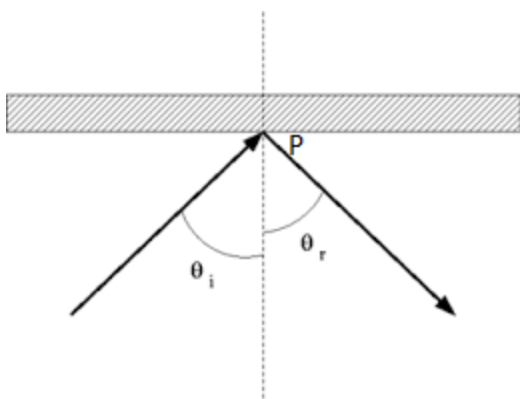


Figure 7 – Reflection of a ray of light on a mirror: the angle of incidence is equal to that of the reflection.

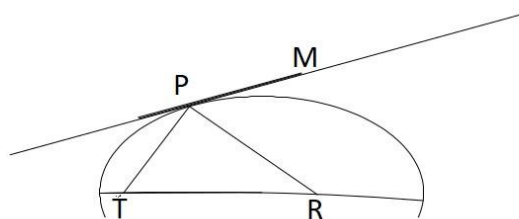


Figure 8 – Meteor tangent to the ellipsoid. T and R are in the foci.

In *Figure 8* the receiver R sees the transmitter T only in one point of the mirror, as a consequence the observed signal comes from a restricted area on the meteor trail. We can approximate this area as a point, which we will call P .

Its position in space depends only on the geometry of the specular reflection. In *Figure 8* the point P is identified geometrically as the one in which the path between the transmitter and the receiver is shorter. (Wislez, 2005). It lies on an ellipsoid which foci consist of transmitter T and

receiver R , and the path of the meteor is tangent to this ellipsoid.

It should be noted that this point does not necessarily coincide with the point, which we will call M , in which the meteor “lights up”, the beginning point where it becomes visible for the visual observer.

A second receiver R_1 , placed at a different position, if it also receives the meteor echo of the same meteor, will receive it coming from a different point on the same path that we will call P_1 in which the track of the meteor is also tangent to a second ellipsoid with foci T and R_1 , see *Figure 9*.

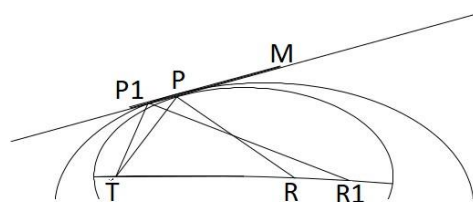


Figure 9 – Meteor tangent to the two ellipsoids. T , R and R_1 are in the foci.

In the case of relatively short distances between the two receivers, the two ellipsoids differ slightly. The meteor moves along the trajectory with a high velocity reaching the points P and P_1 at different times which we can call T and T_1 .

5 Simultaneous receptions

The Graves transmitter transmits an unmodulated continuous carrier, therefore, in reception, there are no impulses that allow us to detect the delays due to the different path taken by the reflected signal. This means that the temporal evaluation must be carried out exclusively on the delay times due to the movement of the meteor in the atmosphere.

As mentioned before, the system records data accurate to a millisecond, even if the time resolution of each single sampling requires us to consider a ΔT of plus or minus 15 ms. Synchronization between the receivers is carried out via the NTP (Network Time Protocol)¹² system capable of guaranteeing an accuracy of less than 10 ms and therefore less than the time resolution of CARMELO.

Nonetheless we carried out a field test by measuring “artificial” meteors, i.e., generated by a portable radio transmitter with three different receivers placed a few kilometers away. The result was that 100% of the signal receiving times were identical plus or minus 15 ms ΔT .

With receivers placed in a radius of between 10 and 40 km, most of the meteors are received simultaneously by two or more receivers. We therefore set ourselves the goal of

¹² https://en.wikipedia.org/wiki/Network_Time_Protocol

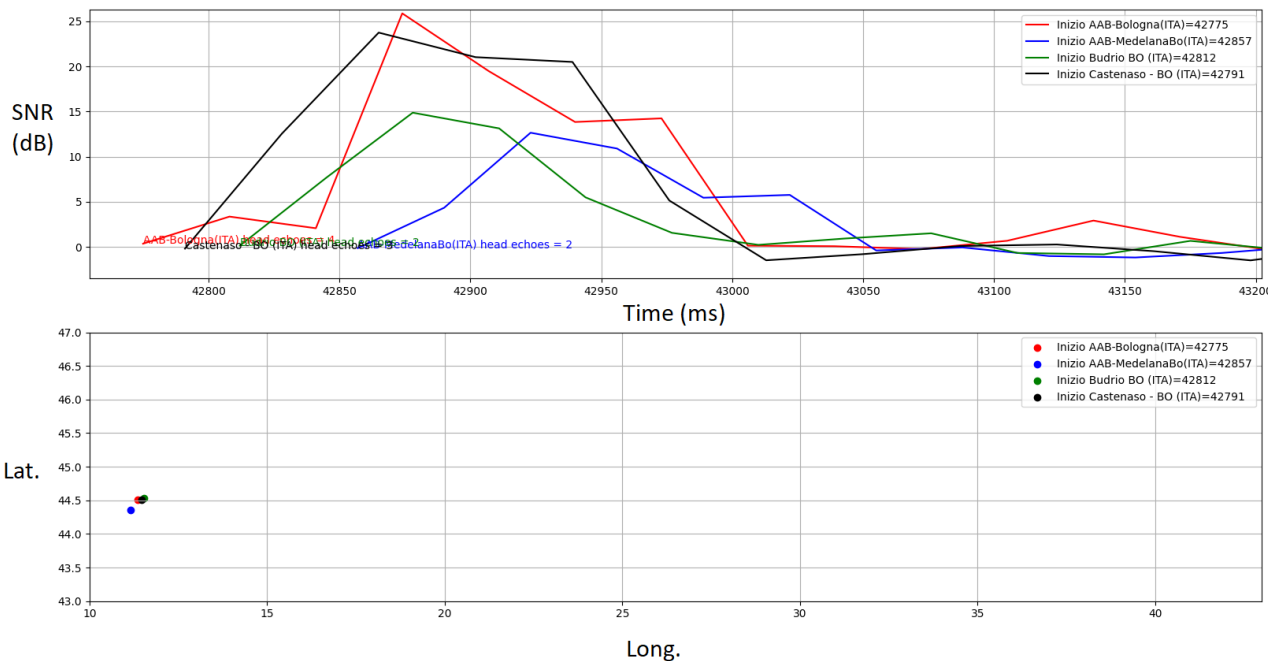


Figure 10 – In the upper part: superposition of four simultaneous receptions, in the lower part: geographical location of the receivers.

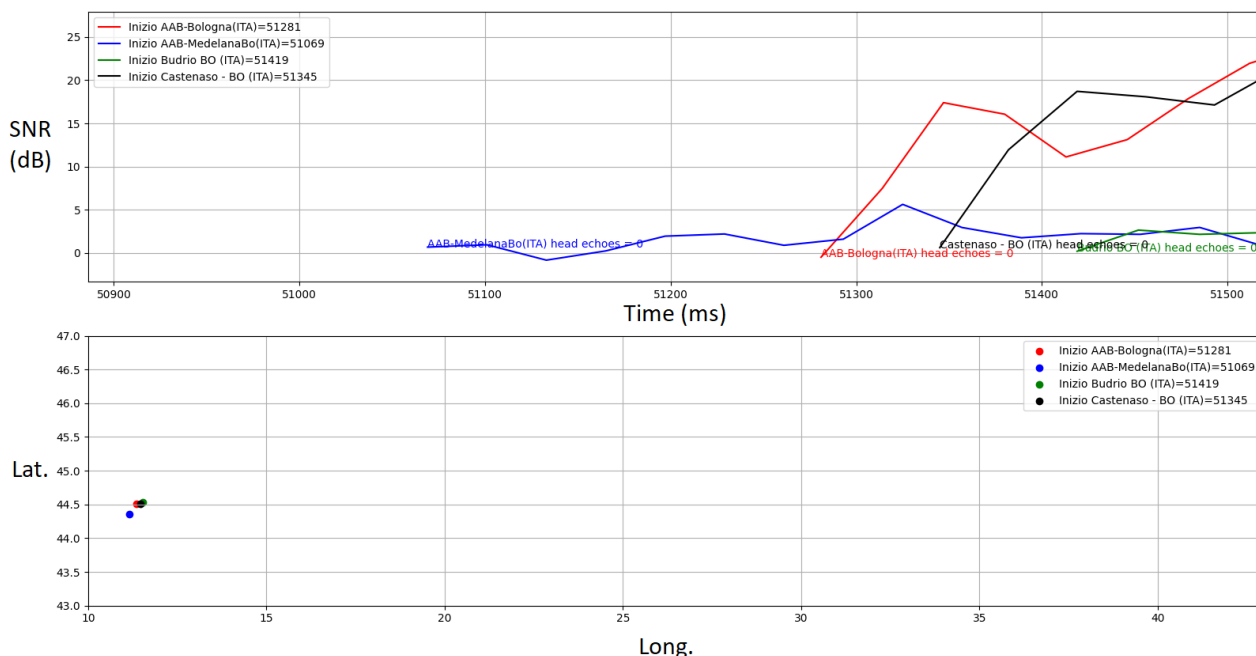


Figure 11 – Sometimes not all the waveforms have the same shape.

comparing these observations in search of clues that lead us to identify the orientation, direction and position of the meteor’s path. Each CARMELO receiver records, to the millisecond, the meteor start time, from now on: $T(im)$; this measurement is the instant following the first two samplings in which the fast Fourier transformation detects the frequency of the carrier for two consecutive times with an amplitude in which the signal-to-noise ratio (S/N) exceeds the pre-set threshold.

In simultaneous receptions, the meteor starting time $T(im)$ varies between one and the other reception in a range from zero to half a second. In the stacked image of the waveforms of the simultaneous recordings it is sometimes noted how

the curves, although very similar, present differences, see *Figure 11*.

The first cause of these differences concerns the antenna gain: not all antennas are identical and not all have the same pointing or the same height from the ground. First of all, all this entails a different amplitude in the signal-to-noise ratio (S/N) but this can also cause a delay in the identification of the first instant $T(im)$.

In some meteors an increasing front can be clearly seen, in others this is less visible. This way, the question arises how to choose which is the instant to be considered as the instant in which the meteor reaches point P , i.e., if the instant $T(im)$ measured automatically by the CARMELO system or the instant in which the ascending of the wave front begins.

For this experience we have chosen the first hypothesis. We have taken the Italian recordings in a period from July to November 2022 into consideration by isolating all the radio meteors received simultaneously by at least three receivers. In this way it is possible to compare the start timings of receivers placed scattered over the area and therefore able to have, at least in 2D projection an infinity of combinations of possible time sequences.

Comparing the meteor start times of each single recording with the geographic position of the observers on the territory, we first of all noticed how it was almost always possible to highlight a coherence between the times and the positions. For instance, the delay times between the observers, even in the 2D approximation in projection on the ground, were arranged in a time sequence consistent with the arrangement of the receivers and these appeared almost never random.

We therefore tried to assume, for each meteor, the projection of its path onto the ground based on the delay times between one and the other. Obviously, this procedure, also based on a Python script, involves a great approximation, the greater the approximation the smaller the number of observers.

Although approximate, this method has allowed us to identify a hypothesis for the projection on the ground of which we only know the direction and orientation while we know nothing about the position. These direction and orientation hypotheses then had to be verified with visual observation. To do this it is necessary to compare the radio data with those recorded by the video cameras dedicated by astronomers and amateur astronomers to the night observation of the meteors. Our choice fell on the GMN (Global Meteor Network) database¹³.

We know that the time in which the first luminous trace appears in the sky does not always coincide with the time in which the first reflected radio signal reaches a receiver.

From *Figure 9* and from the previous paragraph it is possible to notice how the two points *P* and *M* can differ, and consequently also the corresponding timings. For the purpose of this research, this consideration is not particularly interesting and therefore we have decided to define as the optical counterparts, all those meteors of the GMN database having the starting time coinciding with those of CARMELO within a range of one second.

However, this procedure has a drawback. The temporal coincidence between the two databases does not ensure that we cannot be dealing with two different meteors, which took place at the same moment, but which are located in different areas. This uncertainty may have contaminated our comparison, albeit with a low probability.

We compared the timings of the start of the meteor calculated in the CARMELO and GMN databases with a Python script, setting as a condition, in addition to the

temporary one, also the geographical limits of central Europe. The outcome of this comparison identified 46 events.

In these 46 events, 15 meteors had insufficient radio observations to be able to define a trajectory hypothesis, either because the delay times were close to zero, or because the waveforms were too different from each other.

In the remaining 31 cases we were able to define a trajectory hypothesis, at this point we were able to compare it with the ground projections of the meteors recorded by GMN¹⁴.

We have defined those having roughly the same direction (more or less about thirty degrees) and the same orientation as coherent” and as inconsistent those in which one or none of these conditions was met. The result was 25 “coherent” meteors, equal to 84% and 5 “inconsistent”, equal to 16%.

6 Reception with greater distances

New observers joining the CARMELO network, placed at greater distances than those examined in the previous test confirmed that even for distances of a few hundred kilometers the differences in arrival times increase as the distance increases, while remaining consistent in timeline with a straight path.

7 Final considerations and future developments

The observations illustrated here constitute a first exclusively qualitative result, but we would like to highlight how, despite all the limitations described in the second paragraph, the possibility of exploiting the CARMELO system for the automatic identification of the direction of the meteors emerges, the first step in a search for radiants.

To further explore this path, however, it is necessary to get rid from the limits imposed by listening for the Graves transmitter signal. It is necessary to build a network of observatories spread over the territory with antennas pointing vertically in an area of some tens of kilometers around a transmitter operating on 50 MHz with vertical irradiation and circular polarization. Alternatively, it is necessary to experiment with this technique where such a network already exists.

For this reason, the availability and contribution of scientific organizations and individual amateurs to expand the network remains a crucial necessity.

References

Wislez J.-M. (2005). “Meteor astronomy using a forward scatter set-up”. *Proceedings of the Radio Meteor School*, pages 85–106.

¹³ https://en.wikipedia.org/wiki/Network_Time_Protocol

¹⁴ <https://globalmeteornetwork.org/>

Radio meteors February 2023

Felix Verbelen

Vereniging voor Sterrenkunde & Volkssterrenwacht MIRA, Grimbergen, Belgium

felix.verbelen@skynet.be

An overview of the radio observations during February 2023 is given.

1 Introduction

The graphs show both the daily totals (*Figure 1 and 2*) and the hourly numbers (*Figure 3 and 4*) of “all” reflections counted automatically, and of manually counted “overdense” reflections, overdense reflections longer than 10 seconds and longer than 1 minute, as observed here at Kampenhout (BE) on the frequency of our VVS-beacon (49.99 MHz) during the month of February 2023.

The hourly numbers, for echoes shorter than 1 minute, are weighted averages derived from:

$$N(h) = \frac{n(h-1)}{4} + \frac{n(h)}{2} + \frac{n(h+1)}{4}$$

No lightning activity was observed and local interference and unidentified noise remained low during this month, with however almost every day weak to very strong brief periods of solar noise (*Figures 5 and 6*), which are of course very interesting as such.

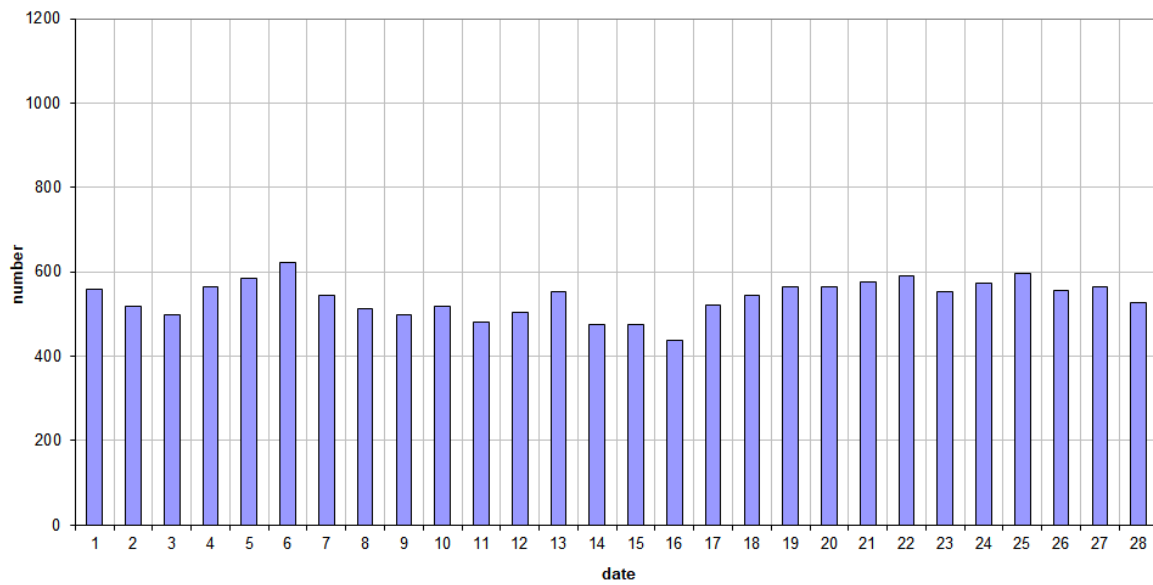
During this month there were, as expected, no strong or eye-catching meteor showers, but closer examination of the data - in particular the overdense - reveals a number of weak showers.

Over the entire month, 6 reflections longer than 1 minute were observed here. A selection of long reflections is shown in *Figures 7 to 14*.

In addition to the usual graphs, you will also find the raw counts in cvs-format¹⁵ from which the graphs are derived. The table contains the following columns: day of the month, hour of the day, day + decimals, solar longitude (epoch J2000), counts of “all” reflections, overdense reflections, reflections longer than 10 seconds and reflections longer than 1 minute, the numbers being the observed reflections of the past hour.

¹⁵ https://www.meteornews.net/wp-content/uploads/2023/03/202302_49990_FV_rawcounts.csv

49.99MHz - RadioMeteors February 2023
daily totals of "all" reflections *(automatic count_Mettel5_7Hz)*
Felix Verbelen (Kamphenhout)



49.99MHz - RadioMeteors February 2023
daily totals of all overdense reflections
Felix Verbelen (Kamphenhout)

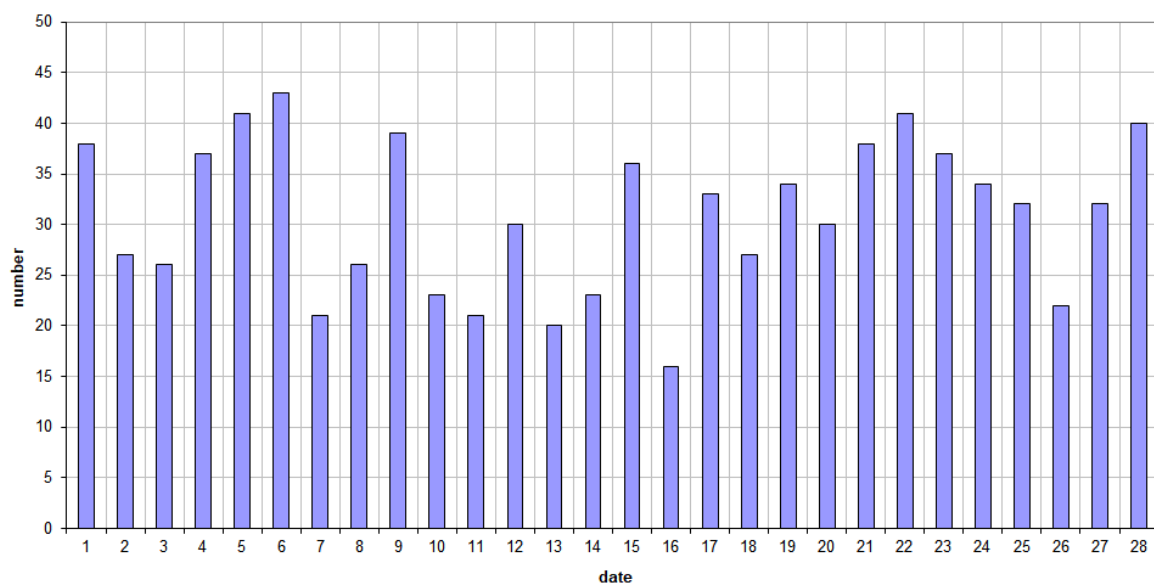
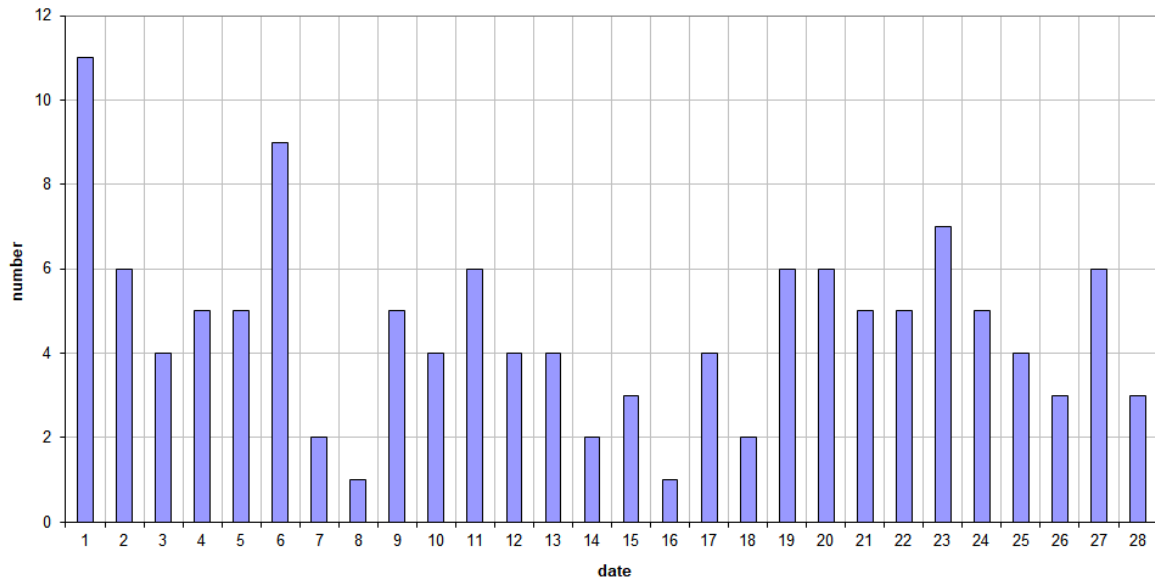


Figure 1 – The daily totals of “all” reflections counted automatically, and of manually counted “overdense” reflections, as observed here at Kamphenhout (BE) on the frequency of our VVS-beacon (49.99 MHz) during February 2023.

49.99MHz - RadioMeteors February 2023
daily totals of reflections longer than 10 seconds
Felix Verbelen (Kamphenhout)



49.99MHz - RadioMeteors February 2023
daily totals of reflections longer than 1 minute
Felix Verbelen (Kamphenhout)

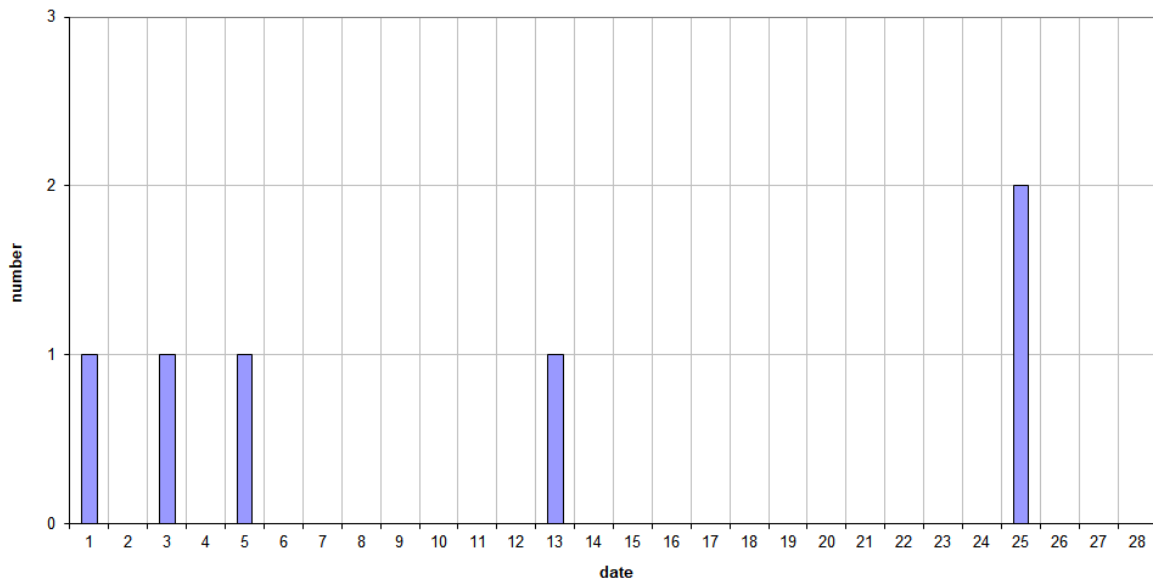


Figure 2 – The daily totals of overdense reflections longer than 10 seconds and longer than 1 minute, as observed here at Kamphenhout (BE) on the frequency of our VVS-beacon (49.99 MHz) during February 2023.

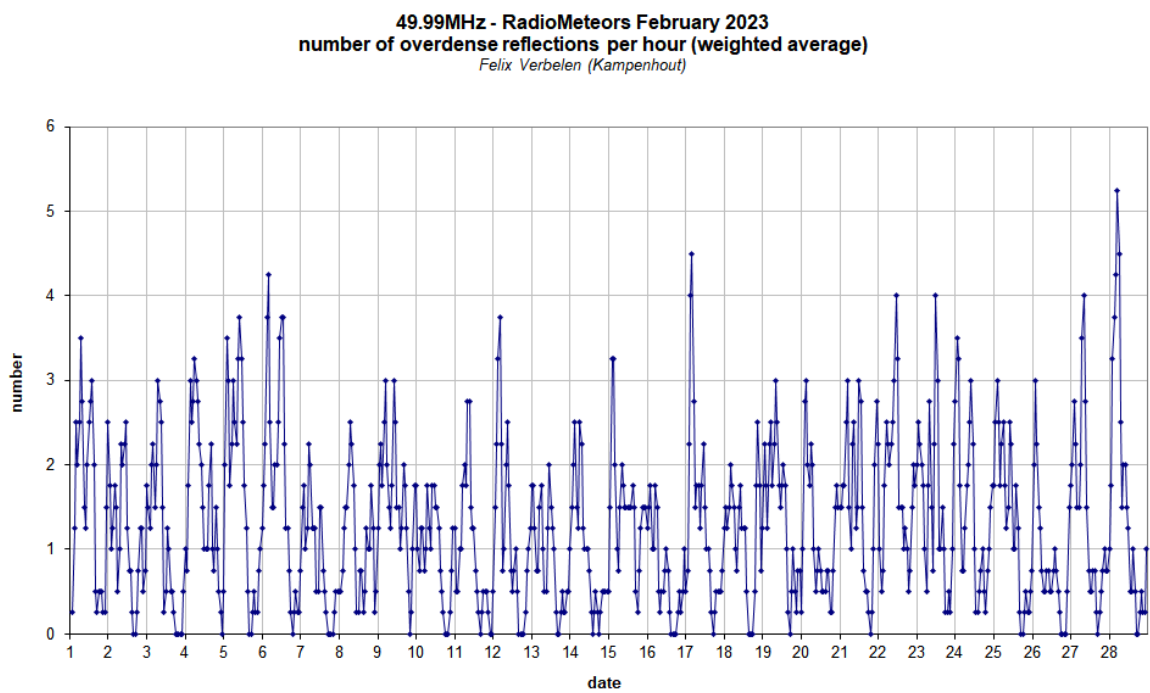
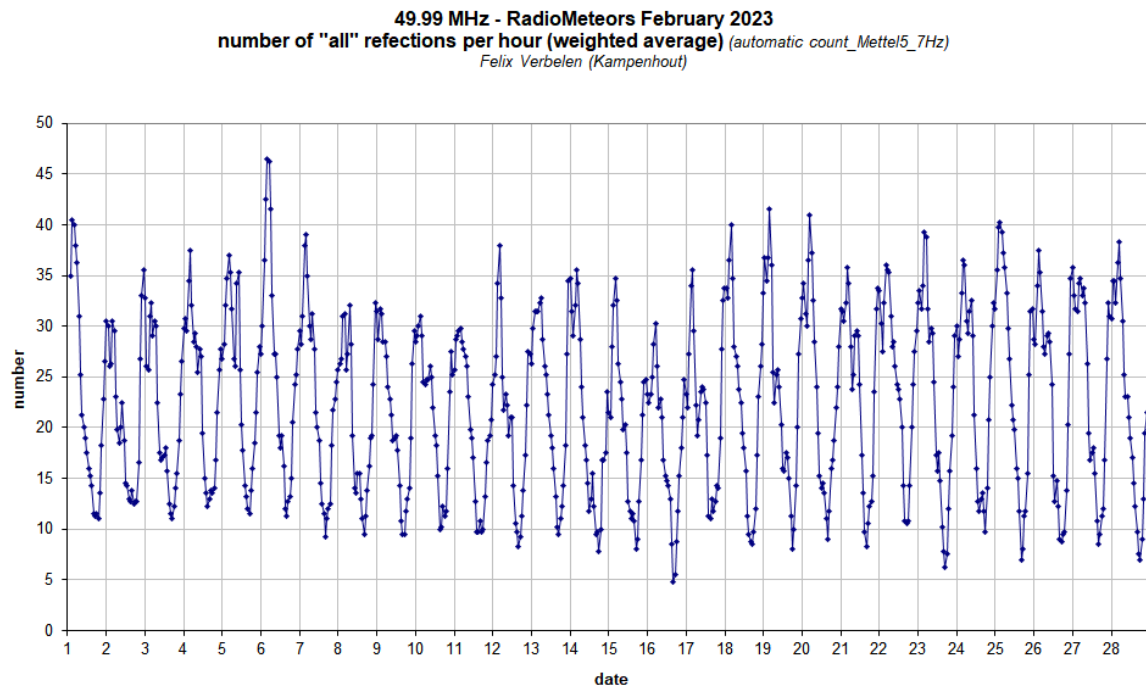
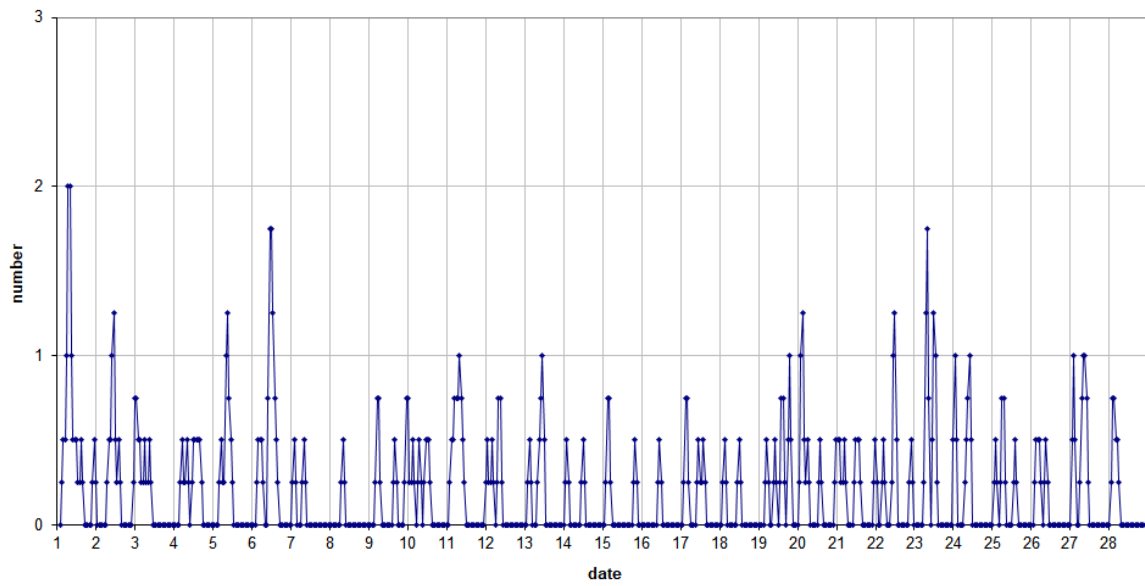


Figure 3 – The hourly numbers of “all” reflections counted automatically, and of manually counted “overdense” reflections, as observed here at Kampenhout (BE) on the frequency of our VVS-beacon (49.99 MHz) during February 2023.

49.99MHz - RadioMeteors February 2023
number of reflections >10 seconds per hour (weighted average)
Felix Verbelen (Kampenhout)



49.99MHz - RadioMeteors February 2023
hourly totals of overdense reflections longer than 1 minute
Felix Verbelen (Kampenhout/BE)

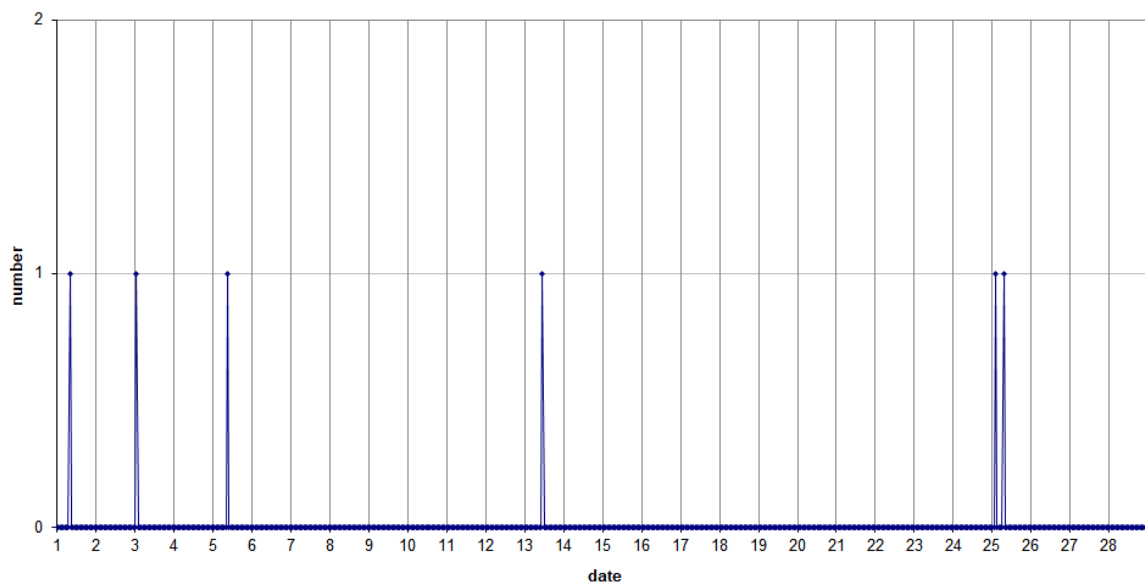


Figure 4 – The hourly numbers of overdense reflections longer than 10 seconds and longer than 1 minute, as observed here at Kampenhout (BE) on the frequency of our VVS-beacon (49.99 MHz) during February 2023.



Figure 5 – Strong brief period of solar noise 21 February.

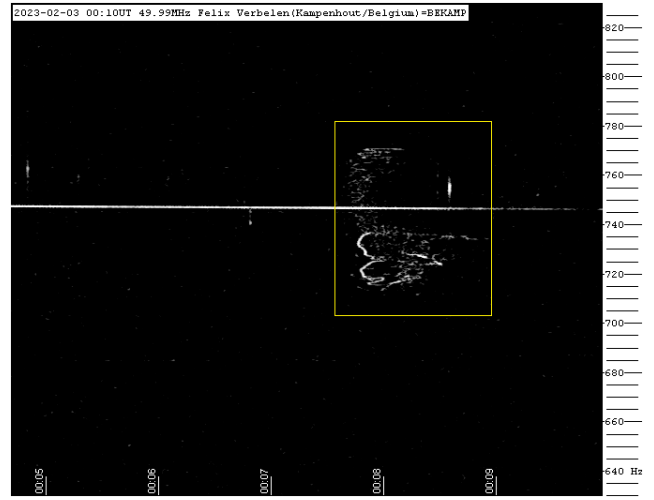


Figure 8 – Meteor echo 3 February 2023, 0^h10^m UT.

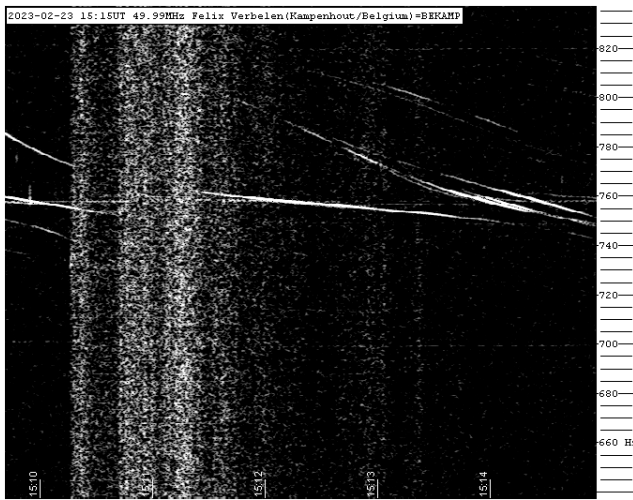


Figure 6 – Strong brief period of solar noise 23 February.

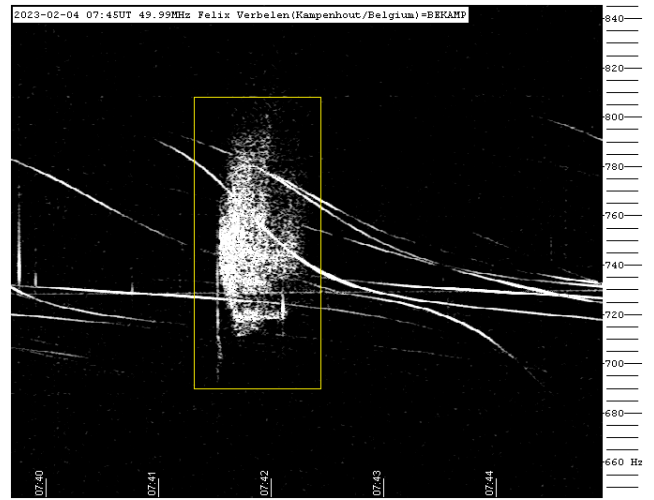


Figure 9 – Meteor echo 4 February 2023, 7^h45^m UT.

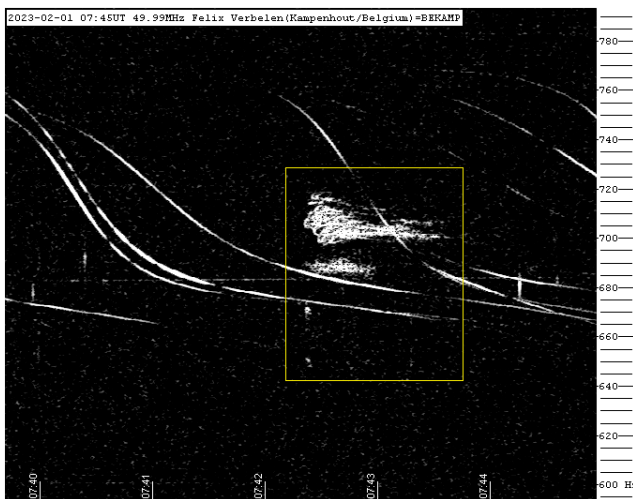


Figure 7 – Meteor echo 1 February 2023, 7^h45^m UT.

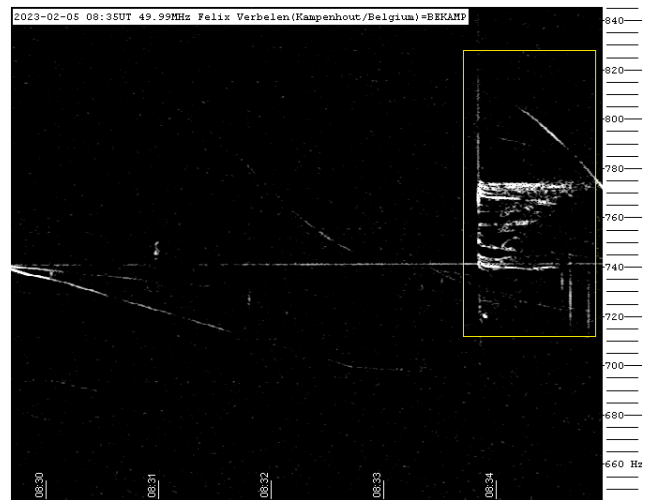


Figure 10 – Meteor echo 5 February 2023, 8^h35^m UT.

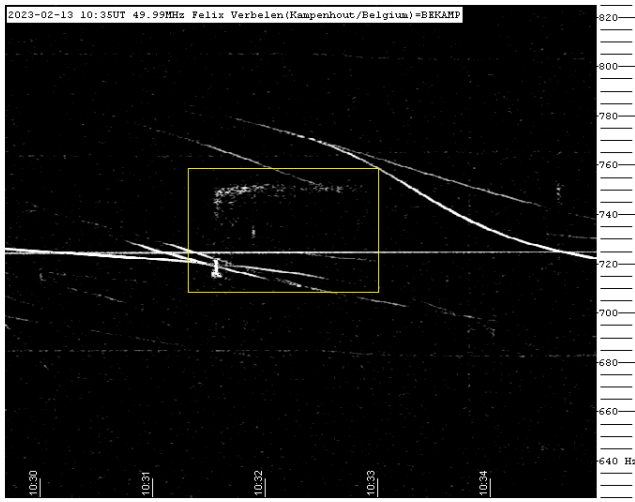


Figure 11 – Meteor echo 13 February 2023, 10^h35^m UT.

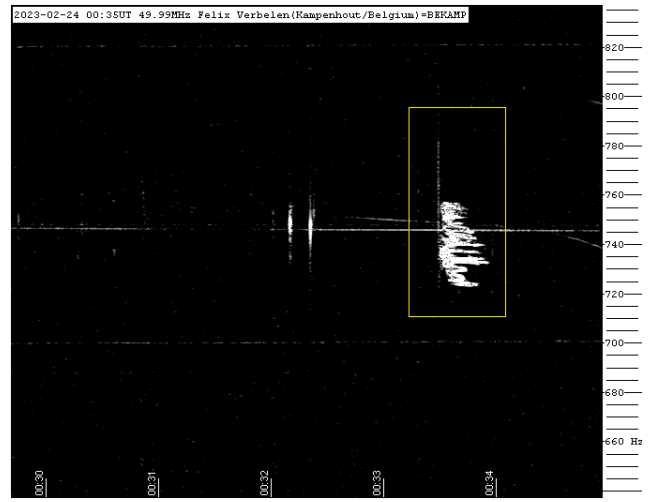


Figure 14 – Meteor echo 24 February 2023, 0^h35^m UT.

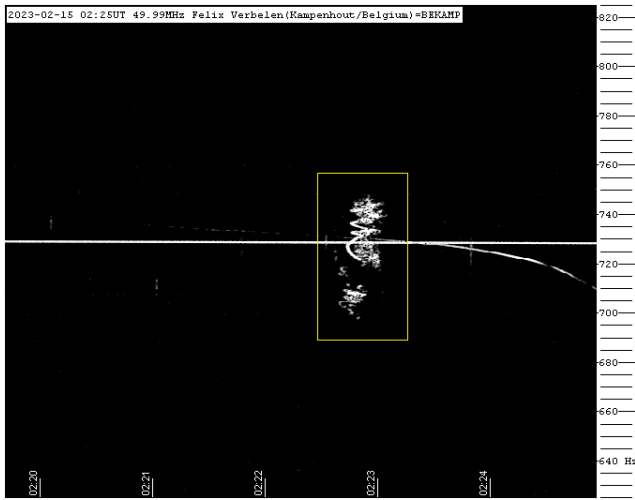


Figure 12 – Meteor echo 15 February 2023, 2^h25^m UT.

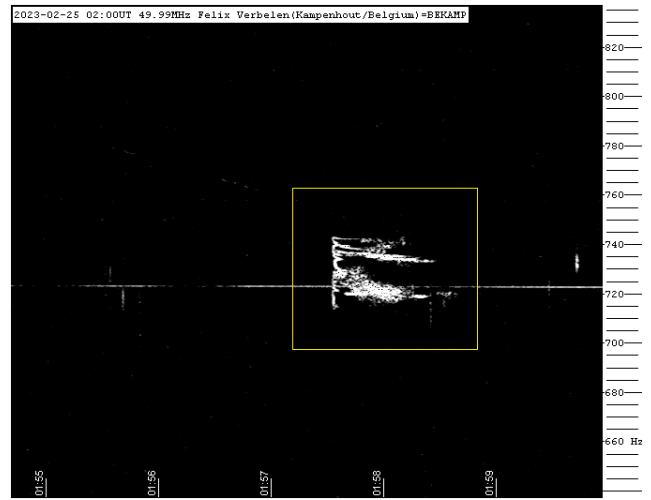


Figure 15 – Meteor echo 25 February 2023, 2^h00^m UT.

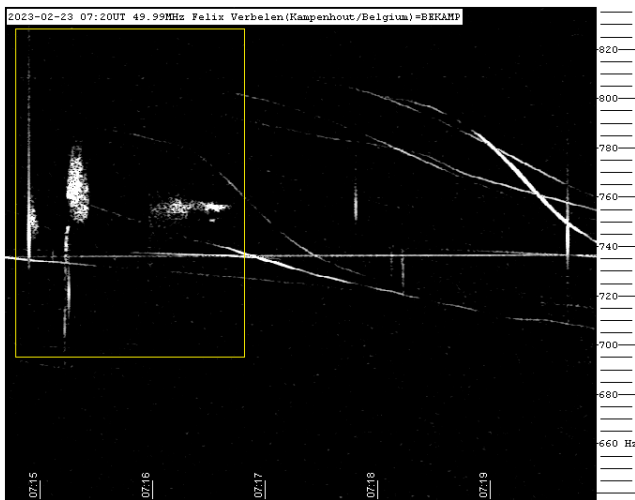


Figure 13 – Meteor echo 23 February 2023, 7^h20^m UT.

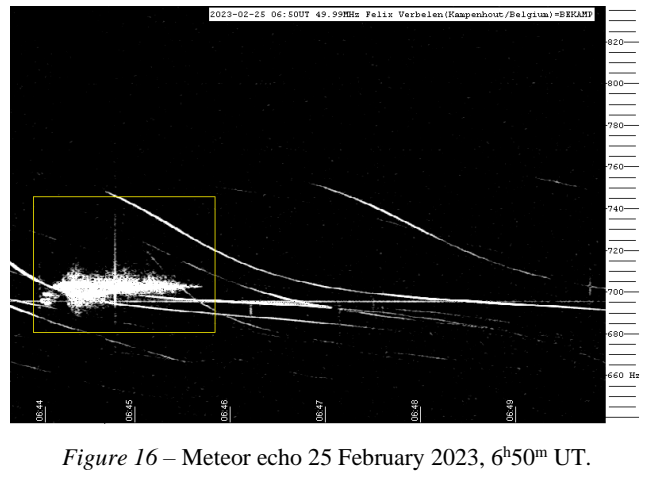


Figure 16 – Meteor echo 25 February 2023, 6^h50^m UT.

Radio meteors March 2023

Felix Verbelen

Vereniging voor Sterrenkunde & Volkssterrenwacht MIRA, Grimbergen, Belgium

felix.verbelen@skynet.be

An overview of the radio observations during March 2023 is given.

1 Introduction

The graphs show both the daily totals (*Figure 1 and 2*) and the hourly numbers (*Figure 3 and 4*) of “all” reflections counted automatically, and of manually counted “overdense” reflections, overdense reflections longer than 10 seconds and longer than 1 minute, as observed here at Kampenhout (BE) on the frequency of our VVS-beacon (49.99 MHz) during the month of March 2023.

The hourly numbers, for echoes shorter than 1 minute, are weighted averages derived from:

$$N(h) = \frac{n(h-1)}{4} + \frac{n(h)}{2} + \frac{n(h+1)}{4}$$

Weak to moderate lightning activity was recorded on just 3 days, while local interference and unidentified noise remained low this month. Solar noise was also rather limited, with nonetheless a few fairly strong outbursts like the one on March 4 (*Figure 5*).

Meteor activity reached its annual minimum this month as expected, with no strong or prominent meteor showers, but a closer look at the data reveals some fainter showers.

Over the entire month, 4 reflections longer than 1 minute were observed. A selection of these, along with some interesting “epsilons” are included (*Figures 6 to 20*). Many more are available on request.

The number of measurable head reflections remained fairly limited, but two examples are attached (*Figures 21 and 22*).

While the x -axis of the SpecLab images is 5 minutes, with the zoomed head reflection it is only 2 seconds. Measurement of the slope of these head reflections give velocities of resp. 59 km/s (20230309_0119 UT) and 45 km/s (20230331_1456 UT). For the calculation used, the method has been described a few years ago (Verbelen, 2019). Over the entire month, 6 reflections longer than 1 minute were observed here. A selection of long reflections is shown in *Figures 9 to 16*.

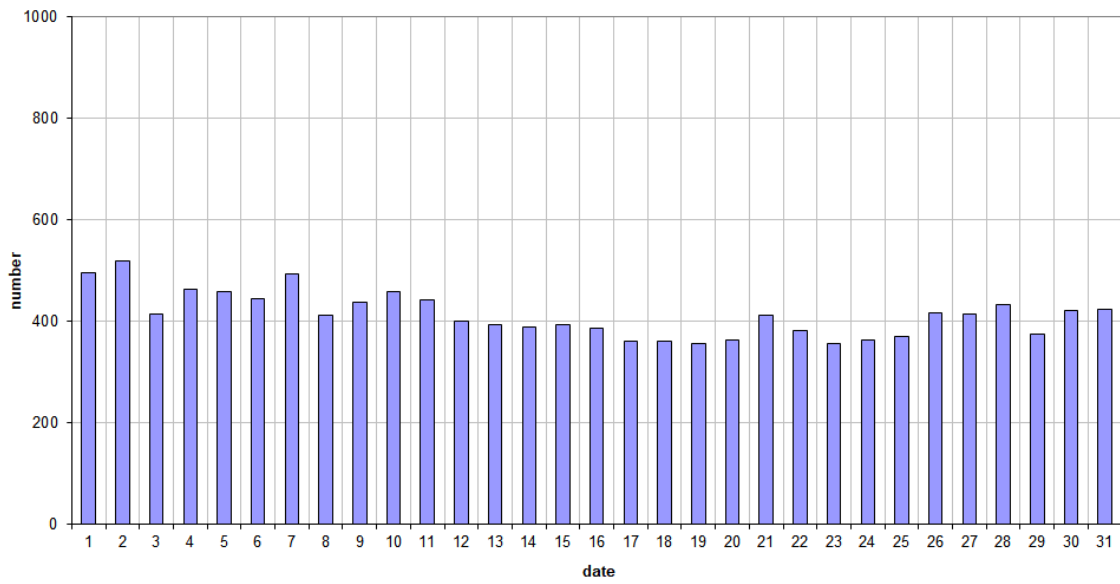
In addition to the usual graphs, you will also find the raw counts in cvs-format¹⁶ from which the graphs are derived. The table contains the following columns: day of the month, hour of the day, day + decimals, solar longitude (epoch J2000), counts of “all” reflections, overdense reflections, reflections longer than 10 seconds and reflections longer than 1 minute, the numbers being the observed reflections of the past hour.

References

Verbelen F. (2019). “Meteor velocity derived from head echoes obtained by a single observer using forward scatter from a low powered beacon”. *WGN, Journal of the International Meteor Organization*, **47**, 49–54.

¹⁶https://www.meteornews.net/wp-content/uploads/2023/04/202303_49990_FV_rawcounts.csv

49.99MHz - RadioMeteors March 2023
daily totals of "all" reflections (automatic count_Mettel5_7Hz)
Felix Verbelen (Kamphenhout)



49.99MHz - RadioMeteors March 2023
daily totals of all overdense reflections
Felix Verbelen (Kamphenhout)

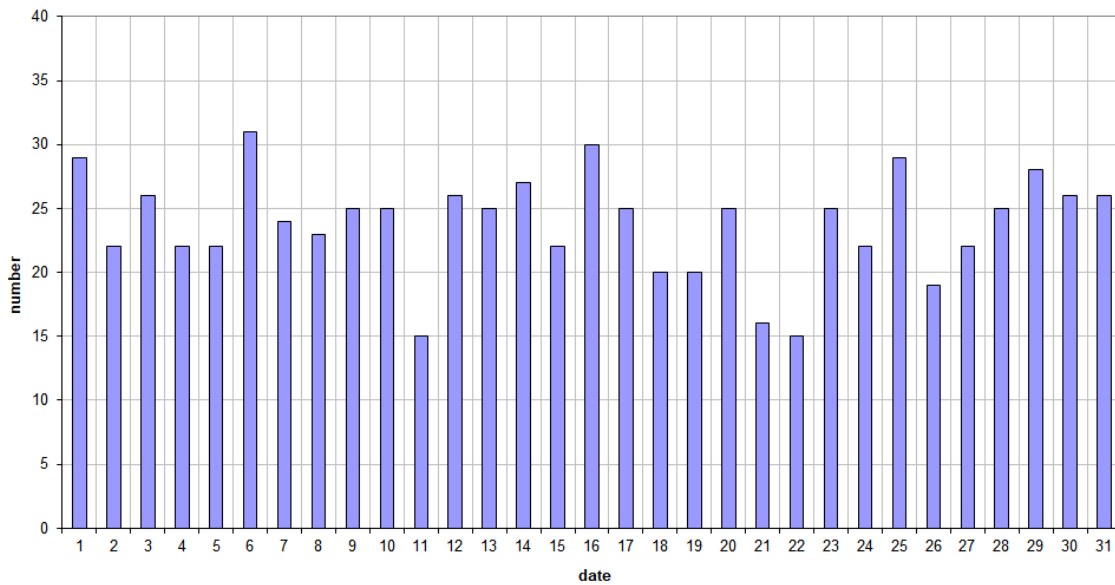


Figure 1 – The daily totals of “all” reflections counted automatically, and of manually counted “overdense” reflections, as observed here at Kamphenhout (BE) on the frequency of our VVS-beacon (49.99 MHz) during March 2023.

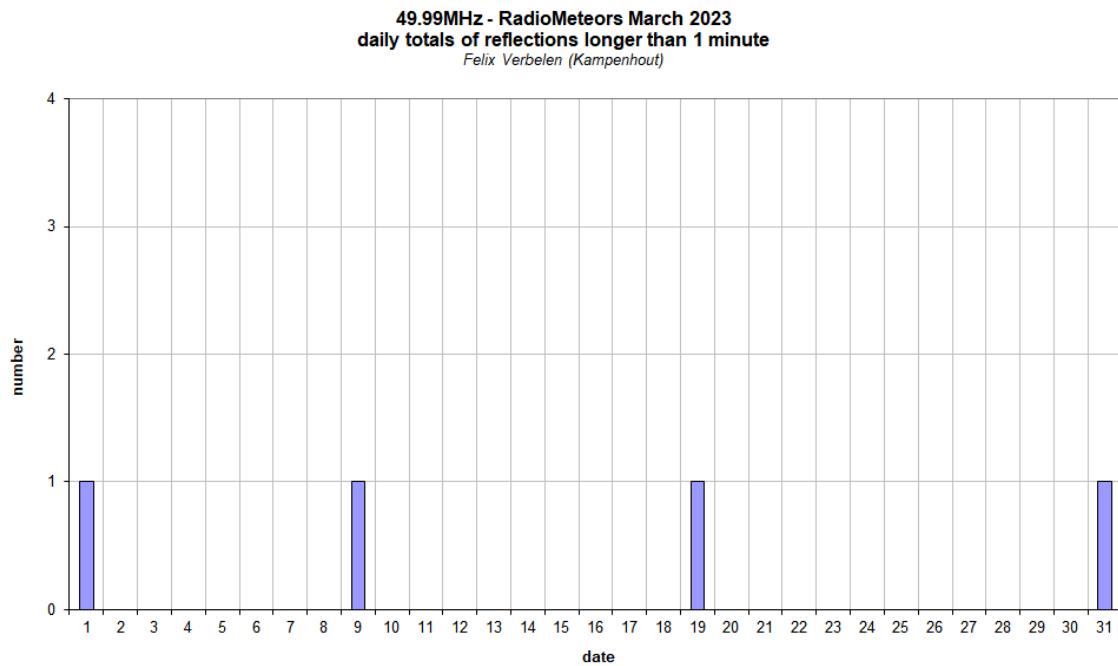
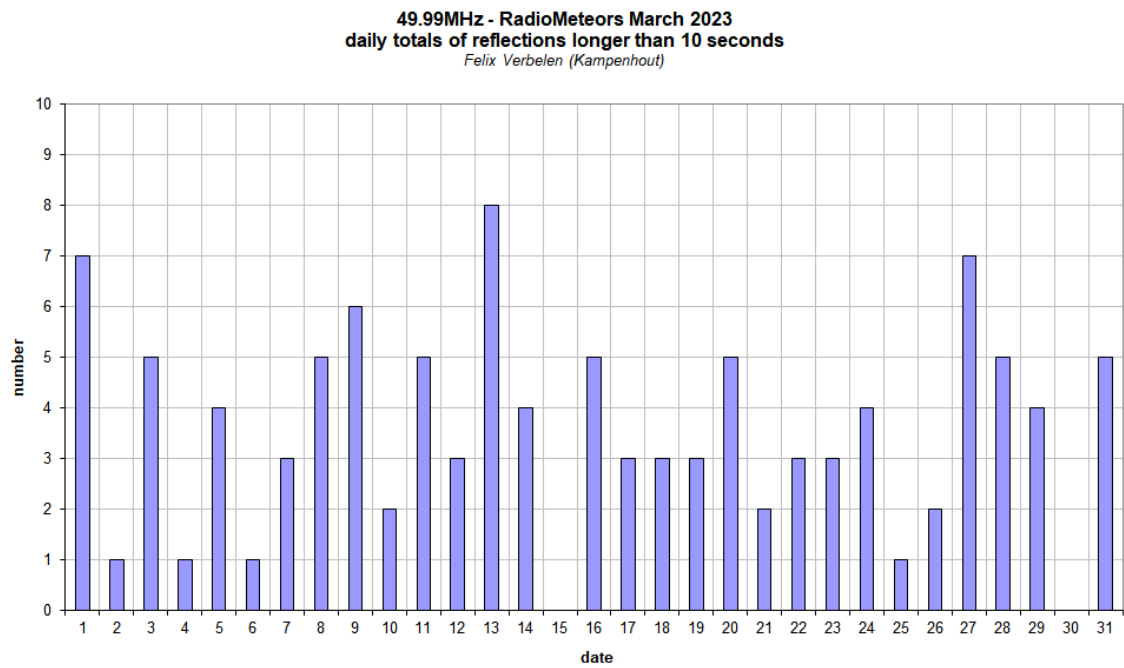


Figure 2 – The daily totals of overdense reflections longer than 10 seconds and longer than 1 minute, as observed here at Kamphenhout (BE) on the frequency of our VVS-beacon (49.99 MHz) during March 2023.

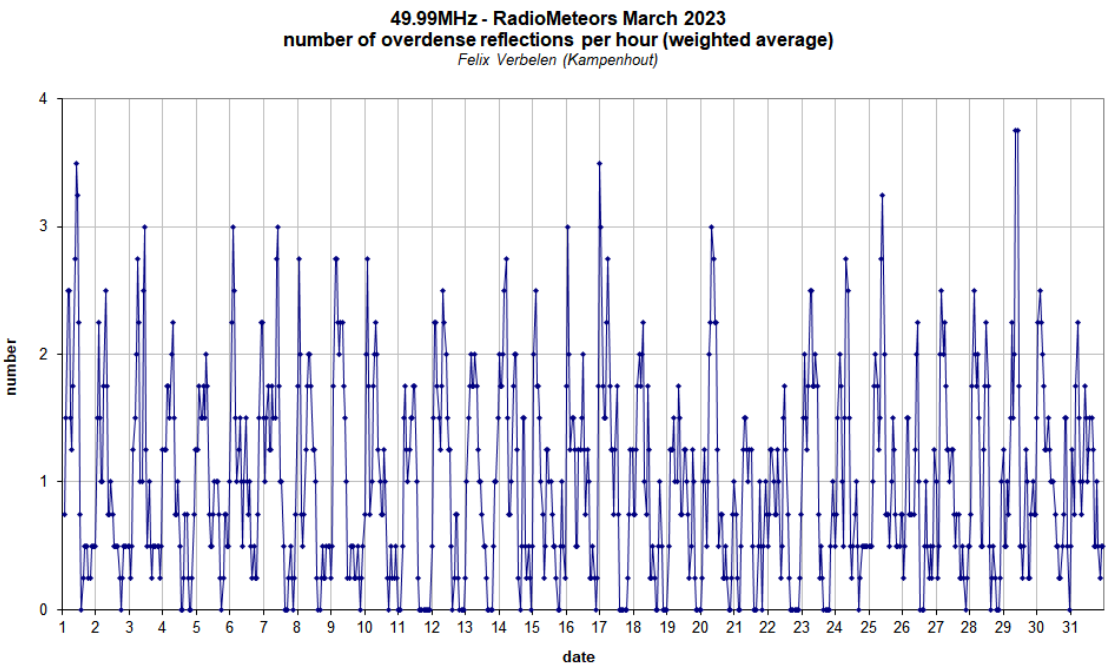
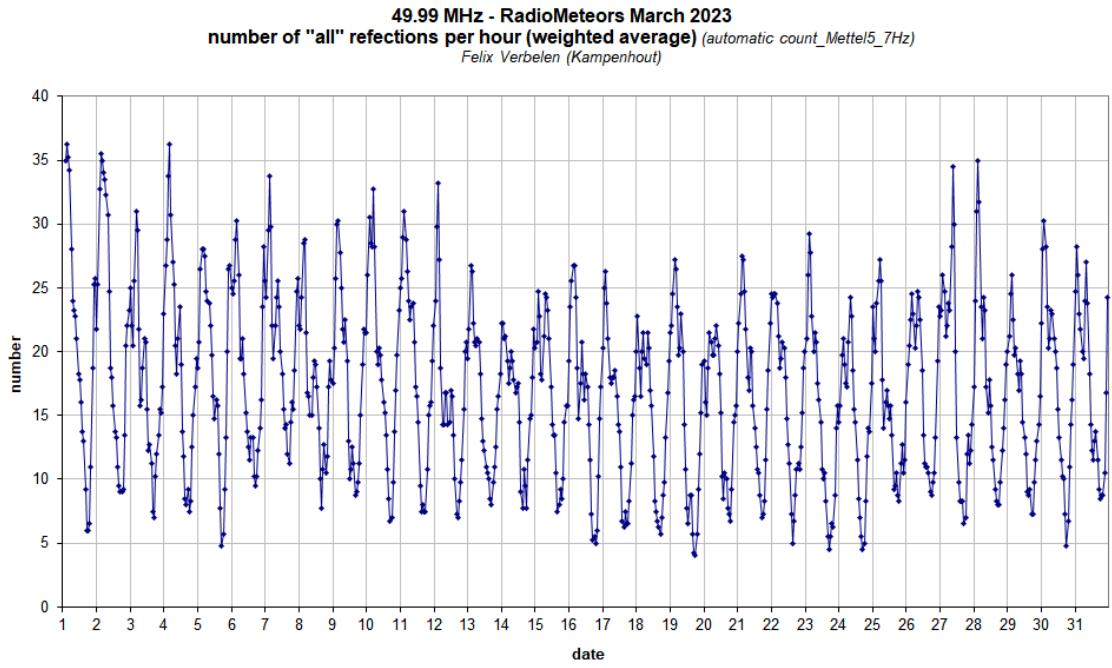


Figure 3 – The hourly numbers of “all” reflections counted automatically, and of manually counted “overdense” reflections, as observed here at Kamphenhout (BE) on the frequency of our VVS-beacon (49.99 MHz) during March 2023.

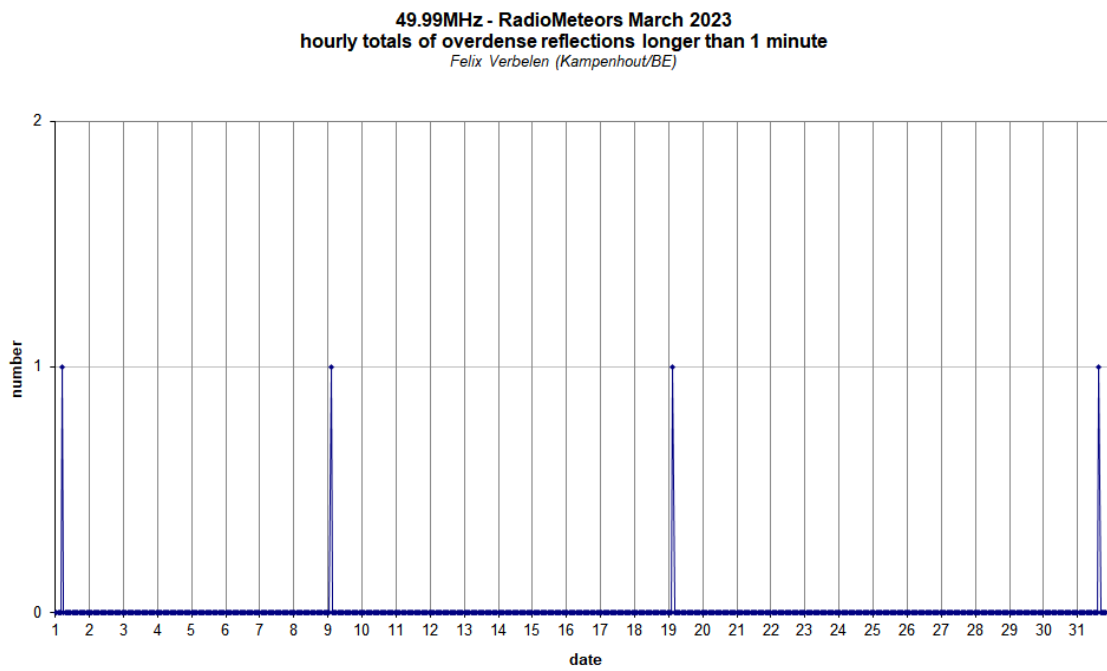
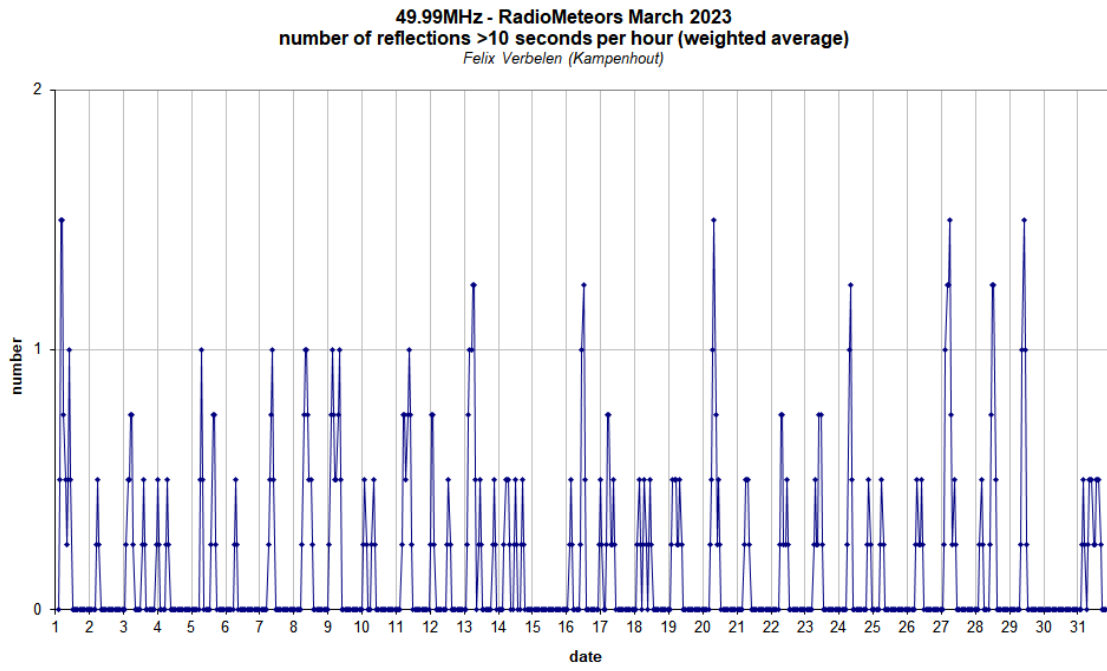


Figure 4 – The hourly numbers of overdense reflections longer than 10 seconds and longer than 1 minute, as observed here at Kampenhout (BE) on the frequency of our VVS-beacon (49.99 MHz) during March 2023.

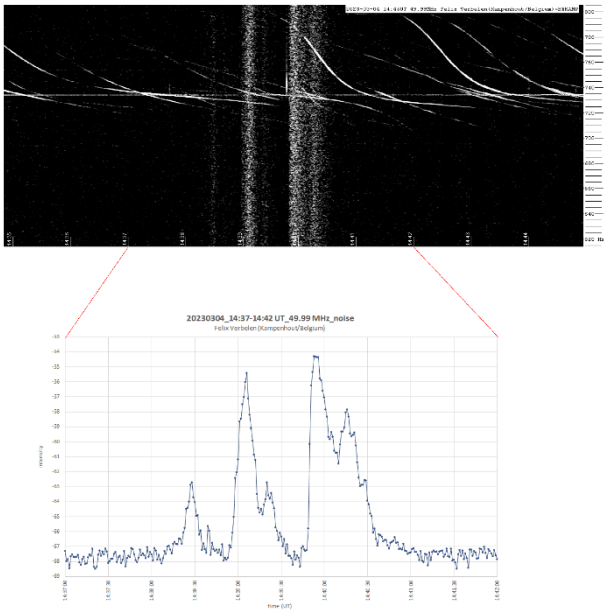


Figure 5 – Solar noise outburst on 4 March 2023.

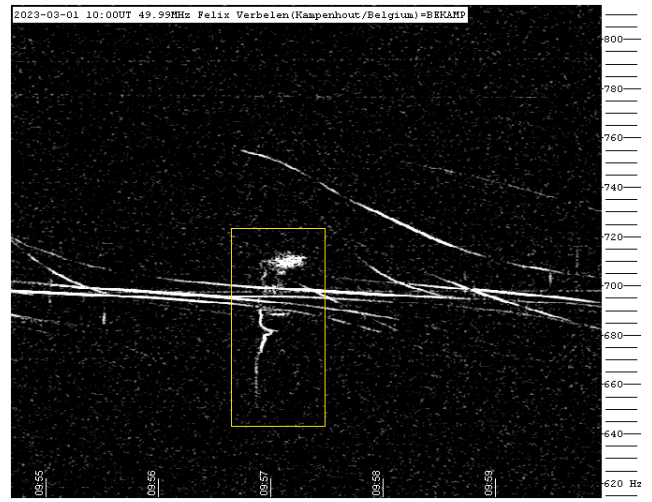


Figure 8 – Meteor echo 1 March 2023, 10^h00^m UT.

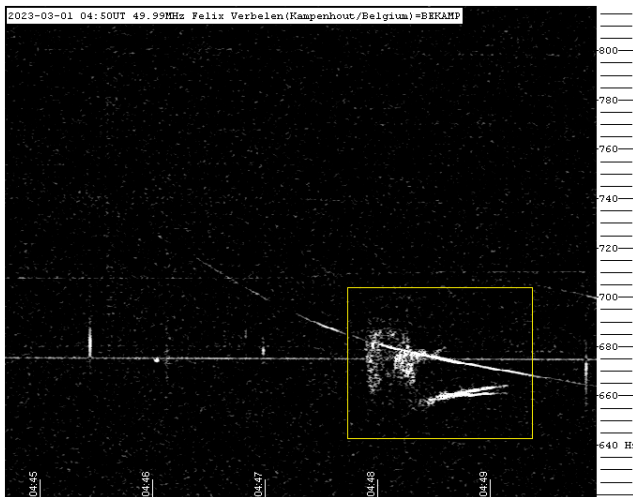


Figure 6 – Meteor echo 1 March 2023, 4^h50^m UT.

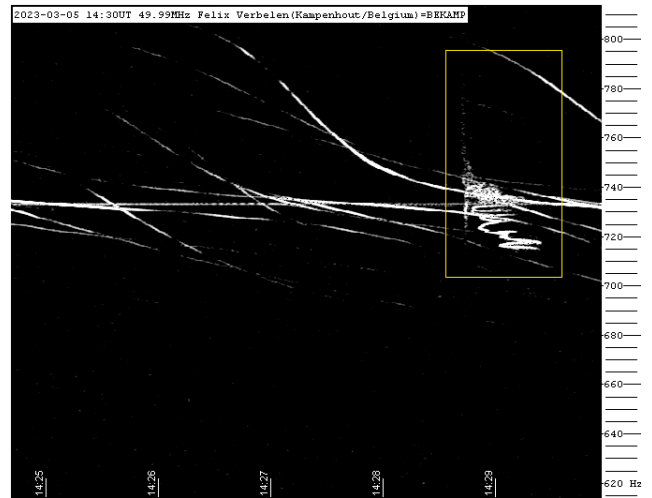


Figure 9 – Meteor echo 5 March 2023, 14^h30^m UT.

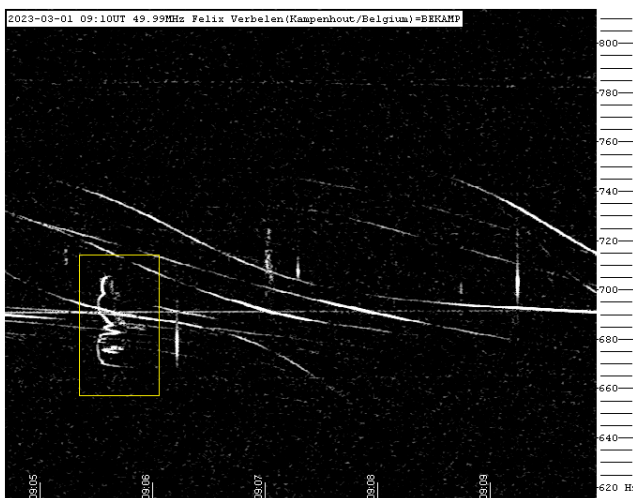


Figure 7 – Meteor echo 1 March 2023, 9^h10^m UT.

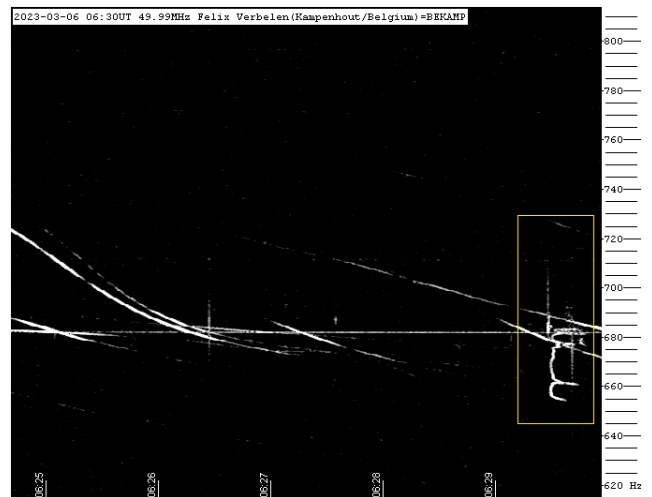


Figure 10 – Meteor echo 6 March 2023, 6^h30^m UT.

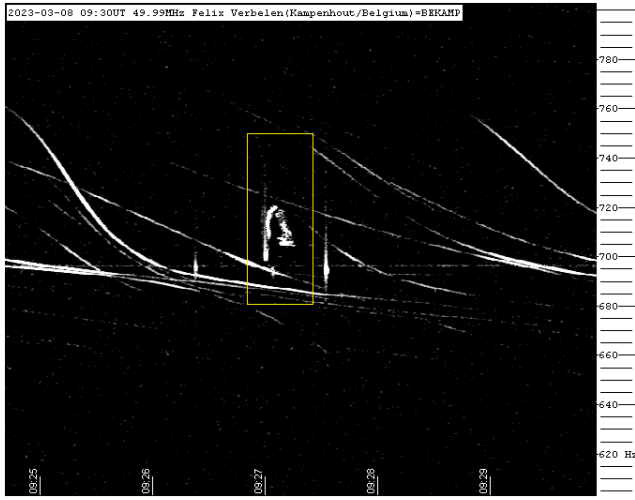


Figure 11 – Meteor echo 8 March 2023, 9^h30^m UT.

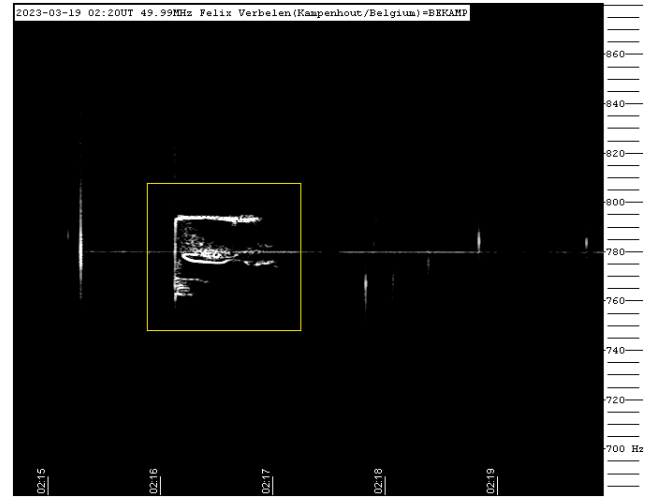


Figure 14 – Meteor echo 19 March 2023, 2^h20^m UT.

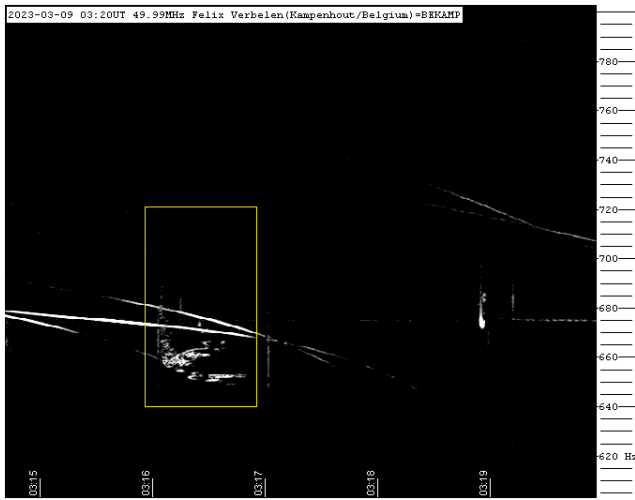


Figure 12 – Meteor echo 9 March 2023, 3^h20^m UT.

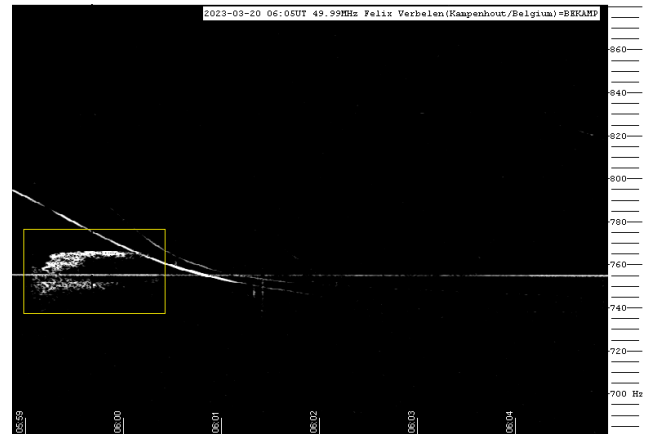


Figure 15 – Meteor echo 20 March 2023, 6^h05^m UT.

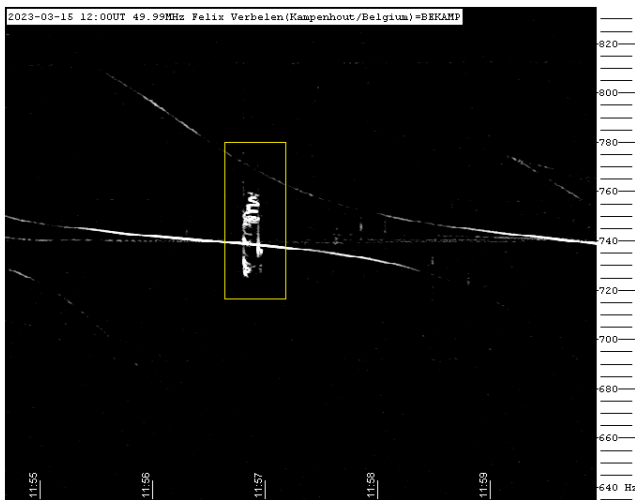


Figure 13 – Meteor echo 15 March 2023, 12^h00^m UT.

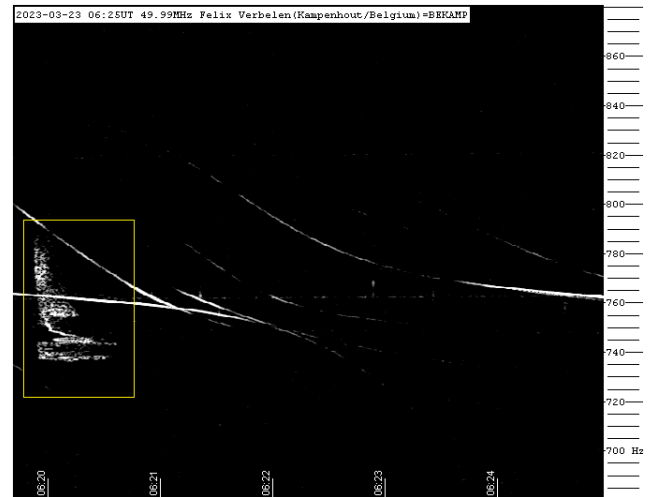


Figure 16 – Meteor echo 23 March 2023, 6^h25^m UT.

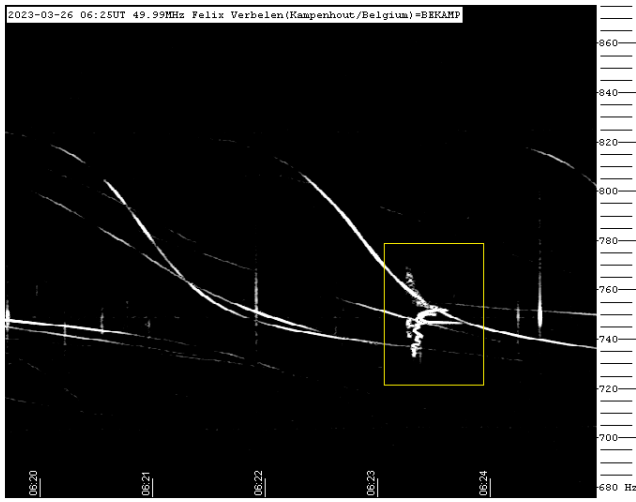


Figure 17 – Meteor echo 26 March 2023, 6^h25^m UT.

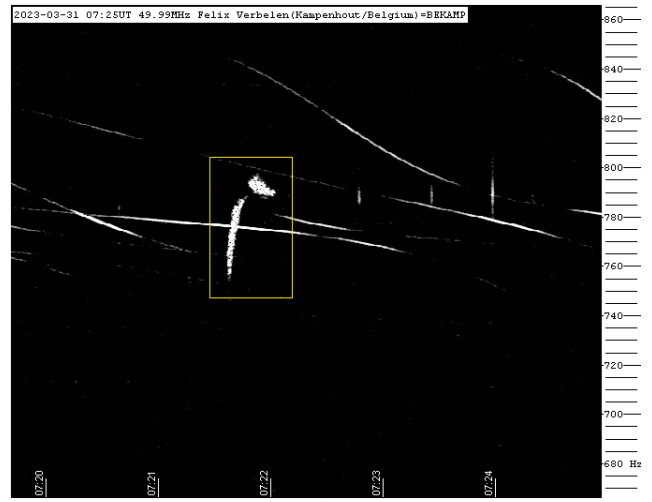


Figure 20 – Meteor echo 31 March 2023, 7^h25^m UT.

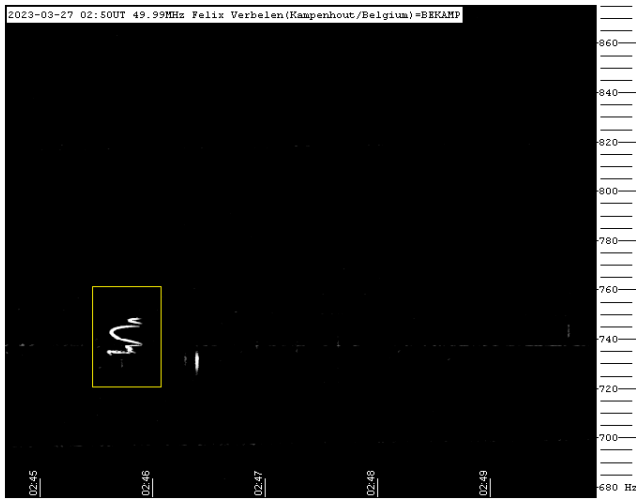


Figure 18 – Meteor echo 27 March 2023, 2^h50^m UT.

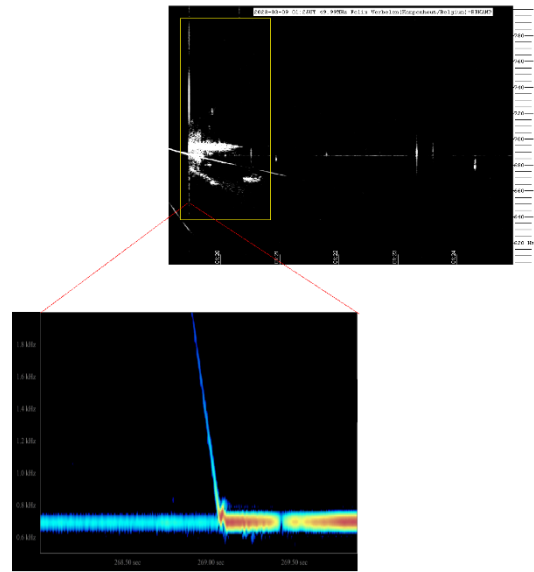


Figure 21 – Head reflections 9 March 2023, 01^h19^m UT.

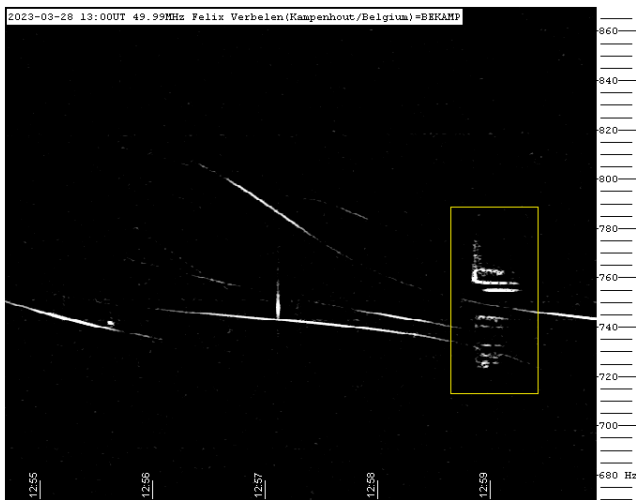


Figure 19 – Meteor echo 28 March 2023, 13^h00^m UT.

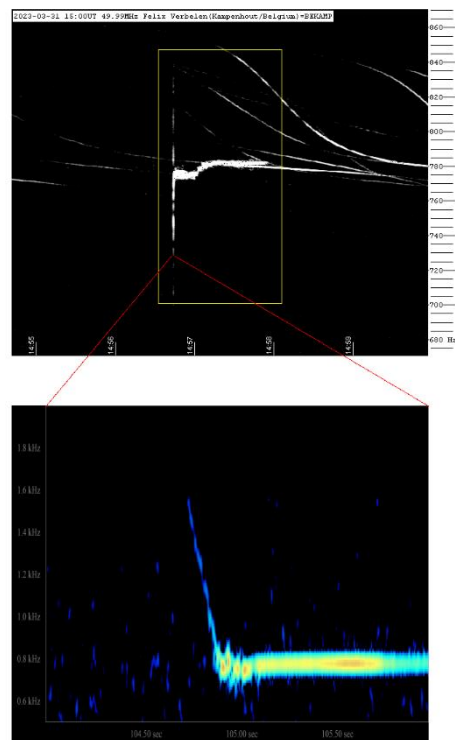


Figure 22 – Head reflections 31 March 2023, 14^h56^m UT.

The Southwestern Europe Meteor Network: remarkable meteors recorded between February and March 2023

J.M. Madiedo¹, J.L. Ortiz¹, J. Izquierdo², P. Santos-Sanz¹, J. Aceituno³, E. de Guindos³,
P. Yanguas⁴, J. Palacián⁴, A. San Segundo⁵, D. Ávila⁶, B. Tosar⁷, A. Gómez-Hernández⁸,
Juan Gómez-Martínez⁸, Antonio García⁹, and A.I. Aimee¹⁰

¹ Departamento de Sistema Solar, Instituto de Astrofísica de Andalucía (IAA-CSIC), 18080 Granada, Spain
madiedo@cica.es, ortiz@iaa.es, psantos@iaa.es

² Departamento de Física de la Tierra y Astrofísica, Universidad Complutense de Madrid, 28040 Madrid, Spain
jizquierdo9@gmail.com

³ Observatorio Astronómico de Calar Alto (CAHA), E-04004, Almería, Spain
aceitun@caha.es, guindos@caha.es

⁴ Departamento de Estadística, Informática y Matemáticas e Institute for Advanced Materials and Mathematics,
Universidad Pública de Navarra, 31006 Pamplona, Navarra, Spain
yanguas@unavarra.es, palacian@unavarra.es

⁵ Observatorio El Guijo (MPC J27), Galapagar, Madrid, Spain
mpcj27@outlook.es

⁶ Estación de Meteoros de Ayora, Ayora, Valencia, Spain
David_ayora007@hotmail.com

⁷ Casa das Ciencias. Museos Científicos Coruñeses. A Coruña, Spain
borjatosar@gmail.com

⁸ Estación de Registro La Lloma, Olocau, Valencia, Spain
curso88@gmail.com

⁹ Estación de Meteoros de Cullera (Faro de Cullera), Valencia, Spain
antonio.garcia88@joseantoniogarcia.com

¹⁰ Southwestern Europe Meteor Network, 41012 Sevilla, Spain
swemn.server@gmail.com

This work focuses on the analysis of some of the bright meteors recorded by the Southwestern Europe Meteor Network from February to March 2023. These were spotted from Spain. Their absolute magnitude ranges from –8 to –11. Bolides included in this report were associated with the sporadic background and minor meteoroid streams.

1 Introduction

Our team is performing since 2006 a systematic monitoring of meteor activity in the framework of the SMART project (Spectroscopy of Meteoroids by means of Robotic Technologies), which started operation in 2006 with the aim to determine valuable clues about the properties of meteoroids ablating in the Earth's atmosphere. This includes chemical information derived from the emission spectra of meteors generated by these particles of interplanetary matter. This survey is being conducted in the framework of the Southwestern Europe Meteor Network (SWEMN). It employs an array of automated spectrographs deployed at different meteor-observing stations in Spain (Madiedo, 2014; Madiedo, 2017). This allows to derive the luminous path of meteors and the orbit of their progenitor meteoroids, and also to study the evolution of meteor

plasmas from the emission spectrum produced by these events (Madiedo, 2015a; 2015b). SMART also provides important information for our MIDAS project, which is being conducted by the Institute of Astrophysics of Andalusia (IAA-CSIC) to study lunar impact flashes produced when large meteoroids impact the Moon (Madiedo et al., 2015; Madiedo et al., 2018; Madiedo et al., 2019; Ortiz et al., 2015).

In this work we describe the preliminary analysis of six bright meteors recorded by the SWEMN network along February and March 2023. This work has been fully written by AIMEE (acronym for Artificial Intelligence with Meteoroid Environment Expertise) from the records included in the SWEMN fireball database (Madiedo et al., 2021; Madiedo et al., 2022).

2 Equipment and methods

The events presented here have been recorded by using Watec 902H2 and Watec 902 Ultimate cameras. Their field of view ranges from 62×50 degrees to 14×11 degrees. To record meteor spectra we have attached holographic diffraction gratings (1000 lines/mm) to the lens of some of these cameras. We have also employed digital CMOS color cameras (models Sony A7S and A7SII) operating in HD video mode (1920×1080 pixels). These cover a field of view of around 70×40 degrees. A detailed description of this hardware and the way it operates was given in previous works (Madiedo, 2017). Besides digital CMOS cameras manufactured by ZWO (model ASI185MC) were used. The atmospheric paths of the events were triangulated by means of the SAMIA software, developed by J.M. Madiedo. This program employs the planes-intersection method (Ceplecha, 1987).



Figure 1 – Stacked image of the SWEMN20230201_200423 “Oulad Ameer” fireball as recorded from Calar Alto.

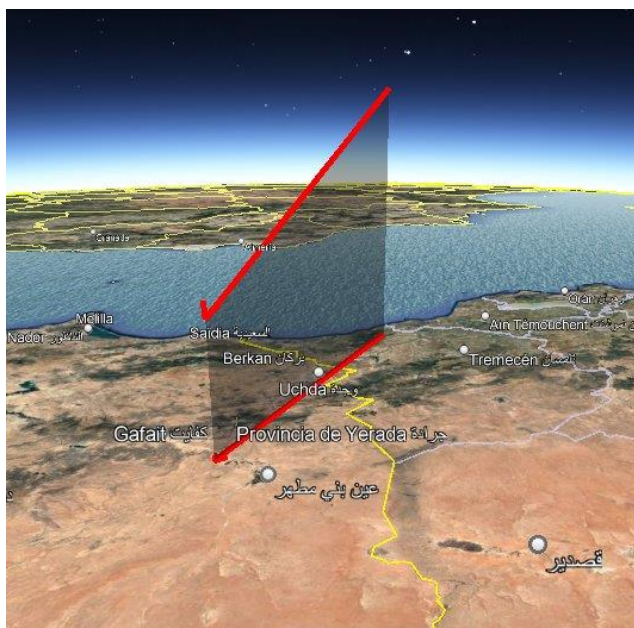


Figure 2 – Atmospheric path of the SWEMN20230201_200423 “Oulad Ameer” fireball, and its projection on the ground.

3 Description of the 2023 February 1 meteor

This striking bolide was recorded on 2023 February 1 at $20^{\text{h}}04^{\text{m}}23.0 \pm 0.1^{\text{s}}$ UT from the meteor-observing stations located at Huelva, La Hita (Toledo), Calar Alto, Sierra Nevada, La Sagra (Granada), and Sevilla (Figure 1). The maximum luminosity of the event was equivalent to an absolute magnitude of -11.0 ± 1.0 . It was listed in the SWEMN meteor database with the code SWEMN20230201_200423. The fireball could also be observed by a wide number of causal eyewitnesses.

Atmospheric trajectory, radiant and orbit

The analysis of the atmospheric trajectory of the bright meteor revealed that this bolide overflowed Algeria and Morocco. The luminous event began at an altitude $H_b = 93.2 \pm 0.5$ km. The meteor penetrated the atmosphere till a final height $H_e = 41.6 \pm 0.5$ km. The equatorial coordinates found for the apparent radiant are $\alpha = 160.04^\circ$, $\delta = +59.10^\circ$. The entry velocity in the atmosphere inferred for the parent meteoroid was $v_\infty = 25.5 \pm 0.3$ km/s. The obtained trajectory in our atmosphere of the bolide is shown in Figure 2. The heliocentric orbit of the parent meteoroid is drawn in Figure 3.

Table 1 – Orbital data (J2000) of the progenitor meteoroid before its encounter with our planet.

a (AU)	1.90 ± 0.06	ω ($^\circ$)	247.6 ± 00.6
e	0.60 ± 0.01	Ω ($^\circ$)	312.386216 ± 10^{-5}
q (AU)	0.755 ± 0.002	i ($^\circ$)	30.1 ± 0.3

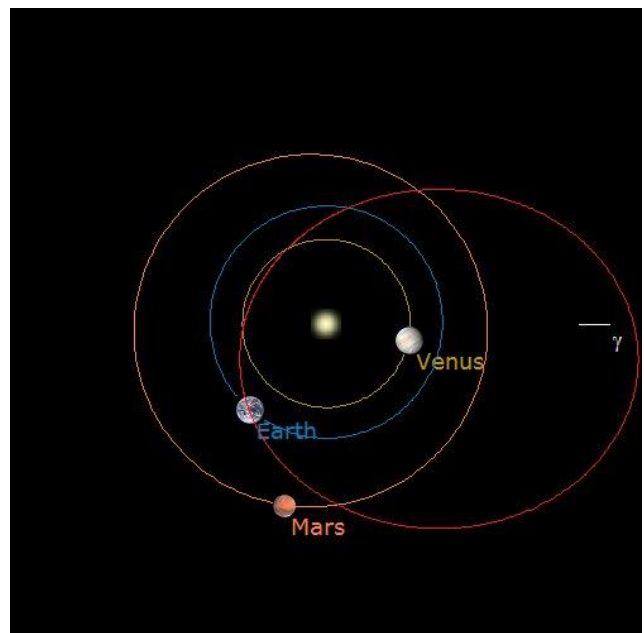


Figure 3 – Projection on the ecliptic plane of the orbit of the parent meteoroid of the SWEMN20230201_200423 “Oulad Ameer” bolide.

This fireball was named “Oulad Ameer”, because the meteor was located over this locality during its initial phase. Table 1 contains the orbital parameters of the progenitor meteoroid before its encounter with our planet, and the

geocentric velocity derived in this case was $v_g = 22.7 \pm 0.3$ km/s. From the value derived for the Tisserand parameter with respect to Jupiter ($T_J = 3.56$), we found that the meteoroid was moving on an asteroidal orbit before entering the atmosphere. By taking into account these parameters and the derived radiant position, it was concluded that the bright meteor was produced by the sporadic component.



Figure 4 – Stacked image of the SWEMN20230302_011351 “Casa de la Vega” fireball.



Figure 5 – Atmospheric path of the SWEMN20230302_011351 “Casa de la Vega” fireball, and its projection on the ground.

4 Analysis of the 2023 March 2 bolide

This bright bolide was captured on 2023 March 2, at $1^{\text{h}}13^{\text{m}}51.0 \pm 0.1^{\text{s}}$ UT (Figure 4). Its maximum brightness was equivalent to an absolute magnitude of -8.0 ± 1.0 . It was listed in the SWEMN meteor database with the code SWEMN20230302_011351.

Atmospheric path, radiant and orbit

It was deduced by calculating the luminous path of the event that this fireball overflowed the province of Cuenca (Spain). The meteoroid started ablating at a height $H_b = 130.7 \pm 0.5$ km, with the terminal point of the luminous phase located at a height $H_e = 85.6 \pm 0.5$ km. The position concluded for the apparent radiant corresponds to the equatorial coordinates $\alpha = 239.55^\circ$, $\delta = -1.78^\circ$. The entry velocity in the atmosphere deduced for the progenitor meteoroid was $v_\infty = 68.5 \pm 0.3$ km/s. The calculated atmospheric path of the bright meteor is shown in Figure 5, and the heliocentric orbit of the meteoroid is drawn in Figure 6.

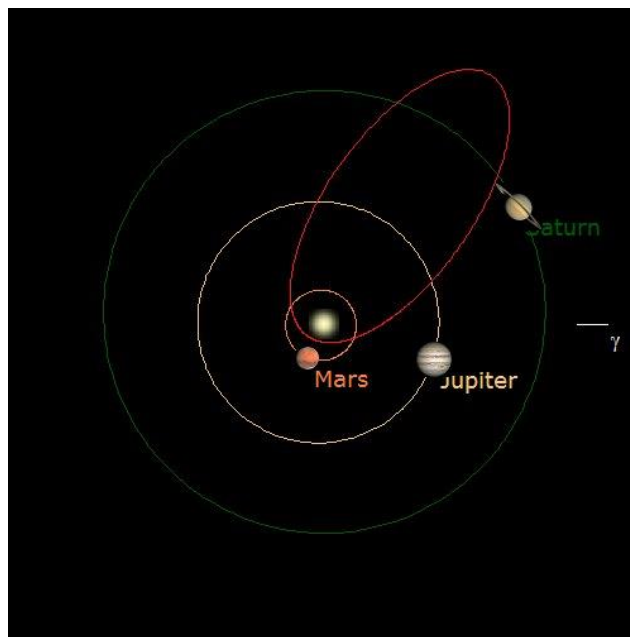


Figure 6 – Projection on the ecliptic plane of the orbit of the parent meteoroid of the SWEMN20230302_011351 “Casa de la Vega” event.

This bright meteor was named “Casa de la Vega”, because the event was located near the zenith of this locality during its final phase. The parameters of the orbit in the Solar System of the progenitor meteoroid before its encounter with our planet are listed in Table 2. The geocentric velocity obtained for the particle yields $v_g = 67.3 \pm 0.3$ km/s. The value found for the Tisserand parameter referred to Jupiter ($T_J = -0.23$) suggests that the meteoroid followed a cometary (HTC) orbit before entering the atmosphere. These data and the calculated radiant coordinates confirm that the event was associated with the February μ -Virginids (IAU shower code FMV#0516).

Table 2 – Orbital data (J2000) of the progenitor meteoroid before its encounter with our planet.

a (AU)	7.3 ± 1.4	ω ($^\circ$)	223.3 ± 00.7
e	0.88 ± 0.02	Ω ($^\circ$)	340.870887 ± 10^{-5}
q (AU)	0.864 ± 0.002	i ($^\circ$)	147.1 ± 0.1

5 The second bright meteor on 2023 March 2

We recorded this bright meteor from the meteor-observing stations located at Huelva, La Hita (Toledo), Calar Alto, Sierra Nevada, La Sagra (Granada), and Sevilla (*Figure 7*). The bolide was captured on 2023 March 2, at $3^{\text{h}}56^{\text{m}}05.0 \pm 0.1^{\text{s}}$ UT. The peak brightness of the event, that presented a bright flare at the final phase of its trajectory in our atmosphere, was equivalent to an absolute magnitude of -10.0 ± 1.0 . This flare arose as a consequence of the sudden disruption of the meteoroid. The code assigned to the bolide in the SWEMN meteor database is SWEMN20230302_035605. The bright meteor can be viewed on YouTube¹⁷.



Figure 7 – Stacked image of the SWEMN20230302_035605 “Oulad Khallouf” event.

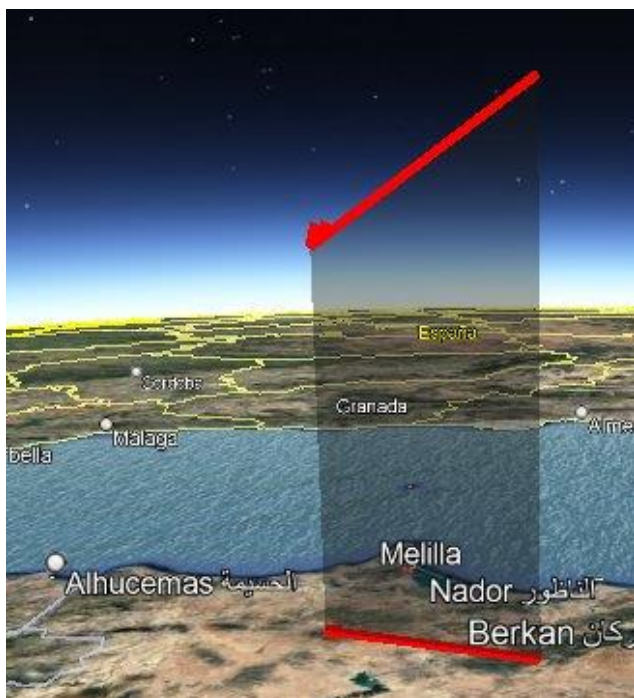


Figure 8 – Atmospheric path of the SWEMN20230302_035605 “Oulad Khallouf” meteor, and its projection on the ground.

Atmospheric path, radiant and orbit

By calculating the trajectory in the atmosphere of the event it was concluded that this fireball overflowed Morocco. Its initial altitude was $H_b = 119.5 \pm 0.5$ km. The event penetrated the atmosphere till a final height $H_e = 84.5 \pm 0.5$ km. The position concluded for the apparent radiant corresponds to the equatorial coordinates $\alpha = 264.97^\circ$, $\delta = +2.54^\circ$. Besides, we deduced that the meteoroid entered the atmosphere with a velocity $v_\infty = 66.1 \pm 0.3$ km/s. *Figure 8* shows the calculated trajectory in our atmosphere of the meteor. The heliocentric orbit of the meteoroid is shown in *Figure 9*.

We named this fireball “Oulad Khallouf”, since the bolide was located over this locality during its initial phase. The parameters of the heliocentric orbit of the parent meteoroid before its encounter with our planet have been listed in *Table 3*, and the geocentric velocity derived in this case was $v_g = 64.9 \pm 0.3$ km/s. According to the value calculated for the Tisserand parameter with respect to Jupiter ($T_J = -0.25$), the meteoroid followed a cometary (HTC) orbit before entering the atmosphere. Radiant and orbital data do not match any of the meteoroid streams in the IAU meteor database. So, we concluded that this event was produced by the sporadic background.

Table 3 – Orbital data (J2000) of the progenitor meteoroid before its encounter with our planet.

a (AU)	9.6 ± 2.4	ω ($^\circ$)	139.1 ± 00.7
e	0.90 ± 0.02	Ω ($^\circ$)	340.984545 ± 10^{-5}
q (AU)	0.875 ± 0.002	i ($^\circ$)	133.7 ± 0.1

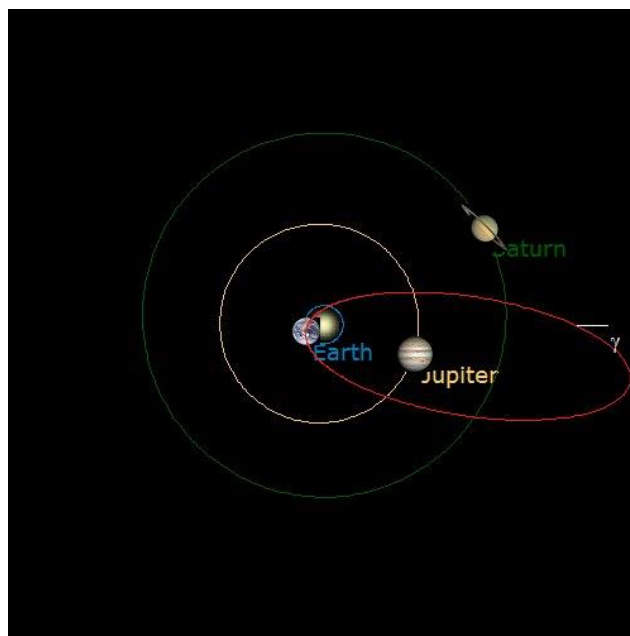


Figure 9 – Projection on the ecliptic plane of the orbit of the parent meteoroid of the SWEMN20230302_035605 “Oulad Khallouf” meteor.

¹⁷ <https://youtu.be/nZ86vpCCQUk>

6 The third bolide on 2023 March 2

Our cameras captured a third event on 2023 March 2, at $21^{\text{h}}39^{\text{m}}20.0 \pm 0.1^{\text{s}}$ UT. The peak brightness this bright meteor was equivalent to an absolute magnitude of -9.0 ± 1.0 (Figure 10). It was listed in the SWEMN meteor database with the code SWEMN20230302_213920. A wide number of casual observers saw how the fireball crossed the sky, and a video showing the meteor was uploaded to YouTube¹⁸.



Figure 10 – Stacked image of the SWEMN20230302_213920 “Arroyos” event.



Figure 11 – Atmospheric path of the SWEMN20230302_213920 “Arroyos” bolide, and its projection on the ground.

Atmospheric path, radiant and orbit

This event overflew the provinces of Almería and Jaén (south of Spain). It began at an altitude $H_b = 100.1 \pm 0.5$ km, and penetrated the atmosphere till a final height $H_e = 41.6 \pm 0.5$ km. The position inferred for the apparent radiant corresponds to the equatorial coordinates $\alpha = 160.63^\circ$, $\delta = -2.77^\circ$. The meteoroid hit the atmosphere with an initial velocity $v_\infty = 26.8 \pm 0.3$ km/s. The obtained trajectory in the Earth’s atmosphere of the bright meteor is

shown in Figure 11. The heliocentric orbit of the meteoroid is drawn in Figure 12.

This event was named “Arroyos”, because the bolide overflew this locality during its final phase. Table 4 contains the parameters of the orbit in the Solar System of the progenitor meteoroid before its encounter with our planet. The value calculated for the geocentric velocity was $v_g = 24.2 \pm 0.3$ km/s. According to the value found for the Tisserand parameter with respect to Jupiter ($T_J = 3.10$), the particle was moving on an asteroidal orbit before colliding with our atmosphere. By taking into account these data and the derived radiant position, it was concluded that the bright meteor was produced by the η -Virginids (IAU code EVI#0011) (Jenniskens et al., 2016).

Table 4 – Orbital data (J2000) of the progenitor meteoroid before its encounter with our planet.

a (AU)	2.30 ± 0.09	ω ($^\circ$)	92.3 ± 0.2
e	0.76 ± 0.01	Ω ($^\circ$)	161.720834 ± 10^{-5}
q (AU)	0.544 ± 0.003	i ($^\circ$)	9.7 ± 0.1

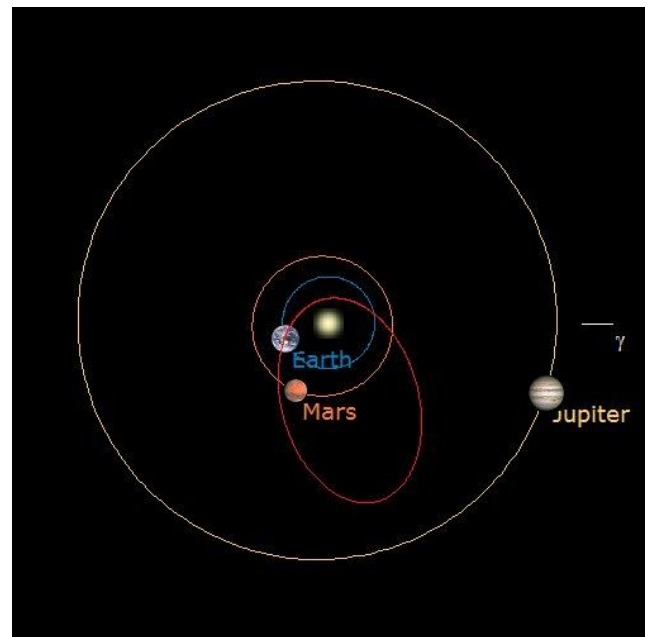


Figure 12 – Projection on the ecliptic plane of the orbit of the parent meteoroid of the SWEMN20230302_213920 “Arroyos” meteor.

7 Description of the 2023 March 8 bolide

We recorded this bright meteor from the meteor-observing stations located at Huelva, La Hita (Toledo), Calar Alto, Sierra Nevada, La Sagra (Granada), and Sevilla. The bolide was spotted on 2023 March 8, at $22^{\text{h}}15^{\text{m}}18.0 \pm 0.1^{\text{s}}$ UT. It had a peak absolute magnitude of -8.0 ± 1.0 (Figure 13) and exhibited a series of flares along its luminous path as a consequence of the sudden break-up of the meteoroid. The event was added to our meteor database with the code SWEMN20230308_221518. A video with images of the bolide and its trajectory in our atmosphere was uploaded to

¹⁸ <https://youtu.be/TY842Pm7wBk>

YouTube¹⁹. Casual observers also saw the bright meteor crossing the sky.



Figure 13 – Stacked image of the SWEMN20230308_221518 “Santa Marina” fireball.



Figure 14 – Atmospheric path of the SWEMN20230308_221518 “Santa Marina” fireball, and its projection on the ground.

Atmospheric path, radiant and orbit

From the analysis of the trajectory in our atmosphere of the fireball it was found that this bright meteor overflowed the province of Jaén (south of Spain). Its initial altitude was $H_b = 78.8 \pm 0.5$ km, and the event penetrated the atmosphere till a final height $H_e = 44.7 \pm 0.5$ km. The equatorial coordinates found for the apparent radiant are $\alpha = 154.43^\circ$, $\delta = -1.98^\circ$. Besides, we obtained that the meteoroid hit the atmosphere with a velocity $v_\infty = 22.1 \pm 0.3$ km/s. Figure 14 shows the calculated

trajectory in the atmosphere of the bolide. The orbit in the Solar System of the meteoroid is shown in Figure 15.

Table 5 – Orbital data (J2000) of the progenitor meteoroid before its encounter with our planet.

a (AU)	2.5 ± 0.1	ω ($^\circ$)	68.07 ± 00.07
e	0.71 ± 0.01	Ω ($^\circ$)	167.756983 ± 10^{-5}
q (AU)	0.733 ± 0.002	i ($^\circ$)	8.26 ± 0.08

The bright meteor was named “Santa Marina”, since the fireball was located over this locality during its initial phase. The parameters of the heliocentric orbit of the progenitor meteoroid before its encounter with our planet have been listed in Table 5. The geocentric velocity obtained for the particle yields $v_g = 19.0 \pm 0.3$ km/s. From the value found for the Tisserand parameter with respect to Jupiter ($T_J = 2.99$), we found that the particle followed a cometary (JFC) orbit before colliding with the atmosphere. By taking into account these values and the calculated radiant coordinates, the bolide was linked to the sporadic component.

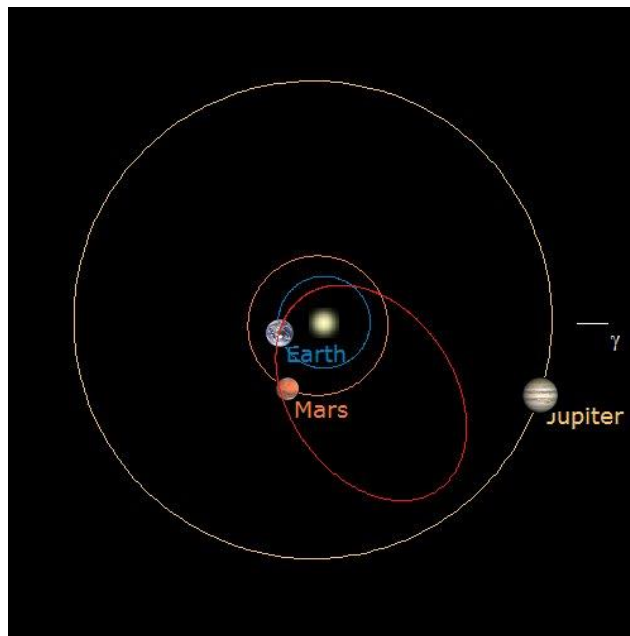


Figure 15 – Projection on the ecliptic plane of the orbit of the progenitor meteoroid of the SWEMN20230308_221518 “Santa Marina” event.

8 Analysis of the 2023 March 12 bolide

This bright event was captured on 2023 March 12, at $1^{\text{h}}24^{\text{m}}57.0 \pm 0.1^{\text{s}}$ UT (Figure 16). Its peak brightness was equivalent to an absolute magnitude of -9.0 ± 1.0 . It presented different flares along its trajectory in the atmosphere as a consequence of the sudden disruption of the meteoroid. The bolide was added to our meteor database with the code SWEMN20230312_012457. A video about this fireball can be viewed on YouTube²⁰.

¹⁹ <https://youtu.be/4XwK6maZiF8>

²⁰ <https://youtu.be/KfLBCi0jt3k>



Figure 16 – Stacked image of the SWEMN20230312_012457 “Pedrezuela” bolide.



Figure 17 – Atmospheric path of the SWEMN20230312_012457 “Pedrezuela” event, and its projection on the ground.

Atmospheric path, radiant and orbit

This bolide overflowed the provinces of Madrid and Segovia (Spain). Its initial altitude was $H_b = 70.8 \pm 0.5$ km. The event penetrated the atmosphere till a final height $H_e = 33.7 \pm 0.5$ km and the apparent radiant was located at the equatorial coordinates $\alpha = 209.35^\circ$, $\delta = -18.53^\circ$. The entry velocity in the atmosphere deduced for the parent meteoroid was $v_\infty = 14.5 \pm 0.2$ km/s. The calculated trajectory in the atmosphere of the fireball is shown in Figure 17, and the orbit in the Solar System of the meteoroid is shown in Figure 18.

Table 6 – Orbital data (J2000) of the progenitor meteoroid before its encounter with our planet.

a (AU)	0.732 ± 0.004	ω ($^\circ$)	161.4 ± 00.2
e	0.40 ± 0.01	Ω ($^\circ$)	170.887076 ± 10^{-5}
q (AU)	0.43 ± 0.01	i ($^\circ$)	7.1 ± 0.1

The name given to the bolide was “Pedrezuela”, because the meteor passed near the zenith of this locality during its initial phase. Table 6 shows the parameters of the orbit in the Solar System of the progenitor meteoroid before its encounter with our planet. The geocentric velocity obtained for the particle yields $v_g = 9.1 \pm 0.3$ km/s. According to the value found for the Tisserand parameter with respect to Jupiter ($T_J = 7.79$), the meteoroid was moving on an asteroidal orbit before impacting our planet’s atmosphere. By taking into account these values and the derived radiant position, the event was linked to the sporadic component.

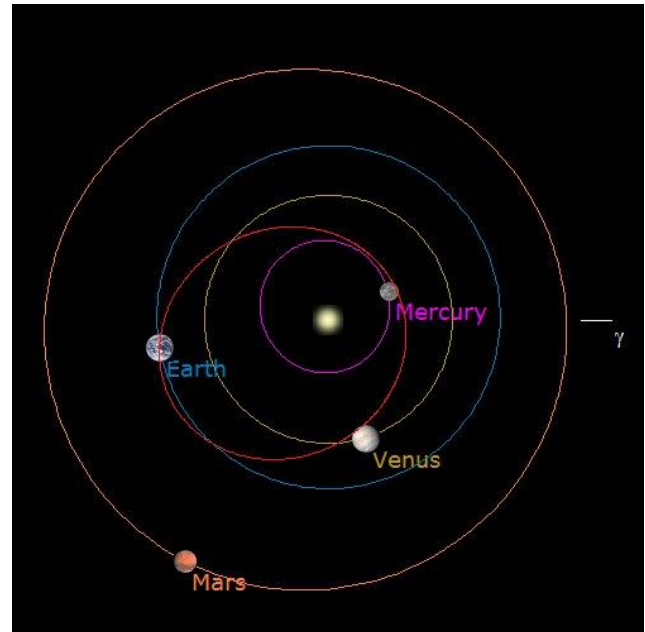


Figure 18 – Projection on the ecliptic plane of the orbit of the progenitor meteoroid of the SWEMN20230312_012457 “Pedrezuela” meteor.

9 Conclusions

Some of the most luminous bolides recorded by SWEMN from February to March 2023 have been presented here. Their absolute magnitude ranges from -8 to -11 .

The “Oulad Ameer” event was recorded on February 1. This sporadic fireball had a peak absolute magnitude of -11.0 and overflowed Algeria and Morocco. The particle followed an asteroidal orbit before colliding with the Earth’s atmosphere. This deep-penetrating meteor reached a final height of about 41 km.

Next, we have described an event recorded on March 2 which was named “Casa de la Vega”. It reached a peak absolute magnitude of -8.0 and belonged to the February μ -Virginids (FMV#0516). This meteor overflowed the province of Cuenca (Spain). Before colliding with our atmosphere, the meteoroid was moving on a cometary (HTC) orbit.

The third bright meteor presented here was the “Oulad Khallouf” fireball. This was also recorded on March 2. It reached a peak absolute magnitude of -10.0 and was associated with the sporadic component. This meteor overflowed Morocco. The progenitor particle followed a cometary (HTC) orbit before hitting our atmosphere.

Next, we have discussed the “Arroyos” bright meteor. This was the third remarkable event recorded on March 2. Its peak magnitude was -9.0 . The meteor was produced by an η -Virginid (EVI#0011) meteoroid and overflowed the provinces of Almería and Jaén (south of Spain). Before hitting our atmosphere, the meteoroid was moving on an asteroidal orbit. At the terminal stage of its luminous phase this deep-penetrating fireball was located at a height of about 41 km.

The fifth bright meteor analyzed here was a fireball recorded on March 8 which was named “Santa Marina”. The peak magnitude of this sporadic, which overflowed Jaén (Spain), was -8.0 . The particle was moving on a cometary (JFC) orbit before colliding with the Earth’s atmosphere. This deep-penetrating fireball reached an ending height of about 44 km.

And the last fireball described in this paper was the “Pedrezuela” fireball, which was recorded on March 12. It reached a peak absolute magnitude of -9.0 and belonged to the sporadic. This meteor event overflowed Madrid and Segovia (Spain). Before striking our planet’s atmosphere the particle was moving on an asteroidal orbit. This deep-penetrating bolide reached a terminal height of about 33 km.

Acknowledgment

We acknowledge support from the Spanish Ministry of Science and Innovation (project PID2019-105797GB-I00). We also acknowledge financial support from the State Agency for Research of the Spanish MCIU through the “Center of Excellence Severo Ochoa” award to the Instituto de Astrofísica de Andalucía (SEV-2017-0709). P.S.-S. acknowledges financial support by the Spanish grant AYA - RTI2018 – 098657 – J - I00 “LEO – SBNAF” (MCIU / AEI / FEDER, UE). The first author is very grateful to Casa das Ciencias (Museos Científicos Coruñeses) for their helpful support in the setup and operation of the automated meteor-observing station located at their facilities in A Coruña.

References

- Ceplecha Z. (1987). “Geometric, dynamic, orbital and photometric data on meteoroids from photographic fireball networks”. *Bull. Astron. Inst. Cz.*, **38**, 222–234.
- Jenniskens P., Nénon Q., Albers J., Gural P. S., Haberman B., Holman D., Morales R., Grigsby B. J., Samuels D. and Johannink C. (2016). “The established meteor showers as observed by CAMS”. *Icarus*, **266**, 331–354.
- Madiedo J. M. (2014). “Robotic systems for the determination of the composition of solar system materials by means of fireball spectroscopy”. *Earth, Planets & Space*, **66**, 70.
- Madiedo J. M. (2017). “Automated systems for the analysis of meteor spectra: The SMART Project”. *Planetary and Space Science*, **143**, 238–244.
- Madiedo J. M. (2015a). “Spectroscopy of a κ -Cygnid fireball afterglow”. *Planetary and Space Science*, **118**, 90–94.
- Madiedo J. M. (2015b). “The ρ -Geminid meteoroid stream: orbits, spectroscopic data and implications for its parent body”. *Monthly Notices of the Royal Astronomical Society*, **448**, 2135–2140.
- Madiedo J. M., Ortiz J. L., Organero F., Ana-Hernández L., Fonseca F., Morales N. and Cabrera-Caño J. (2015). “Analysis of Moon impact flashes detected during the 2012 and 2013 Perseids”. *A&A*, **577**, A118.
- Madiedo J. M., Ortiz J. L. and Morales N. (2018). “The first observations to determine the temperature of a lunar impact flash and its evolution”. *Monthly Notices of the Royal Astronomical Society*, **480**, 5010–5016.
- Madiedo J. M., Ortiz J. L., Morales N. and Santos-Sanz P. (2019a). “Multiwavelength observations of a bright impact flash during the 2019 January total lunar eclipse”. *Monthly Notices of the Royal Astronomical Society*, **486**, 3380–3387.
- Madiedo J. M., Ortiz J. L., Izquierdo J., Santos-Sanz P., Aceituno J., de Guindos E., Yanguas P., Palacian J., San Segundo A., and Avila D. (2021). “The Southwestern Europe Meteor Network: recent advances and analysis of bright fireballs recorded along April 2021”. *eMetN*, **6**, 397–406.
- Madiedo J. M., Ortiz J. L., Izquierdo J., Santos-Sanz P., Aceituno J., de Guindos E., Yanguas P., Palacian J., San Segundo A., Avila D., Tosar B., Gómez-Hernández A., Gómez-Martínez J., and García A. (2022). “The Southwestern Europe Meteor Network: development of new artificial intelligence tools and remarkable fireballs observed from January to February 2022”. *eMeteorNews*, **7**, 199–208.
- Ortiz J. L., Madiedo J. M., Morales N., Santos-Sanz P. and Aceituno F. J. (2015). “Lunar impact flashes from Geminids: analysis of luminous efficiencies and the flux of large meteoroids on Earth”. *Monthly Notices of the Royal Astronomical Society*, **454**, 344–352.

The mission of MeteorNews is to offer fast meteor news to a global audience, a swift exchange of information in all fields of active amateur meteor work without editing constraints. MeteorNews is freely available without any fees. To receive a notification: <https://www.meteornews.net/newsletter-signup/>.

You are welcome to contribute to MeteorNews on a regular or casual basis, if you wish to. Anyone can become an author or editor, send an email to us. For more info read: <https://meteornews.net/writing-content-for-emeteornews/>

MeteorNews account manager: Richard Kacerek rickzkm@gmail.com.

The running costs for website hosting are covered by a team of sponsors. We want to thank the 2022-2023 sponsors: Anonymous (3x), Mikhail Bidnichenko, Gaetano Brando, TomB, Trevor C, Nigel Cunnington, Richard Glassner, Kevin Heider, Paul Hyde, K. Jamrogowicz, Dave Jones, Richard Kacerek, Richard Lancaster, Joseph Lemaire, Mark McIntyre, Hiroshi Ogawa, Paul Mohan, Stan Nelson, Lubos Neslusan, BillR, Whitham D. Reeve, John Schlin, Ann Schroyens and Denis Vida.

Financial support is still needed and welcome:
https://www.justgiving.com/crowdfunding/meteor-news?utm_term=JJBjmJpzV

Contributing to this issue:

- Aceituno J.
- Aimee A.I.
- Ávila D.
- Barbieri L.
- Brando G.
- de Guindos E.
- Eschman P.
- Fontana P.
- García A.
- Gómez-Hernández A.
- Gómez-Martínez J.
- Harachka Y.
- Harman E.
- Izquierdo J.
- Jenniskens P.
- Johannink C.
- Kacerek R.
- Koseki M.
- Madiedo J.M.
- Massey B.
- Olivera W.
- Ortiz J.L.
- Palacián J.
- Roggemans P.
- San Segundo A.
- Santos-Sanz P.
- Sarto S.
- Šegon D.
- Sergei I.
- Tosar B.
- Verbelen F.
- Vida D.
- Yanguas P.
- Zavadich R.

ISSN 2570-4745 Online publication <https://meteornews.net>

Listed and archived with ADS Abstract Service: <https://ui.adsabs.harvard.edu/search/q=eMetN>

MeteorNews Publisher:

Valašské Meziříčí Observatory, Vsetínská 78, 75701 Valašské Meziříčí, Czech Republic
